

THESIS FOR THE DEGREE OF DOCTOR OF PHILOSOPHY

Studies of Volcanic Plumes with
Remote Spectroscopic Sensing Techniques
DOAS and FTIR measurements on volcanoes of the
Network for Observation of Volcanic and Atmospheric Change

Santiago Rafael Arellano



CHALMERS

Department of Earth and Space Sciences
CHALMERS UNIVERSITY OF TECHNOLOGY
Gothenburg, Sweden 2014

Studies of Volcanic Plumes with Remote Spectroscopic Sensing Techniques
DOAS and FTIR measurements on volcanoes of the
Network of Observation of Volcanic and Atmospheric Change
SANTIAGO RAFAEL ARELLANO

© SANTIAGO RAFAEL ARELLANO, 2014

ISBN: 978-91-7597-070-7
Doktorsavhandlingar vid Chalmers tekniska högskola
Ny series nr 3751
ISSN 0346-718X

Department of Earth and Space Sciences
Optical Remote Sensing Group
Chalmers University of Technology
SE-412 96 Gothenburg, Sweden
Telephone +46 (0) 31-772 10 00

Cover:
Global map of SO₂ emissions from volcanoes in NOVAC, photograph of volcanoes in Java,
and example of a DOAS evaluation for SO₂

Printed by
Reproservice
Chalmers Tekniska Högskola
Gothenburg, Sweden 2014

STUDIES OF VOLCANIC PLUMES WITH
REMOTE SPECTROSCOPIC SENSING TECHNIQUES
DOAS and FTIR measurements on volcanoes of the
Network of Observation of Volcanic and Atmospheric Change

SANTIAGO RAFAEL ARELLANO
Department of Earth and Space Sciences
Chalmers University of Technology

Abstract

Volcanism is a rich geodynamical process, closely linked to the origin and ongoing evolution of the lithosphere, atmosphere, hydrosphere and biosphere. Humans have benefited from the resources provided by volcanoes but also been threatened by the dangers of volcanic eruptions, which accurate prediction remains elusive. This is partly due to the inherent complexity of volcanic systems and partly because of the difficulty of conducting key observations to characterize them. In particular, since the segregation and escape of magmatic volatiles are essential mechanisms behind volcanic eruptions, monitoring the intensity and composition of the resulting emissions in the atmosphere is essential to characterize the state of volcanic activity; however, their direct measurement is not always feasible.

Remote spectroscopic sensing, whereby gas species can be quantified by their spectral signatures in electromagnetic radiation gathered at a prudent distance from the plume, offers the possibility to conduct reliable and sustainable monitoring of volcanic emissions. To expand the remote sensing capabilities of volcanological observatories the Network for Observation of Volcanic and Atmospheric Change (NOVAC) was established in 2005.

The central theme of this thesis is the acquisition, analysis and interpretation of measurements of volcanic gas emissions on volcanoes of NOVAC. Measurements of the mass flow rate of SO_2 and the molar ratios of SO_2 against BrO and HCl were obtained by scanning-Differential Optical Absorption Spectroscopy (DOAS) of scattered solar ultraviolet radiation and by Fourier-Transform Spectroscopy (FTIR) of direct solar infrared radiation. The uncertainty of the measurements is characterized and methods for combining observations from different sensors implemented. Statistical and physical models of degassing are proposed for selected volcanoes of the network. The resulting time-series of emission on 16 volcanoes is one of the more detailed compilations of volcanic degassing in the last decade, particularly from passive emissions which are difficult to detect from satellite platforms. This work aims at advancing our knowledge of volcanic eruptions for a better mitigation of their risks.

Keywords: Volcanic gas emissions, Remote Sensing, DOAS, FTIR, NOVAC.

List of publications

This thesis is based on the work contained in the following papers, referred to by Roman numerals in the text:

(Included)

- I. "Network for Observation of Volcanic and Atmospheric Change (NOVAC)-A global network for volcanic gas monitoring: Network layout and instrument description"
J. Geophys. Res., 115, D05304, 2010
B. Galle, M. Johansson, C. Rivera, Y. Zhang, M. Kihlman, C. Kern, T. Lehmann, U. Platt, S. Arellano, S. Hidalgo
- II. "Analysis of uncertainty of the time-averaged estimation of volcanic gas emission rate from scanning-DOAS measurements of tropospheric plumes", *manuscript*
S. Arellano, B. Galle, M. Johansson, C. Kern, M. Van Roozendaal, U. Platt
- III. "Inventory of SO₂ gas emission rate measurements from the global Network for Observation of Volcanic and Atmospheric Change (NOVAC)", *manuscript*
S. Arellano, B. Galle, M. Johansson, P. Norman, the NOVAC collaboration
- IV. "BrO/SO₂ molar ratios from scanning DOAS measurements in the NOVAC network"
Solid Earth, 5, 409-424, 2014
P. Lübcke, N. Bobrowski, S. Arellano, B. Galle, G. Garzón, L. Vogel, U. Platt
- V. "Degassing patterns of Tungurahua volcano (Ecuador) during the 1999-2006 eruptive period, inferred from remote spectroscopic measurements of SO₂ emissions"
J. Volcanol. Geotherm. Res., 176, 151-162, 2008
S. Arellano, M. Hall, P. Samaniego, J.L. LePennec, A. Ruiz, I. Molina, H. Yepes
- VI. "Magnitude, intensity and impact of SO₂ gas emissions from Nyiragongo volcano during 2004-2012", *manuscript*
S. Arellano, M. Yalire, B. Galle, M. Johansson, P. Norman, N. Bobrowski

(Not included)

- VII. "Early in-flight detection of SO₂ via Differential Optical Absorption Spectroscopy: a feasible aviation safety measure to prevent potential encounters with volcanic plumes"
Atmos. Meas. Tech., 4, 1785-1804, 2011
L. Vogel, B. Galle, C. Kern, H. Delgado, V. Conde, P. Norman, S. Arellano, O. Landgren, P. Lübcke, J.M. Álvarez, L. Cárdenas, U. Platt
- VIII. "Detailed multidisciplinary monitoring reveals pre- and co-eruptive signals at Nyamulagira volcano (North Kivu, Democratic Republic of Congo)"
Bull. Volcanol., 76, 787, 2013
B. Smets, N. d'Oreye, F. Kervyn, F. Albino, S. Arellano, M. Bagalwa, C. Balagizi, S. Carn, T. Darrah, J. Fernández, B. Galle, P. González, E. Head, K. Karume, D. Kavotha, F. Lukaya, N. Mashagiro, G. Mavonga, P. Norman, E. Osondu, J. Pallero, J. Pioto, S. Samsonov, M. Syauswa, D. Tedesco, K. Tiampo, C. Wauthier, M. Yalire
- IX. "SO₂ degassing at Tungurahua volcano (Ecuador) between 2007 and 2013: transition from continuous to episodic activity"
Submitted to J. Volcanol. Geotherm. Res.
S. Hidalgo, J. Battaglia, S. Arellano, A. Steele, B. Bernard, J. Bourquin, B. Galle, S. Arrais, F. Váscónez
- X. "Gas emission strength and evolution of the molar ratio of BrO/SO₂ in the plume of Nyiragongo in comparison to Etna"
Accepted for publication in J. Geophys Res.
N. Bobrowski N., R. von-Glasow, G. Giuffrida, D. Tedesco, A. Aiuppa, M. Yalire, S. Arellano, M. Johansson, B. Galle
- XI. "Daily monitoring of Ecuadorian volcanic degassing from space"
J. Volcanol. Geotherm. Res., 176, 1, 141-150, 2008
S.A. Carn, A.J. Krueger, S. Arellano, N.A. Krotkov, K. Yang

To Vivi, Isaac and Carolina

&

To our mothers María Dolores and Marlene

And the memory of our fathers Rafael and Jorge

List of contents

Preface	xi
1. Introduction	1
1.1. Volcanic eruptions, environment and humans	2
1.1.1. Monitoring volcanic eruptions	4
1.1.2. Remote sensing of volcanic plumes	7
1.2. Atmospheric spectroscopy.....	11
1.2.1. Physical properties of the atmosphere.....	11
1.2.2. Observing atmospheric molecules at a distance	12
1.2.3. Spectroscopy – observing the interaction of matter and radiation.....	15
Matter.....	15
Radiation	18
Interaction.....	19
1.2.4. Instrumental considerations	23
2. Measurement techniques and data analysis	27
2.1. Inversion of remote spectroscopic sensing data	27
2.2. DOAS	28
2.2.1. DOAS measurements of volcanic gas emission rates	35
2.2.2. Scanning DOAS instrument	37
2.2.3. Uncertainty related to Scanning DOAS measurements	39
2.3. NOVAC	40
2.4. FTIR	41
2.4.1. FTIR measurements of volcanic gas molar ratios	43
2.4.2. Solar FTIR	44
2.4.3. Open-Path FTIR.....	45
3. Results	49
3.1. Observations with DOAS on several volcanoes.....	49
3.2. Observations with FTIR on several volcanoes.....	59
3.3. Observations from the network perspective: NOVAC	63
3.4. Geophysical models of volcanic degassing.....	64
3.4.1. Gas emissions as a proxy of magma discharge	64
3.4.2. The frequency distribution of passive volcanic degassing.....	66
4. Summary of publications	71
5. Conclusions and outlook	75
6. References	77
Appended articles	85

Preface

This document summarizes the most significant work carried out during my doctoral program at Chalmers during 2009-2014. It is a "compilation thesis", meaning that it contains a brief overview of the problems and areas studied (Chapter 1), the methods used (Chapter 2) and the results obtained (Chapter 3) during my research; followed by a selection, that intends to be as coherent as possible, of six referred articles and manuscripts product of my research work (Chapter 4 and Annexes).

I joined the Optical Remote Sensing Group after a few years of fruitful cooperation with Bo Galle within the NOVAC (Network for Observation of Volcanic and Atmospheric Change) project (2005-2010). This network joined the expertise in volcanology, atmospheric spectroscopy and meteorology of leading groups in Europe with the experience in volcanological observatories in several developing countries to establish a coordinated effort to quantify volcanic gas emissions in the atmosphere. As a consequence, in the last decade we have seen a notable increase in the amount of information regarding emissions from volcanoes, and a renewed interest on the development of remote sensing methods to study volcanic processes. The young community of "remote-plume" scientists is now about as big as the traditional community of "direct-plume" researchers, and many open questions remain to be answered in this exciting field with technological, scientific and humanitarian facets.

My work follows up the important contributions of present and past members of the NOVAC collaboration who settled the basic developments in instrumentation, installations and data processing for the network. My grain of sand (or *tephra*, for that matter), in the instrumentation side, has been to help with the assembly, calibration and maintenance of dozens of NOVAC instruments and a few basic developments for the solar-FIR technique. My most important contribution, presented in this thesis, has been the post-processing of the data-archive of the network and the use of volcanic emission time-series to study geophysical processes on particular volcanoes and from a global perspective.

Concerning the preparation of this document, I am indebted to my supervisor Bo Galle and co-supervisor Johan Mellqvist for very useful criticism on different sections of its content and the administration of the Department of Earth and Space Sciences, Chalmers Library and Chalmers Reproservice for their professional logistical support. The NOVAC, FIEL-VOLCAN, Congo, FUTUREVOLC, and DECADE projects, and scholarships from the Friends of Chalmers Foundation, Chalmersska forskningsfonden and the Department of Earth and Space Sciences (Chalmers), are greatly acknowledged for providing funding for this work.

As a final of these preliminary sentences, I hope the reader of this thesis will find it interesting or even useful, and that at least some of the excitement of devising strategies to study natural events of important societal consequences be conveyed by reading the following chapters.

Santiago Arellano
Gothenburg, 2014

1. Introduction

*"It's tempting to go to the throat of the volcano to get the data; because if you do you're a hero...
It's a battle between your mind and your emotions.
If your emotions win out, you can get yourself in a lot of trouble."*

— Ken Wohletz ¹

In the quest for understanding the inner workings of our planet, scientists face the challenge of performing observations at scales difficult to experiment in the laboratory. Furthermore, the challenge of studying geophysical systems lies on their complexity, due to the interplay of different components, processes and feedbacks in the system. Volcanoes exemplify this situation. They are shallow manifestations of deep geodynamical processes leading to the generation and transport of magma. Although these processes may occur during hundreds or thousands of years, the time span of a volcanic eruption may be minutes, hours, days, or years. The disruption caused by volcanic events range from local to global, depending on the magnitude (mass) and the intensity (emission rate) of the ejected material. Volcanoes have left a profound imprint in human culture. However, since large volcanic eruptions occur less often than small events, human societies tend to lose the historical memory of their occurrence. This complicates the management of volcanic crises, especially in densely populated zones.

As we understand more and more about the processes leading to eruptions, we recognize their complexity but also the limitation of our means to observe directly certain key characteristics of the volcanic system. Scientists should resort to ingenuity to obtain information about the state of the volcano, to infer the probable scenarios and update them as they accumulate more information. Uncertainties are large and should be properly assessed and openly communicated. Many situations of crises need to be faced on the basis of precautionary principles.

At the heart of a volcanic event lies the process of degassing, by means of which small amounts of certain volatile species present in the magma (notably H₂O, CO₂, SO₂, H₂S, HCl, HF, OCS, CO) are separated and transported out of solution and emitted into the atmosphere (for sub-aerial volcanoes). The resulting volcanic plume is the farthest reaching effect of an eruption, and it does not only carry on the message of certain properties of the volcano, but constitute in itself an agent of important interactions with the environment.

Important as they are, they are difficult to study. They can be corrosive, highly acidic or extremely hot, too high or wide to be sampled. Moreover, they should be observed continuously or frequently, to arrive at meaningful conclusions about the state and change of activity.

The development of remote sensing methods to measure volcanic gaseous emissions in the atmosphere has provided the means to tackle some of the abovementioned problems. Automatic systems can be deployed and operated permanently from a safe distance to

¹ Quoted by Ron Russell in 'Column One: In pursuit of Deadly Volcanoes', Los Angeles Times (25 Jun 1991), an article about three scientists who had died in a volcanic eruption

get, for instance, the mass flow rate of a volcanic component. Data can be analyzed on the way, and informed to authorities. The relative composition, the rate of emission, cycles, trends or general characteristics of the distribution of emissions can be studied and related to other geophysical observables to better delineate the situation and potential changes.

In this chapter we present an overview of the problem of measuring and interpreting the emission characteristics of volcanoes by remote spectroscopic sensing to try to understand the state and changes of volcanic activity.

1.1. Volcanic eruptions, environment and humans

Volcanoes dominate the geography of vast regions of our planet. Some of them look like high glacier-capped cones, others like low, flattened shields; they can be inactive for centuries and prone to external erosion, or in permanent eruptive activity and self-sustained growth. Volcanism not only includes the conspicuous protruding subaerial, subglacial or sublacustrine mountains that we identify as volcanoes but also the less evident but much more widespread submarine vents, which may represent about 80% of the magma mass production on Earth (Parfitt and Wilson, 2008). Terrestrial volcanism is the most important mechanism for crust generation and participates on several geochemical cycles like those of sulfur, carbon and halogens. It has also been hypothesized that volcanism has influenced the early formation of the atmosphere and hydrosphere through the outgassing of volatile species originated in the mantle (Allègre et al., 1987). Eruptions have also been observed in other planetary bodies of the Solar System like the Moon, Mars, Venus, and Jupiter's moon, Io, owing to apparently quite different causative mechanisms (Wilson, 2009).

The material ejected by subaerial volcanic eruptions may alter significantly the state of the surrounding environment at various degrees of impact as well as of temporal and spatial extent. Most of the erupted mass corresponds to consolidated material; i.e., consisting of tephra, pyroclasts or lava, which impact, although potentially devastating, is usually confined to relatively short distances from their source. Conversely, emissions of gas and small particles have the potential to reach higher layers of the atmosphere and be transported over large distances. For instance, the explosive eruption of El Chichón in 1982 produced a cloud that circumvented the world in 3 weeks (Robock and Matson, 1983). Among the gaseous species emitted by volcanoes is sulfur dioxide (SO_2), which can be oxidized to sulfuric acid (H_2SO_4) aerosols. The lifetime scale of sulfate aerosols in the stratosphere is in the order of months to years (Robock, 2000), depending on the latitude of the volcano and the global circulation patterns of the atmosphere. Although major eruptions are capable of injecting their emissions into the stratosphere, under certain conditions this is also possible for smaller eruptions, as it has been suggested for the event of Nabro in 2011, which originally upper tropospheric plume was raised by convection presumably associated with the Asian Monsoon (Bourassa et al., 2012). In fact, recent studies suggest that small to moderate but persistent eruptive activity during the 2000-2010 decade, in addition to usual troposphere-stratosphere exchange mechanisms, are sufficient to explain the observed deceleration of tropospheric warming expected from the greenhouse effect, due to an enhance loading of sulphate aerosol in the stratosphere (Neely et al., 2013).

The main effect of a sulfate veil in the stratosphere is producing a radiative perturbation due to absorption and scattering of solar radiation. This may result in a net cooling of the

troposphere and local warming of the stratosphere. The presence of certain species (like halogens) in volcanic emissions and particles that provide a surface for chemical reactions may also cause ozone (O₃) depletion. Aerosols can also affect the microphysics of clouds and act as seeds for heterogeneous nucleation, which in turn affects the radiative balance. Other important species that compose volcanic plumes like water (H₂O) and carbon dioxide (CO₂) absorb infrared radiation and thus influence climate change via the greenhouse effect. Their contribution is however minor in relation to anthropogenic sources; in fact, it has been estimated that the equivalent to about 700 Pinatubo -1991- or 3500 Mount St. Helens - 1990- paroxysms per year would produce CO₂ emissions comparable to those annually generated by human activities at present (estimated to be on the order of 35 Pg a⁻¹ vs. 0.13-0.44 Pg a⁻¹ emitted by volcanoes (Gerlach, 2011)). Sulfate aerosols near ground are responsible for pollution, usually referred to as “vog”, for volcanic smog (and smog coming from “smoke fog”). Strong volcanogenic acids like hydrogen chloride (HCl) or hydrogen fluoride (HF) are highly corrosive and soluble in condensed water potentially resulting in acid rain. Besides these important effects on the atmosphere, volcanic eruptions seem to affect the climate system via acceleration of glacier melting (Major and Newhall, 1989) and cooling of the oceans –reduction of ocean-atmosphere temperature gradients- (Gleckler et al., 2006). These effects are thought to be in turn responsible for changes in precipitation patterns and regional to global winter warming and summer cooling (Robock and Oppenheimer, 2003). Moreover, feedback mechanisms of the icecaps and ocean systems after major volcanic eruptions have been suggested as feasible causes of the onset and maintenance of the “Little Ice Age” towards the middle of last millennia (Miller et al., 2011). Reconstruction of past volcanogenic climate forcing is attempted by the compositional analysis of ice-cores (Gao et al., 2008) and tree rings (Robock, 2005). All in all, it is believed that volcanic eruptions constitute a strong, yet brief perturbation of the climate system, especially if they are explosive, rich in SO₂ emissions and originated at lower latitudes (Grainger and Highwood, 2003).

Certain volcanic areas possess not only aesthetic sceneries but also fertile lands for cultivation and rich mineral formations, favoring the development of human settlements. As a consequence, many cultures have flourished around volcanic areas and integrated volcanoes into their religious or artistic world views, but have, on the other hand, experienced the devastating effects of their cataclysms. Major volcanic events may have even led to important cultural transformations in the most favorable cases, but undoubtedly also to extermination of entire communities in the most adverse ones. As an example, the extent famine produced by the eruption of Laki in 1783-1785 resulted in widespread mortality in Europe, that according to some authors (Grattan et al., 2003), may have even played a role in promoting the onset of the French Revolution. The eruption of Thera (Santorini) in 1650 B.C., one of the largest on Earth, may have aided to the decline of the Minoan civilization. The destruction of roman cities by the eruption of Vesuvius in A.D. 79 or the most recent disaster of the Colombian village of Armero caused by the eruption of Nevado del Ruiz in 1985, are examples of the deadly volcanic impact on human populations (Oppenheimer, 2011).

The recent eruption of Eyjafjallajökull in 2010 (Sigmundsson et al., 2012), though relatively small in magnitude and intensity, focused the public attention once again towards volcanoes, due mainly to the closure of air traffic in Europe for several weeks and its associated economical impact. This is just another case showing that although our knowledge of volcanic phenomena is growing, the vulnerability of our technological society to volcanic hazards is also increasing, and so must be our preparedness based on adequate monitoring of the possible precursory signals, initiation and evolution of eruptions. The work reported here has the intention to contribute to the advancement of monitoring methods of gaseous emissions from eruptive volcanoes.

1.1.1. Monitoring volcanic eruptions

Terrestrial volcanic eruptions are shallow manifestations of deep mechanisms for heat and mass transport that are believed to occur since the formation of Earth. The primordial accreted mass of iron metals, oxides, silicates, and volatiles has undergone differentiation to form the present layered planetary structure from the core, through the mantle to the crust, oceans and atmosphere (Jackson et al., 2010). The unifying scheme of Plate Tectonics provides us with a picture of the present causation of volcanism: internal convection in the planet driven by complex thermal and gravitational gradients creates structures where magma, the fluid mixture of molten silicates, crystals and volatiles, is favorably generated and transported. These structures correspond to zones where tectonic plates converge (e.g., volcanic arcs) or diverge (e.g., mid-oceanic ridge) and to zones where a deeper flow of magma is able to ascend in more or less stationary regions over periods of time larger than the ascent period (e.g., intra-plate continental and oceanic "hot-spot" volcanism). Associated with divergent margins, low viscosity basaltic magma is generated by decompression melting and it is characterized by a low volatile abundance and low silica (SiO_2) content (~50-60 wt%), being an example the Icelandic volcanoes. At convergent margins, on the other hand, magma is composed by mantle basalt, melted continental crust and material from the subducted slab; the resulting high viscosity andesitic to dacitic magma has an intermediate SiO_2 content (~60-70 wt%) and it is rich in volatiles, as it is the case of e.g. the Andean volcanoes. Finally, at intra-plate continental volcanoes, basaltic magma plumes melt a layer of thick crust to produce very viscous rhyolitic magma, which has a high SiO_2 content (~70 wt%), for instance at Yellowstone; whereas at intra-plate oceanic hot-spots, basaltic plumes melt a thin crust layer generating low viscosity basaltic magmas, like in the case of the Galápagos volcanoes.

It is estimated that more than 1500 subaerial volcanoes have erupted during the Holocene, and therefore can be considered active in geological time-scales. About 540 of these have had eruptions in historical times, more than 380 in the last century, about 150 in the last 35 years of intensive monitoring, and in this period an average of 50 volcanoes have presented either continuous or episodic eruptive activity every year, with an average of 20 volcanoes erupting simultaneously each day. More than 2/3 of these volcanoes are located in remote areas in the Northern hemisphere and the tropics, and many of them threaten largely populated regions, particularly in developing countries (Andres and Kasgnoc, 1998; Simkin, 1993; Simkin and Siebert, 1999; Wright and Pilger, 2008).

The set of particular conditions present at any given volcanic system determines the type of volcano and its eruptive activity. Such conditions are determined primarily by the tectonic setting which dictates the rate of production and composition of magma (silica content, amount and type of crystals, amount and type of volatiles), and the local/regional stresses, but also by the historical activity (lithological structure of the volcanic edifice and its surroundings) and the presence of liquid water (oceans, lakes, hydrothermal systems, glaciers). Under certain conditions, external forcing caused by local meteorological conditions and Earth tides can play a role in triggering or modulating eruptive activity (Connor et al., 1988; Matthews et al., 2002).

A simplified model of the upper part of a volcanic system can be represented as composed of two distinct components: a deep magma reservoir and a narrow region for transport or conduit ending in the vent. Magma fed from depth is stored at the reservoir for dormant

periods that are usually 30-60 times longer than eruption periods at different tectonic settings (Simkin and Siebert, 1984). In order to initiate an eruption, an overpressure in the reservoir must be created. One possible mechanism for this would be as follows: if not constantly fed by "fresh" magma injected from deeper levels, stagnant magma in the reservoir loses heat by conduction to the confining wall rocks, causing a series of petrological differentiation, i.e. chemical alteration, mechanisms, by which magma acidifies. Moreover, the initiation of (heterogeneous) nucleation of the less soluble volatile species, usually CO₂, may lead to the accumulation of a gaseous phase in the reservoir, with the concomitant increase in pressure and enhanced acidification and crystallization. If the overpressure is high enough to overcome the gravitational lithospheric pressure, a pathway for magma migration in the form of a crack or dike is formed, and magma starts to ascend by buoyancy and excess pressure. The continued movement produces a conduit that eventually connects the reservoir with surface forming an eruption. Other mechanisms for eruption initiation include the chemical mixing or physical mingling of a basic and an acid magma, tectonic stresses by local or distant triggers, or direct feeding from the mantle, especially in divergent margins (Parfitt and Wilson, 2008).

The conduit is the region of magma transport where the most dynamic processes occur, since the rapid migration of magma implies a pressure reduction that promotes further nucleation, growth, deformation, and coalescence of bubbles of gaseous species. It is also a zone for the formation of networks for gas escape, loss of heat and gases to the conduit walls, and crystallization. These processes produce dramatic changes in the rheological properties of the fluid, especially its viscosity, and as a consequence, the dynamics of shallow magma ascent may be highly non-linear and result in different regimes or styles of eruption: effusive, explosive or extrusive, and even change over the course of an eruption (Slezin, 2003; Sparks, 2003).

Our present understanding of the dynamics of volcanic eruptions thus tells us that although these events can indeed be very different in their style, duration, magnitude, intensity, and type of products (lavas, pyroclasts, ash, plumes, etc.), their essential causative mechanisms are similar. It is the variety of possibilities in terms of magma properties, system geometry and environment, and the non-linearity of their dynamics which creates the different aspects of volcanism and makes predicting a particular volcanic eruption, or a part thereof, so intricate.

During ascent, the changes of thermal, chemical, textural, and mechanical properties of the magma obey mostly to the loss of volatiles or degassing. The permeability of magma to gas transport and escape, and its ascent velocity in relation to the velocity of gas escape controls the transition between different eruptive styles (Dingwell, 1996; Gonnermann and Manga, 2006; Jaupart and Allègre, 1991; Massol and Koyaguchi, 2005; Melnik et al., 2005; Sparks, 2003; Wilson et al., 1980). Magma degassing is therefore a key parameter to monitor in order to characterize the dynamical state of a volcano. Figure 1 illustrates some general features of the structure, components and processes of the volcanic system.

Having in mind the processes involved in magma migration, it is obvious that a number of geophysical and geochemical effects should be observable at surface. Volcanological monitoring relies on measuring these effects, which may include acoustic oscillations at ground (seismicity) or in the atmosphere (sound, infrasound), geodetic deformation, changes in the composition and emission rate of gases, thermal anomalies, petrological changes, gravimetric perturbations, electromagnetic disturbances, among others (Scarpa

and Tilling, 1996; Sparks et al., 2012). The establishment of dedicated modern volcano observatories started at Vesuvio in 1845; today, the World Organization of Volcano Observatories (WOVO), has about 80 members. A few of these observatories count with sophisticated geophysical monitoring networks for the most dangerous or active volcanoes. However, most of them lack enough human expertise and/or instrumental capabilities to perform adequate volcano surveillance.

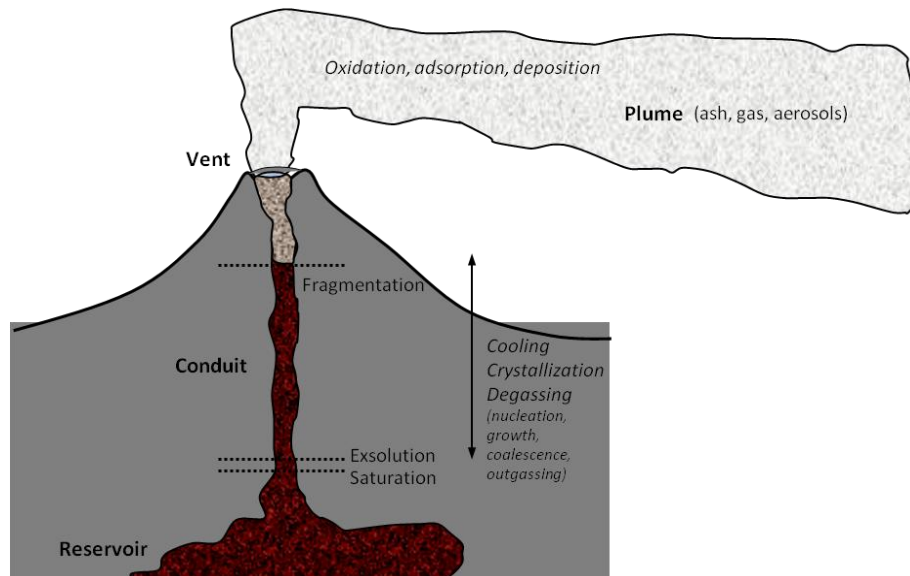


Figure 1. The volcanic system (not to scale). Magma accumulates in a shallow reservoir and ascends through a conduit to the main vent. At a certain depth, magma saturates in some volatiles and at a shallower level, the overpressure leads to bubble formation, eased by the presence of crystals. Different processes can bring the mixture of melt, crystals and bubbles to disrupt, forming an ash plume, or to passive degassing without magma discharge. Inside the plume, different processes occur downwind the source.

The primary characterization of a volcanic system is done by basic geological mapping to define the petrology and morphology as well as the history of the volcano. Once a volcano is considered active, monitoring is recommended. Seismic monitoring is the most widespread method to monitor volcanoes. Magma ascent produce fractures of the rocks, resonances of magma and gases in cracks, or pressure oscillations that are transmitted as acoustic signals through the lithosphere and deeper terrestrial layers. Local networks of seismometers are deployed around volcanoes and typically measure velocity or acceleration of the ground and transmit their signals telemetrically to a base station. The signals are classified according to their spectral signatures, duration, intensity, magnitude, location, and have played an important role in defining the baseline activity, the signals of unrest and the dynamical state of the volcanoes during eruptions. The second most used monitoring method is geodetics, which include a series of static or dynamic displacement meters, arrays of GPS receivers, interferometric synthetic aperture radar (InSAR), tiltmeters, and other instruments. Shallow magma ascent is usually accompanied by inflation signals, whereas depleted magma chambers can produce ground depressions. These observations usually give information on the reservoir geometry and allow detecting precursory signals with anticipation. The third most common technique involves direct sampling and remote sensing of volcanic gases in

air or water bodies. The composition, emission rate, electrical properties, isotopic signatures, and other characteristics provide information on the physical-chemical state of the volcano. Thermal sensors in ground or remote platforms measure the thermal radiation or temperature of hot magmatic rocks and gases. Infrasound or microphones detect acoustic signals accompanying emissions of volcanic material. These signals are sometimes able to travel large distances through atmospheric pathways. Petrological analysis allows determining the conditions of the magma at diverse stages during the eruption, based for example on the chemical characterization of the melt and crystals, the measurement of volatiles trapped in crystals (melt inclusions), or the crystallography of the sample rocks. Related to these methods is the quantification of the amount and size distribution of the material emitted by an eruption either via field mapping in ground or by remote sensors. Cameras and radar sensors measure the ejection velocity of erupted blocks. Other instruments measure the self-electrical potential, magnetic field, gravimetric anomalies, radioactivity of magma bodies, or even the internal structure of volcanic edifices via muon-tomography. An essential understanding of an eruption is achieved by direct visual observation of the activity, an essential task of an observatory. The combination of simultaneous observations retrieved from different techniques is a powerful procedure to gain understanding of the structure and dynamics of an active volcano (Scarpa and Tilling, 1996; Sturkell et al., 2008; Shinohara and Tanaka, 2012; Sparks et al., 2012).

1.1.2. Remote sensing of volcanic plumes

Paradoxically, volcanic volatiles are present in small amounts in the magma but can exert a major role in triggering or controlling eruptions. Also paradoxically, in spite of their importance in the eruptive process and effect on environment, permanent monitoring of volcanic gases has been rather uncommon. The reason to the first puzzle has to be found principally in the special characteristics of volatiles to control the rheology of magmas, as explained in the preceding section. The clue to the second question lies on the obvious logistical difficulties to access the vents for direct sampling of volcanic gases. In-situ collection of gaseous samples in hot-temperature fumaroles or hydrothermal fields has in fact a long history. Direct sampling methods include evacuated bottles with alkali solutions to prevent uncontrolled post-collection chemical reactions (Taran, 2009), but also electrochemical sensors (Shinohara, 2005), tunable diode-laser systems (Gianfrani and De Natale, 2000), mass spectrometers (Diaz et al., 2002), or in-plume optical particle counters (Weber et al., 2010). After sampling with a traditional evacuated bottle, post-analysis by conventional laboratory methods permits a thorough characterization of the composition of gaseous species, temperature, pH, electrical conductivity, and other physical-chemical properties. This type of studies indicates that, depending on the tectonic setting, hydrothermal environment and other conditions, the most abundant volcanogenic volatile species and their concentrations (%vol) are: H₂O (50-90), CO₂ (1-40), SO₂ (1-25), H₂S (1-10), HCl (1-10), HF (<10⁻³), COS (10⁻⁴-10⁻²), CS₂ (10⁻⁴-10⁻²), HBr (10⁻⁶), HI (<10⁻⁶). These estimates are subject to a large level of uncertainty due principally to the reduced number of studied cases and the natural variability of the emissions. (Textor et al., 2003).

Sulfur and halogen compounds emitted by volcanoes have the largest environmental impact due to their relatively low background concentrations in the atmosphere. The lifetime of these species in the atmosphere depends on different aspects like the oxidation capacity

of the local atmosphere, the humidity, altitude, solar irradiance, ash and aerosol content, or wind patterns. It is therefore only possible to estimate an order of magnitude lifetime, which for species such as SO₂ and H₂S lies in the order of hours-days in the troposphere, and weeks in the stratosphere, where are usually converted to H₂SO₄, a species with a lifetime of months-years. HCl, HF, HBr are much more soluble in water and thus are easily removed by water droplets and precipitation or undergo chemical reactions producing secondary radicals (e.g., ClO, BrO) which have a huge impact on the catalytic destruction of O₃ (Bobrowski et al., 2003; von Glasow et al., 2009).

The estimates of global emission of SO₂ from volcanoes vary among authors between 1-50 Tg a⁻¹, depending on the way of counting and the data used for the extrapolation (e.g., Halmer et al., 2002). It is usually assumed that the distribution of emitters follows a power-law (the number of volcanoes emitting more than a certain average flux per year is proportional to the flux itself elevated to the negative power of an exponent). This assumption allows estimating the global emission from a sample of the most representative emitters if the exponent is lower than unity, which certain studies show to be a likely condition (Andres and Kasgnoc, 1998).

To measure the emission rate of SO₂ from a volcano the most common method is passive remote sensing. This can be accomplished from a stationary or moving platform, from vehicles in land, water, air, or space. The first and most known method used by volcanologists for almost three decades is the Correlation Spectrometer (COSPEC), which has been used since the beginning of the 1970s on a number of volcanoes (Moffat and Millan, 1971; Stoiber and Jepsen, 1973; Williams-Jones et al., 2008). COSPEC is an ultraviolet (UV) dispersive spectrometer that uses differential absorption of a number of pairs of absorbing and non-absorbing bands that are isolated by slits engraved in a rotating disc. The instrument is mostly used in passive mode, measuring the scattered solar radiation in the atmosphere (skylight) collected by a Cassegrain telescope, transmitted through the spectrometer, disc, and ending in a sensitive photomultiplier tube detector. To calibrate the measurement, a couple of cells with known concentrations of SO₂ are employed, which measurement is done while pointing the spectrometer to a region without the gas of interest. At least five generations of the COSPEC were developed by the Barringer Research Limited in Canada, and all of them were equipped with a paper plotter to record the measurements, limiting the possibilities of post-analysis by digital means. The COSPEC can be powered by a 12V car battery and the whole system, including the telescope and a supporting/pointing tripod, can be transported in a vehicle and mounted by a single operator. The method to quantify the flux of a gas by passive remote sensing is explained in Chapter 3. Perhaps the most important spectroscopic limitation of the COSPEC lies in its specificity, given the reduced information content of the narrow bands it uses and the strong interference of O₃ and molecular or aerosol scattering in the region of absorption of SO₂. On the other hand, being the only instrument used by (a few of) volcanologists worldwide meant that the procedures were to a large extent standardized and thus the measurements directly comparable. The first estimates of global contribution of SO₂ from volcanoes to the atmosphere were done based on records of measurements with the COSPEC in a limited number of volcanoes (Stoiber and Jepsen, 1973; Stoiber et al., 1987; Andres and Kasgnoc, 1998; Halmer et al., 2002, Paper III). A summary of different methods for remote sensing of volcanic gases in the ultraviolet (UV), visible (Vis) infrared (IR) spectral regions is presented in Table 1.

Table 1. Operational portable and satellite-based instruments for remote sensing of volcanic gas emissions

Name	Principle	Measured volcanic species	Approximate cost (Euro)	Reference
COSPEC (Correlation spectrometer)	Mask filter correlation spectroscopy	SO ₂	50k	(Hamilton et al., 1978)
DOAS (Differential Optical Absorption Spectroscopy)	Broad-band, dispersive, differential absorption spectroscopy	SO ₂ , BrO, ClO, NO ₂	5-10k	(Galle et al., 2003)
DIAL (Differential Absorption LIDAR)	Differential absorption spectroscopy with light detection and ranging	SO ₂	100k	(Weibring et al., 2002)
GASCOFIL (Gas filter correlation spectrometer)	Gas filter correlation radiometry	CO, COS	50k	(Stix et al., 1996)
FTIR (Fourier Transform Infra-Red spectroscopy)	Broadband infrared interferometry	H ₂ O, CO ₂ , SO ₂ , HCl, HF, CO	50k	(Notsu et al., 1993)
IDOAS (Imaging DOAS)	2D array of DOAS channels	Same as DOAS	20k	(Bobrowski et al., 2006)
UV SO ₂ Camera	2D detector, non-dispersive filter radiometry (sometimes calibrated by a parallel DOAS)	SO ₂	20k	(Bluth et al., 2007)
IR SO ₂ Camera	2D detector, non-dispersive filter correlation radiometer	SO ₂ , ash	30k	(Prata and Bernardo, 2009)

Table 1 (continued)

Satellite-based sensor	Footprint area (km²)	Sensitivity at < 5 km altitude* (Mg SO₂) (1 σ)	Smallest detectable cloud (Mg SO₂) (5 pixels at 5σ)	Reference
TOMS (Total Ozone Mapping Spectrometer)	39×39	70	7800	(Krueger et al., 1995)
SCIAMACHY (Scanning Imaging Absorption Spectrometer for Atmospheric Cartography)	30×60	4	250	(Afe et al., 2004)
GOME-2 (Global Ozone Monitoring Experiment)	40×80	4	914	(Eisinger and Burrows, 1998)
OMI (Ozone Monitoring Instrument)	13×24	4	87	(Carn et al., 2007)
OMPS (Ozone Mapping and Profiler Suite)	50×50	4	700	Carn (pers. comm.)
IASI (Infrared atmospheric sounding interferometer)	d=12	180	1420	(Clarisse et al., 2008)
MODIS (Moderate Resolution Imaging Spectroradiometer)	1×1	2500	175	(Watson et al., 2004)
ASTER (Advanced Spaceborne Thermal Emission & Reflection Radiometer)	0.09×0.09	2500	1.4	(Urai, 2004)
AIRS (Atmospheric Infrared Radiation Sounder)	d=13.5	300	2990	(Prata and Bernardo, 2007)
SEVIRI (Spinning Enhanced Visible and Infrared Imager)	4.8×4.8	2500	4010	(Prata and Kerkmann, 2007)

*Sensitivity at 20 km (stratosphere) is estimated to be a factor of 2 better than in the troposphere

1.2. Atmospheric spectroscopy

This section reviews some basic concepts of spectroscopic methods for the remote measurement of molecules in the atmosphere.

1.2.1. Physical properties of the atmosphere

Earth's atmosphere is a mixture of compounds in different states of aggregation. The lower layers (homosphere) have a relatively stable composition of molecules, whereas the higher layers (heterosphere) contain a large proportion of ions with changing concentration depending on the flux of energetic particles and electromagnetic radiation from the sun and surrounding space. The atmosphere is also interacting with the other subsystems on Earth, such as the hydrosphere, cryosphere, lithosphere, biosphere. The flux of mass and energy between these systems and the flux of extraterrestrial energy produce changes in the vertical and horizontal structure of the atmosphere, but also create relatively stable spatial and temporal patterns (the climate). Due to the composition of the atmosphere, there is a well defined thermal layering composed of the troposphere, stratosphere, mesosphere and thermosphere. Gravity is responsible for the exponentially decreasing density profile of the atmosphere. The atmosphere contains not only gases and ions, but also liquid droplets and solid particles (Seinfeld and Pandis, 2006). The work reported in this thesis focuses on measurements of gas concentrations in the troposphere. The temperature, density and composition profiles of the atmosphere are represented in Figure 2.

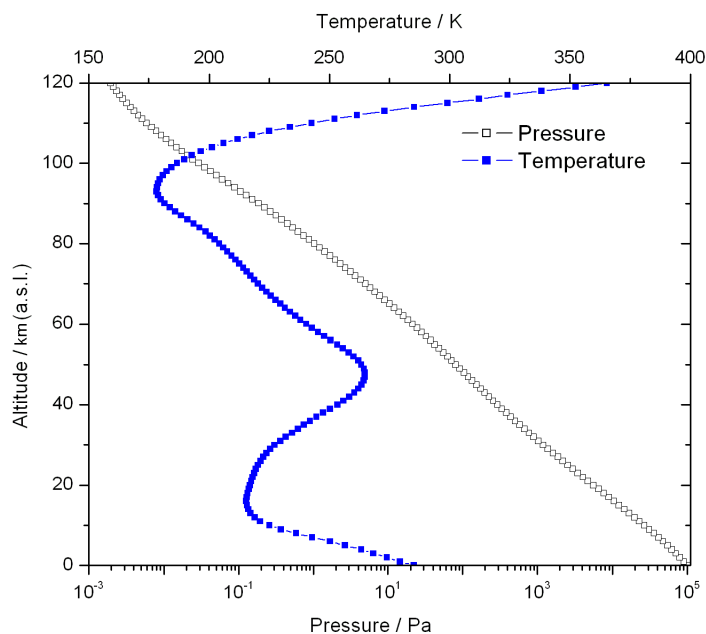


Figure 2a. Temperature and density profiles of a model Earth's atmosphere at mid latitudes. The measurements of volcanic plumes presented in this thesis are limited to the first kilometers of altitude, in the troposphere (<20 km).

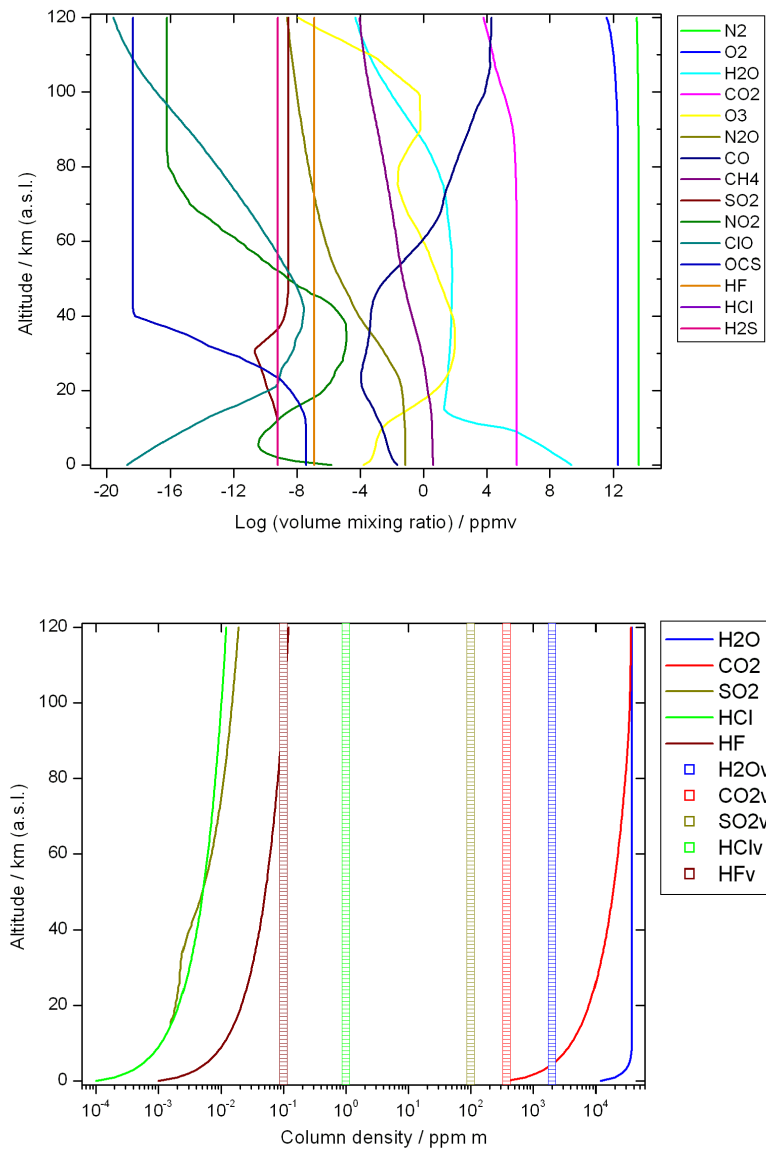


Figure 2b. Above: Background concentration profiles of main atmospheric constituents. Below: vertical column densities of background atmospheric and volcanic species. Notice that the volcanic SO₂ and HCl column densities are much higher than the background, facilitating their measurement (data from Oxford's Reference Forward Model atmospheric profiles for a mid-latitude standard atmosphere: <http://www.atm.ox.ac.uk/RFM/atm/>)

1.2.2. Observing atmospheric molecules at a distance

Our scientific understanding of Nature relies upon observation, broadly defined as a process by which a system (the observer) acquires certain information (the observable) about another system (the observed). The acquisition of information entails the interaction between the observing and observed counterparts, usually mediated by an instrument, which can be seen as an extension of the sensing capabilities of the observer. The observable in turn is a particular and well defined property of the system under scrutiny. Although our present description of Nature at the fundamental level of its elementary

constituents (Quantum Mechanics) defies the reality of a sharp distinction between these two interacting parts of the observational process, this conceptual scheme is helpful to represent the informational transaction involved in observation and it is a particularly accurate one at the typical mesoscopic scales of experimentation in geophysical research.

The field of Remote Sensing has been defined in many ways, all of which agree on the notion of observation at a distance (Elachi and Van Zyl, 2006). It has to be kept in mind; however, that observation implies a local interaction that takes place at the instrument-observer². In many cases the only difference between examples of so called "remote" and "direct" sensing is the scale at which the observation is performed. For instance, the visual observation of a bacterium under the microscope, an archetypal case of direct sensing, is not qualitatively different than an active open-path infrared observation of a volcanic plume, in the sense that what is being observed is actually enclosed by the sensing apparatus. A more scientifically rigorous definition of remote detection requires setting the lengths scales of the observer and observed parts and the requirement that a signal be transmitted between both through a distance that is larger than the scales of the systems. In electromagnetic remote sensing the signal is composed by electromagnetic waves/photons carrying information about the observed system and detected by the instrument.

Often observations are quantifiable, i.e., the observed property is comparable with a similar property adopted as a standard and reproducible unit of reference. In this case, the observation is called measurement and is generally performed by the instrument. In order for the measurement to be accurate, the instrument requires calibration to set the proper values to the measurement of controlled effects. Measurements always carry the effect of the instrument used to perform them, which limits the precision and accuracy of the measurement and therefore the instrumental effects should be ideally well characterized. Importantly, measurements constitute samples from the observed system, unavoidably limited in space and time, and therefore the observer should always ponder how representative results his or her measurement. In Paper II, an analysis of uncertainty for measurement of volcanic gases is presented.

Electromagnetic remote sensing of molecules in gas phase in the Earth's atmosphere can be conducted at different energies, from the microwave to the near-ultraviolet spectral regions, i.e., at wavelengths³ of about 10^{-2} to 10^{-8} m. This is a consequence of the properties of the molecules themselves (the existence of quantum states separated by these energies), the measurement environment (extinction of radiation due to radiative and collision processes) and the available technology (optical elements and detectors). This thesis explores some techniques in the mid-infrared (~2-15 μm) and near-ultraviolet (~300-360 nm) spectral regions.

Spectroscopy has a long and venerable history as a scientific tool for studying the nature and interactions of electromagnetic radiation with matter. The term spectrum itself seems to have been first used scientifically by Isaac Newton, who in 1665 produced the chromatic decomposition of solar light by a prism, a controlled observation of the essential process by which rainbows and other striking phenomena like halos, glories, coronas, iridescence, or

² It can be argued that the particular case of quantum-entanglement, where two systems share the same physical information even though they can be spatially separated, can be seen as an exception to this principle, but even in this case the observer needs to locally interact with one of the systems to get information about the other.

³ Energy and wavelength of photons are related by Planck equation: $E = hc/\lambda$, where E represents energy, h Planck's constant ($\sim 6.626 \times 10^{-34}$ m² kg s⁻¹), c speed of light in vacuum ($\sim 2.998 \times 10^8$ m s⁻¹), and λ wavelength.

supernumerary bows are formed in Nature, namely: the scattering of electromagnetic radiation by matter (Bohren and Clothiaux, 2006). In this thesis spectrum is meant a graphical representation of the distribution of a physical quantity as a function of another relevant variable (e.g., radiation intensity as a function of energy, number of particles as a function of mass-to-charge ratio, number of events in a given energy interval, etc.). The techniques employed for the observation of spectra are called spectroscopic, but in rigour, a classification between spectroscopes, spectrographs and spectrometers is in order to designate to the instruments used for observation, registration or measurement of spectra, respectively. Spectrophotometers, in specific, are instruments for the analysis of electromagnetic radiation. The work presented here was based on measurements with dispersive and interferometric spectrophotometers. The configuration of instruments for spectrometric remote sensing of gases depends on the specific objectives and conditions of measurement; however, a general scheme of the components of a typical instrument includes: a source (natural or artificial), a section for gathering and transfer (optics, antennae, etc.), a section for analysis (grating, interferometer, prism, gas-cells, crystals, etc.), and a section for detection-measurement (detector, amplifiers, A/D converter, computer, etc.) of incoming radiation. Each part of the system introduces an effect on the measurement that should be characterized and altogether define the instrumental function that modifies the incoming signal. A graphical representation of a general instrumental setup is shown in Figure 3.

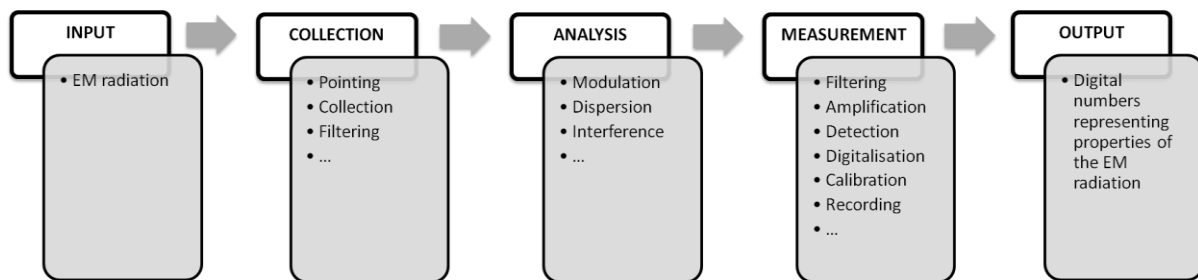


Figure 3. Schematics of the information flow for spectrometric remote measurements of gases in the atmosphere

The input signal is a determinant of the absolute limitation in the amount of information that can be retrieved from the measurement; therefore, an important part of the success of a remote sensing application is due to a proper instrumental design and an efficient measurement strategy to maximize the quality of the input signal. For instance, for remote sensing of volcanic gases in the ultraviolet spectral region by absorption spectroscopy, the choice of instrumental components should consider such aspects as the typical range of measurement, the spectral region of absorption of the volcanic species, the desired sampling rate, etc. A wide field of view can make the measurements faster but less accurate, accepting excessive amount of radiation from spectral regions outside those of interest can introduce detrimental effects including stray light on the signal, etc. The design of a remote sensing instrument should provide an answer to the question of how to achieve a defined signal to noise ratio for the measurement of a certain species under expected measurement conditions (distance, concentration, temperature, pressure, etc.)? On the basis of the scheme presented in Figure 3, it is possible to define different criteria for a classification of remote sensing techniques, as indicated in Table 2.

Table 2. Different classification criteria for electromagnetic remote sensing techniques

Criterion	Class	Name/Type
Nature of radiation source	Natural Artificial	Passive Active
Spectral analysis method	Dispersive Non-dispersive	Prism Grating Filter/mask/gas correlation Interferometry
Spectral bandwidth	Narrow-band Broad-band	Monochromator/spectrometer Radiometer
Output	Total radiant power Interferogram Spectrum Image	Radiometer Interferometer Spectrometer Imager
Measurement mode	Absorption Emission	

This thesis treats the case of passive remote sensing with grating and interferometric spectroscopic instruments deployed for measurements in absorption mode. A more detailed explanation of the principles behind these techniques is presented in the next chapter.

1.2.3. Spectroscopy – observing the interaction of matter and radiation

The analysis of spectra of atoms and molecules in interaction with electromagnetic radiation has played a crucial role in the development of our present understanding of the quantum properties of radiation and matter. In this section, we present the basic physics behind the formation of a spectral line, without going into details of this process that are not relevant for the rest of the material exposed in this work.

Matter

In essence, a measured spectral line is the instrumental signature left by the transition between possible energy states of a system (collection of atoms, molecules) due to the interaction of the “internal” components of the system and the “external” radiation field (or vacuum)⁴. Even a single molecule is conceived as a complex system with different types of motion, each of which requires a certain amount of energy, for example the molecule as a whole may have translational (thermal) motion respect to a fixed system of reference, the molecule can rotate respect to certain axes according to its geometry, their constituent atoms can vibrate respect to the centre of mass of the molecule, the electrons can make transitions between their orbitals, escape or being captured by the molecule, a disintegration of the nuclei can occur, etc. The interplay of internal and environmental forces

⁴ A rigorous treatment requires quantum electrodynamics, where the radiation field is quantized, but considering the usually high density of photons at even weak fields (of interest in this work), a semi-classical picture is sufficient. In this picture the radiation field is treated as continuous and the atomic system does not influence the radiation field that can be considered as external to it (Bransden and Joachain, 2003). In this sense, the vacuum (virtual particles) is also considered as an external field.

affecting the physical state of a molecule can alter the configuration of the system in a complicated manner. However, certain simplifying assumptions can be adopted to analyze the different changes of state of molecules as independent, especially for the relatively simple (di/tri-atomic) molecules or our interest and the relatively low energetic conditions in lower altitude levels of the Earth's atmosphere.

The translational motion of a collection of molecules in a non-confined environment like the atmosphere, and without considering external fields (which, like gravity, may be considered of negligible intensity), has a continuous spectrum of possible energy states. In the ideal gas and non-relativistic approximation, the probability distribution of speeds of molecules in thermal equilibrium at a temperature T is Gaussian, meaning that the probability $P(v_x + dv_x)$ of finding a molecule of mass M with a speed between v and $v + dv$ is proportional to the Boltzmann factor:

$$P(v + dv) \propto e^{-\frac{Mv^2}{2k_B T}} \quad (1)$$

The distribution has a mean value $\mu_v = 0$ and a standard deviation $\sigma_v = \sqrt{3k_B T/M}$, where k_B is Boltzmann constant ($\sim 1.381 \times 10^{-23} \text{ m}^2 \text{ kg s}^{-2} \text{ K}^{-1}$).

The kinetic energy of the translational motion $E_t = Mv^2/2$ is Chi-squared distributed, and it can be shown that its probability distribution is given by (Bohren and Clothiaux, 2006):

$$PE_t dE_t = \frac{2}{(k_B T)^3} \sqrt{\frac{E_t}{\pi}} e^{-\frac{E_t}{k_B T}} dE_t \quad (2)$$

With a mean energy given by $\mu_{E_t} = k_B T/2$, which for a typical tropospheric temperature of 300 K represents $\sim 10^{-2} \text{ eV}$ per molecule, i.e., a speed of its center of mass of $\sim 10^2\text{--}10^3 \text{ m s}^{-1}$. Under these conditions, the mean free path for molecules in the atmosphere is in the order of $7 \times 10^{-6} \text{ m}$ (Jennings, 1988), so that the mean free time (average time between collisions) would be in the order of $\sim 10^{-9} \text{ s}$. This time is comparable to the lifetime (exponential decay) of an excited electronic state, but much shorter than typical excited vibrational or rotational states. Consequently, the de-excitation of vibrational/rotational energy levels (infrared and longer wavelengths) is controlled by collisions, meaning that radiation is strongly coupled with matter and that local thermodynamical equilibrium (LTE) holds. Conversely, radiative rather than thermal processes control the population of electronic energy levels beyond the UV/Vis spectral region and LTE is not necessarily achieved.

Due to the difference in mass between electrons and nucleons (protons, neutrons), the motion of the electrons can be considered independent of the motion of the nuclei (Born-Oppenheimer approximation). In this way the internal degrees of freedom correspond to the decoupled electronic, vibrational and rotational motions. Electronic transitions typically occur at energies observable in ultraviolet to visible spectral region. Vibrational energy is typically about 2 orders of magnitude smaller than the electronic energy which corresponds

⁵ $1 \text{ eV} \sim 1.602 \times 10^{-19} \text{ m}^2 \text{ kg s}^{-2}$

to transitions in the infrared region (~ 1 eV). The energies associated with rotational transitions lie in the far infrared to microwave spectral region ($\sim 10^{-2}$ – 10^{-4} eV).

The combined effect of rotational, vibrational and electronic transitions constitutes a problem that doesn't usually admit an analytical solution, and approximations dictated by the specific configuration of the studied system and invariance (symmetry) principles allow retrieving information of the structure and dynamics of molecules from their spectra. The state of the system then requires to be specified by a series of quantum numbers, for instance in Equation (3) below, a spectral "term" contains the contribution from electronic, vibrational and rotational levels represented by corresponding quantum numbers ($\nu = 0, 1, 2, \dots; J = 0, 1, 2, \dots$; etc.):

$$E = E_e + E_v + E_r = E_e + \hbar\omega_e\left(\nu + \frac{1}{2}\right) + \hbar B_e J(J + 1) \quad (3)$$

Where $E_e \gg \hbar\omega_e \gg \hbar B_e$, and $\hbar = h/2\pi$. More complicated expressions including corrective terms are necessary to account for the effect of "centrifugal distortion" of the rotation or "anharmonicity" in the vibration. An observable spectral line is calculated from the difference of the two terms involved in the transition, according to certain selection rules derived from e.g., conservation of angular momentum or change in the dipole moment. An schematic representation of the potential energy structure of HCl and resulting spectrum from vibro-rotational transitions is depicted in Figure 4. The development of this topic is beyond the scope of the work presented in this thesis, and the interested reader can find valuable sources of consultation elsewhere (Bransden and Joachain, 2003; Herzberg, 1950; Sakurai, 1967; Svanberg, 2003).

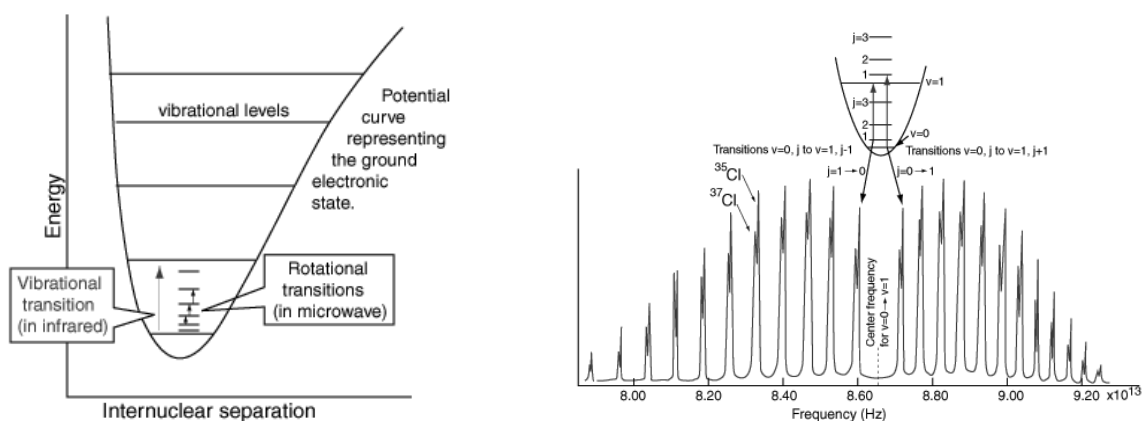


FIGURE 4. (Left) Schematics of the quantized structure of the potential energy of a molecule showing fine rotational levels within vibrational levels. (Right) Spectrum of HCl in the infrared region, corresponding to vibrational-rotational transitions at the ground electronic state and splitting due to isotopic speciation (Image courtesy of Rod Nave, HyperPhysics project: <http://hyperphysics.phy-astr.gsu.edu/hbase/hph.html>)

Radiation

The external radiation field (\vec{E}, \vec{B}) is described classically by the electromagnetic potential (ϕ, \vec{A}) through the relations (in the absence of charge sources):

$$\vec{E}(\vec{r}, t) = -\vec{\nabla}\phi(\vec{r}, t) - \frac{\partial \vec{A}(\vec{r}, t)}{\partial t} \quad (4)$$

$$\vec{B}(\vec{r}, t) = \vec{\nabla} \times \vec{A}(\vec{r}, t)$$

Where \vec{E} represents the electric field, \vec{B} the magnetic field, ϕ the scalar potential, and \vec{A} the vector potential, all of which are functions of space and time (\vec{r}, t) . (\vec{E}, \vec{B}) satisfy the Maxwell equations and it can be shown that \vec{A} satisfies the wave equation (Waters, 1993):

$$\nabla^2 \vec{A}(\vec{r}, t) - \frac{1}{c^2} \frac{\partial^2 \vec{A}(\vec{r}, t)}{\partial t^2} = 0 \quad (5)$$

Which admits solutions of the form:

$$\vec{A}(\vec{r}, t) = A_0(\nu) \text{Re}\left(e^{i(\vec{k} \cdot \vec{r} - 2\pi\nu t + \phi_\nu)}\right) \vec{\varepsilon} \quad (6)$$

Where $|\vec{k}| = 2\pi\nu/c$ represents the wave or propagation vector, ϕ_ν a frequency-dependent real phase and $\vec{\varepsilon}$ the polarization vector. Equation (6) corresponds to a transverse monochromatic wave ($\vec{k} \cdot \vec{\varepsilon} = 0$) propagating at the speed of light. The rate of radiant energy E flow crossing a unit area s is given by the Poynting vector $\vec{S}(\vec{r}, t) = \varepsilon_0 c^2 [\vec{E}(\vec{r}, t) \times \vec{B}(\vec{r}, t)]$, where ε_0 is the vacuum permittivity ($\sim 8.854 \times 10^{-12} \text{ m}^{-3} \text{ s}^4 \text{ kg}^{-1} \text{ A}^2$). The magnitude of the Poynting vector averaged over one period for a component of frequency ν is: $|\vec{S}| = 8\pi^2 \varepsilon_0 c \nu^2 A_0(\nu)^2$ (for incoherent radiation, this quantity includes the contributions from different waves at all polarizations⁶ for the different frequency components, which phases cancel out on average). This quantity is also called spectral irradiance I_ν (or intensity) and its quantum mechanical equivalent is the photon flux Φ_p , or number N of photons in a volume V that cross a unit of area per unit of time, both quantities being related by:

$$I_\nu = 8\pi^2 \varepsilon_0 c \nu^2 A_0(\nu)^2 = \frac{Nh\nu c}{V} = \Phi_p \quad (7)$$

By considering specifically the directionality of the radiation, i.e., the spectral irradiance coming from a direction θ per unit solid angle Ω , we arrive at the definition of spectral

⁶ Electromagnetic waves are polarized, and the field is fully represented by the polarization matrix, composed of Stokes vectors that describe the total intensity, and the levels of horizontal, vertical and elliptical polarization. In this thesis we refer only to the total intensity, because the instruments employed are not polarization-sensitive and the radiation from sky is to a large degree non-polarized.

radiance L_ν , or specific intensity, which can be considered as the elementary quantity defining a radiation beam:

$$L_\nu = \frac{dI_\nu}{\cos\theta d\Omega} = \frac{d^4E}{dt d\nu ds \cos\theta d\Omega} \quad (8)$$

Interaction

When an electromagnetic field interacts with a quantum system (electron, atom, molecule) at low energies and radiation intensities, three elementary processes may occur: the spontaneous emission of a photon when the system passes from a higher to a lower level of energy ($E_2 > E_1$), the absorption of a photon from the radiation field by the system to make the transition from a lower to a higher level of energy, or the stimulated emission of a photon by the system under the influence of the radiation field. The first two processes are proportional to the energy density of radiation. The probability of occurrence of each of these processes per unit time is respectively proportional to the Einstein coefficients B_{21} , B_{12} and A_{21} ⁷ and to the line-shape function of the transition $b(\nu, \nu_{12})$, which expresses the fact that monochromatic transitions cannot occur because of the nonzero probability of transitions given by Heisenberg's uncertainty relation, and macroscopically also due to pressure broadening due to collisions with other molecules and atoms in the gas phase or phonons in the condensed phase, and the thermal Doppler effect (Svanberg, 2003)⁸.

The rate of change with distance of specific intensity can be shown (e.g., Waters, 1993) to be given by:

$$\left. \frac{dL_\nu}{dl} \right|^{12} = \alpha_\nu^{12} (J_\nu^{21} - L_\nu) \quad (9)$$

⁷ Related by $g_1 B_{12} = g_2 B_{21}$ and $A_{21} = \left(\frac{8\pi h \nu^3}{c^3} \right) B_{21}$, where $g_{1,2}$ denotes the multiplicity of the involved states

⁸ The resulting shape of both the natural (uncertainty) and pressure broadening is Lorentzian:

$$b(\nu) = \frac{\gamma/2}{\pi[(\nu - \nu_0)^2 + \gamma^2/4]} \text{ with a characteristic linewidth } \gamma = \tau/2\pi, \tau \text{ being the decay time; whereas, for}$$

thermal broadening is Gaussian: with a $b(\nu) = \sqrt{\frac{4 \ln 2}{\pi}} \Delta \nu_D e^{-\left[\frac{4 \ln 2 (\nu - \nu_0)^2}{\Delta \nu_D^2} \right]}$ with linewidth

$$\Delta \nu_D = \frac{2\nu_0}{c} \sqrt{\frac{2 \ln 2 k_B T}{M}}, \text{ being } M \text{ the mass of the molecule}$$

Which is the differential radiative transfer equation (DRTE)⁹, where:

$$\alpha_\nu^{12} = n_1 B_{12} \left(1 - \frac{n_2 g_1}{n_1 g_2} \right) h\nu b(\nu, \nu_{12}) \quad (10)$$

Is the net absorption coefficient (absorption minus stimulated emission), and:

$$J_\nu^{21} = L_{\nu_{BB}} \frac{e^{\left(\frac{h\nu}{k_B T} - 1\right)}}{\left(\frac{n_1 g_2}{n_2 g_1} - 1\right)} \quad (11)$$

Is the net emission coefficient or source function (equal to the blackbody function $L_{\nu_{BB}}$ in thermodynamic equilibrium, see Equation 22).

The coefficient B_{12} is proportional to the square of the dipole operator M_{12}^ξ along direction ξ . Thus, the total absorption coefficient for radiation and matter with total number density¹⁰ n is given by¹¹:

$$\alpha_\nu = n \left(\frac{1}{4\pi\epsilon_0} \right) \frac{8\pi^3 \nu}{3hcQ(T)} \sum_{12} g_1 g_2 \left(e^{-E_1/k_B T} - e^{-E_2/k_B T} \right) b(\nu, \nu_{12}) \sum_{\xi} |M_{12}^\xi|^2 \quad (12)$$

Defining the optical depth from distance l to L as:

$$\tau_\nu(l, L) = \int_l^L \alpha_\nu(l') dl' \quad (13)$$

The DRTE becomes: $\frac{dL_\nu}{d\tau_\nu} = J_\nu - L_\nu$, and after integration, the integral radiative transfer equation (IRTE) is expressed by:

$$L_\nu(L) = L_\nu(0) e^{-\tau_\nu(0,L)} + \int_0^{\tau_\nu(0,L)} J_\nu e^{-\tau_\nu(l,L)} d\tau_\nu \quad (14)$$

⁹ For more than two non-coherent possible transitions, the DRTE should include all the contributions from individual

transitions: $\frac{dL_\nu}{dl} = \sum_{ul} \alpha_\nu^{ul} (J_\nu^{ul} - L_\nu)$

¹⁰ The mean number density of molecules n_l in state l at thermal equilibrium is related to the total number density n

by: $n_l = n \frac{g_l e^{-E_l/k_B T}}{Q(T)}$, where g_l are the degeneracy of state l and $Q(T) = \sum_j g_j e^{-E_j/k_B T}$ is the partition

function.

¹¹ The last factor in Equation 12 can be extended to include besides electronic, also vibrational and rotational transition matrix elements, the so-called Franck-Condon (vibrational) and Hönl-London (rotational) factors, which represent the level of overlapping of vibrational or rotational wavefunctions of the states associated with the transition

$$= L_\nu(0)e^{-\tau_\nu(0,L)} + \bar{J}_\nu [1 - e^{-\tau_\nu(0,L)}]$$

$$\text{Where: } \bar{J}_\nu = \frac{\int_0^{\tau_\nu(0,L)} J_\nu e^{-\tau_\nu(l,L)} d\tau_\nu}{\int_0^{\tau_\nu(0,L)} e^{-\tau_\nu(l,L)} d\tau_\nu}.$$

In a typical absorption experiment, the difference between intensities at a spectral line peak [$L_{\nu_{12}}(0,L)$] and at a nearby frequency [$L_{\nu_{12}}(0) \approx L_\nu(0)$] where negligible absorption occurs [$\tau_\nu(0,L) = 0$] is calculated, leading to:

$$\Delta L_{\nu_{12}}(L) = L_{\nu_{12}}(L) - L_\nu(0) = [\bar{J}_\nu - L_\nu(0)] [1 - e^{-\tau_{\nu_{12}}(0,L)}] \quad (15)$$

If $\Delta L_{\nu_{12}}(L) < 0$, the line is observed in absorption [$\bar{J}_\nu < L_\nu(0)$]; if $\Delta L_{\nu_{12}}(L) > 0$, the line is observed in emission [$\bar{J}_\nu > L_\nu(0)$]; and, if $\Delta L_{\nu_{12}}(L) = 0$, the line is not observable [$\bar{J}_\nu = L_\nu(0)$].

The optical depth of the transition can be readily calculated from Equation (15):

$$\tau_{12}(0,L) = \ln \left[\frac{L_\nu(0) - \bar{J}_\nu}{L_{\nu_{12}}(L) - \bar{J}_\nu} \right] \quad (16)$$

Equation (16) is a general expression for the so-called Bouguer-Beer-Lambert equation, which constitutes the basis for analysis by absorption spectroscopy.

Equation (9) was derived from microscopic considerations, but considering macroscopic radiation transport, density fluctuations add the effects of scattering (single, multiple and reflection in the surface). These are "source" terms that should be added to the RTE. In plane-parallel (slab) geometry:

$$\frac{dL_\nu}{dl_\nu} = -\varepsilon_\nu(l)L_\nu(l) + \alpha_\nu(l)J_\nu(l,T) + \frac{\sigma_\nu(l)}{4\pi} \int_{4\pi} p(l,\Theta)L_\nu(l,\Omega') d\Omega' + L_\nu^{sf} \quad (17)$$

Where the first term on the right represents extinction characterized by the extinction coefficient $\varepsilon_\nu(l) = \sigma_\nu(l) + \alpha_\nu(l)$ (the sum of scattering $\sigma_\nu(l)$ and absorption $\alpha_\nu(l)$ coefficients); the second term represents thermal emission; the third term represents multiple scattering, depending on the phase function $p(l,\Theta)$, where Θ is the scattering angle; and the last term represents surface emission. To solve this equation, a given geometry, boundary conditions and the source function (thermal, scattering, reflection), should be specified and adjusted iteratively. Equation (17) does not include explicitly the contribution of "inelastic" Raman scattering, which is thought to be the cause of the so-called "Ring effect" (Chance and Spurr, 1997; Vountas et al., 1998), a filling-in of molecular absorption structures that can be as large as the typical absorption of trace gases, especially for large solar zenith angles (sza).

The most important scattering processes in atmospheric spectroscopy in the optical region are debt to density fluctuations of particles much smaller than the wavelength of the radiation, as it is the case of molecules for optical wavelengths. This is called Rayleigh scattering. Another scattering process is debt to the interaction of radiation with particles comparable or bigger than the wavelengths, which is called Mie scattering for the case of

spherical particles. These processes are conservative, in the sense that the radiation field does not transfer energy to the matter. Non-conservative processes also occur, as it is the case of Raman scattering¹².

The Mie scattering cross section are derived analytically by solving Maxwell equations in spherical coordinates through separation of variables, expanding the incident field in spherical harmonics and matching continuity in the boundary. For distances much larger than the wavelength of the radiation (i.e., in the far field), the Mie extinction ε_M and scattering σ_M cross sections are given by:

$$\varepsilon_M(\nu) = \frac{2\pi}{k^2} \sum_{n=1}^{\infty} (2n'+1) \text{Re}(a_{n'} + b_{n'}) \quad (18)$$

$$\sigma_M(\nu) = \frac{2\pi}{k^2} \sum_{n=1}^{\infty} (2n'+1) (|a_{n'}|^2 + |b_{n'}|^2)$$

Where $k = 2\pi/\lambda$ is the radiation wavenumber and $a_{n'}, b_{n'}$ are complex expressions involving spherical functions of the parameter mka , being m the relative (complex) refractive index (index of refraction and absorption coefficient of the particle relative to the index of the medium), and a the radius of the scatterer (Hansen and Travis, 1974). In the limit $|m|ka \ll 1$, i.e., for wavelengths much larger than the size of the scatterers, the Rayleigh scattering cross section for molecules is obtained:

$$\sigma_R(\nu) \propto \nu^4 \quad (19)$$

Equation (19) shows the strong dependency on frequency (wavelength) of the radiation. This is the reason why scattering is dominant in the shorter wavelengths producing effects like the blueness of the daylight or the redness of the twilight. Furthermore, considering that the orientation of molecules plays a role in the coupling with the incident radiation field (polarizability), the effect of rotation or vibration alters the polarizability giving rise to the non-conservative Stokes and anti-Stokes lines of Raman scattering. The dependency of the Mie scattering cross section σ_M on frequency is complex but for a collection of particles can be approximated by a polynomial of low order (i.e., $\propto \lambda^{0 \dots 2}$, explaining the whiteness of the clouds). The angular distribution of Mie scattering usually is characterized by a very peaked forward scattering component, whereas for Rayleigh scattering the angular scattering diagram is symmetric respect to the incident radiation (Bohren and Huffman, 1998; Thomas and Stammes, 1999). Although varying over a relatively large range, typical molecular cross sections for absorption in optical wavelengths are in the order of 10^{-18} cm², whereas Rayleigh scattering cross sections are in the order of 10^{-26} cm², Raman scattering in the order of 10^{-29} cm², and Mie scattering in the order of 10^{-26} - 10^{-8} cm² (Svanberg, 2003).

¹² The term Rayleigh scattering sometimes includes the conservative component, called Cabannes line, and the series of higher or lower frequencies caused by rotational or vibrational scattering, called the Stokes and anti-Stokes lines (Young, A.T., 1982)

1.2.4. Instrumental considerations

In a spectroscopic measurement setup, the observation intervals for time Δt_m , spectral resolution $\delta \nu_m$ ¹³, detector area Δs_m , and solid angle $\Delta \Omega_m$ for radiation coming from direction θ_m with respect to the normal to the detector are pre-determined; thus, the measurement is directly related to the amount of spectral radiant energy gathered by the instrument E_m :¹⁴

$$E_m = \int_{\Delta t_m} \int_{\Delta \nu_m} \int_{\Delta s_m} \int_{\Delta \Omega_m} L_\nu dt d\nu ds \cos \theta d\Omega \quad (20)$$

However, the actual variable recorded by a digital electronic instrument or sensor is usually a digital number $E_{i,j}^*$ (for a detector i in band j) which is connected to the spectral radiant energy by an instrumental measurement equation of the type (Butler et al., 2005):

$$E_{i,j}^* = R_{i,j} E_{mi,j} \quad (21)$$

Where $R_{i,j}$ represents the total responsivity of the sensor which includes the effects of detector spectral, spatial, temporal and polarization responsivities, amplification and digitalization gains, transmittance or reflectance of optical elements, slit transmission function, etc. The measurement equation guides the characterization, calibration and uncertainty analysis of the measurements (Datla and Parr, 2005). For calibration purposes, for instance, a radiometric calibration implies the comparison of an unknown spectral radiance with a standard source, like a tunable laser source or an approximate blackbody source, for which the spectral radiance $L_{\nu_{BB}}$ at an equilibrium temperature T is given by the expression:

$$L_{\nu_{BB}}(T) = \left(\frac{2h\nu^3}{c^2} \right) \frac{1}{e^{\left(\frac{h\nu}{k_B T} \right)} - 1} \quad (22)$$

Although radiometric calibration is an important and sometimes necessary step for remote sensing applications, in some cases we are interested only on relative measurements, where the ratio of two measured signals with unknown absolute spectral radiance is taken, and absolute calibration is not needed. This is the case considered in this work.

The frequency/wavelength scale should also be calibrated in a spectrometer, for which a source with known features is usually used, for example the so-called Fraunhofer lines in a solar spectrum or the emission lines of an inert gas like Hg or Xe, or a laser comb. For the UV spectrometers used for the studies presented here, solar and Hg-lamp methods were used for

¹³ This resolution refers to the full-width-at-half-maximum (FWHM) of the response of the spectrometer to monochromatic radiation at the given frequency. A more appropriate factor to quantify the resolution of a spectral apparatus is the resolving power, defined as $\lambda/\delta\lambda$ for radiation at wavelength λ and line separation $\delta\lambda$.

¹⁴ For a system immersed in a medium with an index of refraction n_m the so called étendue $n_m^2 \Delta s_m \cos \theta_m \Delta \Omega_m$ is an invariant, and therefore the quantity L_ν / n_m^2 is conserved in a non-absorbing medium.

frequency calibration. For the IR interferometer, an internal laser source is used for precise frequency calibration.

The slit function represents the spectral resolution of a spectrometer, because it corresponds to the response of the spectrometer to a spectral feature that is narrower than the slit of a dispersive instrument. The same low pressure Hg-lamp spectrum used for frequency calibration of the UV spectrometers was used for characterizing the slit function at a wavelength of 302.1495 nm¹⁵, which lies close to the spectral region of interest for spectroscopy of SO₂. This characterization makes the assumption that the same slit function applies to all wavelengths, but wavelength-invariance is not common because of the angular dependency of the dispersive mechanism of the spectrometers. For the FTIR method, the resolution is determined by factors like the entrance aperture and path-difference of the arms of the interferometer.

No measurement is exempt from noise either due to fundamental reasons (like quantum fluctuations) or due to effects introduced by each step of the measurement. Noise can be reduced or characterized but usually not eliminated. If we limit the discussion of these effects to what happens at the detector itself, the most important sources of noise can be classified as those due to the incoming signal (photon/shot/background noise) and those due to the electronics of photodetection (thermal/Johnson-Nyquist noise, amplification noise, read-out noise, digitalization noise). In the thermal infrared region the background signal is relatively important, while in the UV/Vis the photon noise is more significant. The ratio of the radiant power of the signal to be measured to the power measured when no external signal is present defines the signal-to-noise ratio S/N . When this ratio is equal to unity, the signal is called the noise-equivalent-power NEP , i.e., the power of a signal that equals 1 root-mean-square (rms) of the fluctuating noise signal. For a detector with a quantum efficiency of η photoelectrons per incident photon, a signal of radiant power P_s will induce a current given by $i_s = \eta e P_s / h\nu$, where e represents the electron's charge¹⁶. In this case, it can be shown (Kingston, 1995) that the mean square noise current is given by $\bar{i}_n^2 = 2\eta e^2 (P_s + P_b) \Delta f / h\nu + 4k_B T_N \Delta f / R_{in}$, where the first term contains the contribution from a signal dependent (P_s) and background dependent (P_b) noise, and the second term the contribution of the equivalent noise temperature T_N and input resistance R_{in} of the detector with electrical bandwidth Δf . Thus, the total S/N can be expressed as:

$$\frac{S}{N} = \frac{P_s}{\sqrt{\frac{2P_s h\nu \Delta f}{\eta} + \frac{2P_b h\nu \Delta f}{\eta} + \left(\frac{h\nu}{\eta e}\right)^2 \frac{4k_B T_N \Delta f}{R_{in}}}} \quad (23)$$

If a detector array is used, and additional detector noise term due to read-out should be added, which is proportional to the number of elements in the array.

¹⁵ Corresponding to a transition from the 44042.977 cm⁻¹ ($J=2$) to the 77129.535 cm⁻¹ ($J=3$) electronic energy levels in air (Kurucz, R.L. and Bell, B., 1995).

¹⁶ $e \sim 1.602 \times 10^{-19}$ C

Another important figure of merit for a detector is the specific detectivity $D^* = \sqrt{S\Delta f} / NEP$, which introduces the effect of the size of the detector S in the detectivity and it is therefore a useful quantity for comparison of different detectors.

2. Measurement techniques and data analysis

"The smell of sulfur is strong, but not unpleasant to a sinner."

— Mark Twain ¹⁷

In this chapter, we present the remote sensing techniques: Differential Optical Absorption Spectroscopy (DOAS) and Fourier Transform Infra-Red (FTIR) spectroscopy, which have been used for the measurements of volcanic gases reported in this thesis.

2.1. Inversion of remote spectroscopic sensing data

The retrieval of information from a remote spectroscopic sensing measurement constitutes an inverse problem: the objective is to derive certain variables and parameters defining the physical state of the observed system from the observed effects. Thus, the inversion includes a forward model containing certain parameter, which reflects the knowledge of the system, to relate measurements with the modeled variables. In the case of this work, the observed effect is the measured spectrum, and the variables to retrieve are the column densities of trace gases in the atmosphere. The retrieval procedure is iterative: from an initial guess of the variables and parameters, a model spectrum is calculated and compared with the measured spectrum. The comparison is done through a cost function and the iterations proceed to minimize such function by varying the values of the variables and parameters until an acceptable value is achieved. If the iteration converges, the retrieved values and the residual (difference between the modeled and measured spectra) determine the results of the measurement. One iterative or fitting function is the least-squares norm. The sum of squares of the normalized residuals should follow a Chi-square distribution if the residuals are effectively random, reflecting only the noise in the measurement. For non-linear minimizing functions, a common fitting method is the Levenberg-Marquardt iterative algorithm (Levenberg, 1944; Marquardt, 1963), which is a combination of a gradient and a Gauss-Newton method. Another algorithm widely used in atmospheric sounding inversion is the Optimal Estimation Method, based on a Bayesian approach (Rodgers, 2000).

The process leading to passive remote sensing of molecules by spectroscopy can be described in the following steps (e.g., Wenig et al., 2005):

1. Radiation is emitted from a source. If this is the sun, it has emission characteristics that can be approximated by a blackbody source function at an effective temperature of 5778 K. The spectrum is not smooth, but has structures from absorption of atoms and molecules in the solar atmosphere, known as Fraunhofer lines. In the UV the spectrum has a variability of about 1%, and lower in the IR; the spectrum also varies along the radius of the solar disc, an effect known as "limb darkening", due to the heterogeneous density distribution of the sun.

¹⁷ Remembering a visit to Kilauea, 1866

2. Radiation enters the atmosphere and it undergoes extinction, including both absorption by gases and Rayleigh, Mie or Raman scattering, as well as refraction due to large scale density gradients in the atmosphere. These effects depend on the vertical and horizontal structure of the atmosphere in terms of composition, temperature, pressure and cloudiness. Any “polluting” cloud, like a volcanic plume also exerts an effect on the radiation transport.
3. The radiation is collected and analyzed by an instrument. In the front-end the transfer optics couples with the radiation field at a given direction (solid angle) and transmits it to the spectral analyzing component, either a dispersive element like a prism, grating or beamsplitter, or a non-dispersive filter. The radiation is then detected by a sensor, amplified and digitalized. Co-adding several spectra in order to improve the S/N is usually performed in the instrument.
4. The digital spectrum is analyzed. This analysis usually corresponds to an inversion, as discussed before. Some correction measures, like offset/dark current subtraction, co-averaging of multiple spectra, or discarding over-attenuated or saturated spectra, are normally performed before the actual analysis. The forward model should include parameters that are known, e.g., instrumental characteristics or high-resolution spectra of absorbing molecules, and parameters to retrieve, like the slant column densities of gases, as well as irreducible errors. The results are obtained from the inversion procedure. These depend on the specific problem, but include both the retrieved variables and their associated uncertainties.

The specific procedures for DOAS and FTIR are discussed below.

2.2. DOAS

Differential Optical Absorption Spectroscopy -DOAS- (Platt and Stutz, 2008) is a spectrometric analysis method for the quantification of trace gases concentrations based on the principles of absorption spectroscopy (Bouguer-Beer-Lambert law). A broad-band absorption spectrum can always be modeled as a signal that has “high frequency” and “low frequency” components, where the dividing criterion or cut-off frequency is determined by the characteristics of the spectrum itself and the spectral range and resolving power of the instrument. The high frequency or “differential” absorption signatures are related principally to the absorption structure of the spectra, whereas the lower frequency components typically correspond to broad-band absorption, scattering and instrumental effects (like the transmission of optical components).

According to the 4-step scheme presented above, a measured solar spectrum is the product of the following transformations:

1) The direct solar beam is not measured in the passive DOAS method used in the field studies reported in this work. DOAS has been used in direct solar/lunar/star mode in other circumstances (Herman et al., 2009), and of course, active DOAS has been used with different sorts of sources like LEDs or Xe lamps (Kern et al., 2006; Platt and Stutz, 2008). The solar spectrum is however the “driving” source of the scattered spectrum that is measured and its known structure is caused of various effects, including the “ I_0 -effect” (Platt and Stutz,

2008) of highly structured features that cannot be resolved by low-resolution spectrometers and that show up as pseudo absorbers in the DOAS methods; also the amount of “Ring-effect” (Chance and Spurr, 1997; Vountas et al., 1998) or filling-in of molecular absorption structures caused by rotational, and to a lower extent also vibrational, Raman scattering is scaled with the intensity of the solar beam. On the other hand, the known structure of the Fraunhofer lines can be used as a marker for self-calibration of the wavelength scale of the spectra (van Geffen and van Oss, 2003).

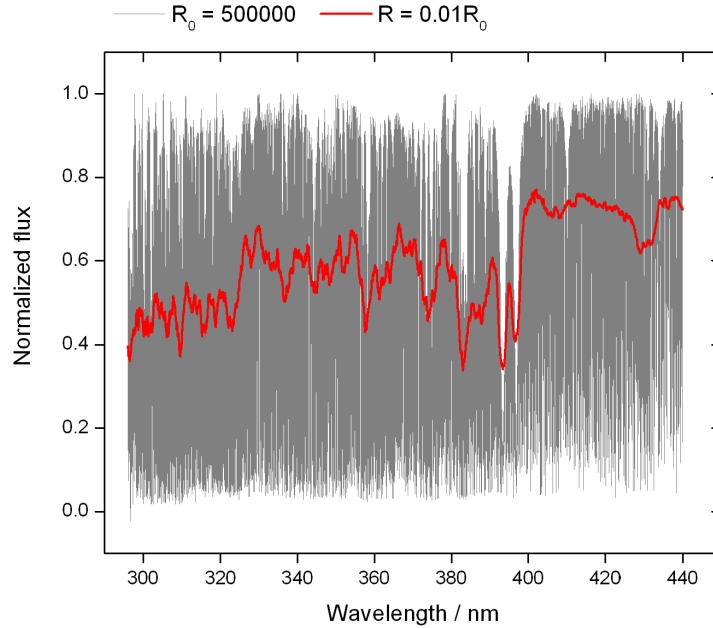


Figure 5. Section of the UV solar flux (irradiance) spectrum (Kurucz et al., 1984) between 296 and 440 nm. The spectrum in gray was measured with a Fourier transform spectrometer at a resolving power of 5×10^5 (at the central wavelength). The spectrum in red is a smoothed version at 1% resolution, similar to what would be measured by the UV spectrometers used for volcanic gas measurements. The structures in the spectrum can be used as stable markers for wavelength calibration of the measurements

2) For diffuse radiation in the near UV spectral region, the leading terms in the RTE (Equation 17) correspond to extinction and multiple scattering, since emission is negligible at atmospheric temperatures and surface reflectivity is usually low for most soil types. The spectrum measured at surface then reduces to:

$$\frac{dL_v}{dl_v} = -\varepsilon_v(l)L_v(l) + \frac{\sigma_v(l)}{4\pi} \int_{4\pi} p(l, \Theta)L_v(l, \Omega')d\Omega' \quad (24)$$

Which formal solution in terms of total optical depth $\tau_v(l, L) = \int_l^L \varepsilon_v(l')dl'$, single scattering albedo $a(l) = \sigma(l)/\tau(l)$ and the factor $u = \cos(\theta)$ (correcting for vertical component), can be represented by:

$$L_v(\tau_v, \Omega) = L_v(0, \Omega)e^{-\tau_v/u} + \int_0^{\tau_v} \left[\frac{a_v(\tau'_v)}{4\pi\epsilon_v(\tau'_v)} \int_{4\pi} p(\tau'_v, \Theta) L_v(\tau'_v, \Omega') d\Omega' \right] \frac{e^{-(\tau'_v - \tau_v)/u'}}{u'} d\tau'_v \quad (25)$$

In fact, this radiance has a direct solar component L_v^s and a diffuse component L_v^d . The measurements we are interested in contain only the latter term; however, the direct component is inherently included in the scattering term. The measured radiance then can be expressed as:

$$\begin{aligned} L_v^d(\tau_v, \Omega) &= \\ &= L_v^d(0, \Omega)e^{-\tau_v/u} + \int_0^{\tau_v} \left[\frac{a_v(\tau'_v)}{4\pi} \int_{4\pi} p(\tau'_v, \Theta) [L_v^s(\tau'_v, \Omega') + L_v^d(\tau'_v, \Omega')] d\Omega' \right] \frac{e^{-(\tau'_v - \tau_v)/u'}}{u'} d\tau'_v \\ &= L_v^d(0, \Omega)e^{-\tau_v/u} + \int_0^{\tau_v} \left[\frac{a_v(\tau'_v)}{4\pi} p(\tau'_v, \Theta^s) F^s e^{-\tau'_v/u^s} \right] \frac{e^{-(\tau'_v - \tau_v)/u'}}{u'} d\tau'_v \\ &+ \int_0^{\tau_v} \left[\frac{a_v(\tau'_v)}{4\pi} \int_{4\pi} p(\tau'_v, \Theta) L_v^d(\tau'_v, \Omega') d\Omega' \right] \frac{e^{-(\tau'_v - \tau_v)/u'}}{u'} d\tau'_v \end{aligned} \quad (26)$$

Where F^s is the extraterrestrial solar irradiance or solar flux. Equation (26) indicates that the radiance reaching the sensor at surface is the contribution from the diffuse radiance on top of the medium attenuated by extinction; plus the direct solar radiance attenuated by extinction, single-scattered to the detector, and further attenuated by extinction; plus the diffuse radiance multiply scattered and attenuated by extinction towards the sensor. If the single scattering albedo is small, the contribution from multiple scattering is minor and may be neglected. Furthermore, the overlaying radiance $L_v^d(0, \Omega)$ may be considered null for a sensor at the surface in the single scattering approximation, since the scattering events that produce this term occur in the upwelling direction. Modeling of this radiation field from first principles require advanced computational programs that divides the atmosphere in layers with specific geometry and properties such as composition, pressure, temperature, number density, scattering and absorption cross sections, single scattering albedo, the position of the sun with respect to the sensor, and polarization corrections (Hansen and Travis, 1974; Thomas and Stammes, 1999). The actual solution to the problem can be found by different approaches, for instance by Monte Carlo simulation of photonic trajectories (Kern et al., 2010).

For a single-scattering Rayleigh atmosphere, the incoming radiance reaching the surface is represented by:

$$L_v^d(\tau_{v,x}, \Omega) = F^s \frac{a_v}{4\pi} p_R(\Theta^s) \frac{u^s}{(u^s - u)} \left(e^{-\tau_v/u^s} - e^{-\tau_v/u} \right) \quad (27)$$

This expression indicates that radiation detected at the surface is a function of solar zenith angle and observation angle and its origin is distributed along the line of sight at different altitudes. If an absorbing layer, like a volcanic plume, is present at certain altitude, only the radiation above the layer is further attenuated by the plume, whereas the radiation originated below the layer does not contain absorption features and therefore "dilutes" the effect of absorption. Representing the radiation above and below the layer by $L_{v,above}^d$ and $L_{v,below}^d$, respectively, the total radiance is expressed by:

$$L^d_{\nu}(\tau_{\nu} + \tau_{\nu,x}, \Omega) = L^d_{\nu,above}(\tau_{\nu,above}, \Omega)e^{-\tau_{\nu,x} \times amf_{\nu}} + L^d_{\nu,below}(\tau_{\nu,below}, \Omega) \quad (28)$$

Where $amf_{\nu} = \tau_{\nu,x} / \tau_{\nu}^{\nu} \approx \int_s n(s) ds / \int_{\nu} n(\nu) \nu = SCD/VCD$ is the air-mass factor relating the slant optical depth $\tau_{\nu,x}$ to the vertical optical depth τ_{ν}^{ν} , and which is equivalent to the ratio of the slant column density SCD to the vertical column density VCD when the extinction inside the plume is independent on the optical path ($\epsilon_{\nu,x} \neq \epsilon_{\nu,x}(l)$).

Note that from equation (37) the VCD_x is equal to:

$$VCD_x = \int_{\nu} n(\nu) d\nu = \frac{\ln \left[\frac{L^d_{\nu,above}(\tau_{\nu,above}, \Omega)}{L^d_{\nu}(\tau_{\nu} + \tau_{\nu,x}, \Omega) - L^d_{\nu,below}(\tau_{\nu,below}, \Omega)} \right]}{\epsilon_{\nu,x} \times amf_{\nu}} \quad (29)$$

If the radiation below the plume can be neglected, by combining two spectra from directions towards Ω and outside Ω' the plume, the column is obtained from:

$$VCD_x = \frac{\ln \left[\frac{L^d_{\nu}(\tau'_{\nu}, \Omega')}{L^d_{\nu}(\tau_{\nu} + \tau_{\nu,x}, \Omega)} \right]}{\epsilon_{\nu,x} \times amf_{\nu}} \quad (30)$$

This approximation is not always accurate, since the component of foreground radiation may be significant at large instrument-plume distances.

3) The measured spectra are altered by the optics, spectral dispersion, detection, and digitalization. The optical elements usually modify the incident field by a slowly varying

transmission function $T(\nu) = \prod_i^n T_i(\nu)$ incorporating the functions of each optical element.

The spectrometer response is characterized by the instrumental line-shape (ILS) function, which in the case of a grating spectrometer depends on the optical resolution given by the order of dispersion q and the number of lines illuminated in the grating z by the relation $\Delta\nu/\nu = 1/qz$, as well as on the line-spread-function (imperfect imaging of the slit caused by the optics). The convolution of both functions defines the ILS which on the spectrometers used for DOAS measurements depends on wavelength and is determined by measuring the lines of a spectrum of a low-pressure Hg lamp, as represented in Figure 6.

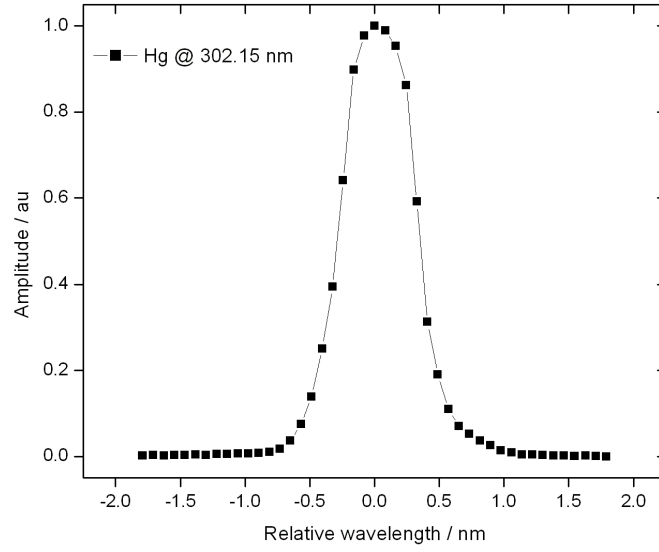


Figure 6. Example of ILS used for calibration of DOAS instruments. The FWHM is about 0.6 nm

The detector of the UV spectrometers is a CCD array of 2048 elements for a typical spectral range of 150 nm (~270-420 nm). The detector is not inherently sensitive to UV radiation, but rather makes use of a shorter wavelength sensitive fluorescent coating. Coupled to the detector is the amplification, digitalization (12 bits for the spectrometers used) and linearity correction systems. It is noteworthy that for an array detector there is an inter-pixel variation in responsivity R_ν . Furthermore, the effects of stray light, detection, digitalization, etc. produce offset and dark current on top of the photon-statistics noise. The noise is thus composed of systematic instrumental effects N^s_ν and random photon noise N^r_ν . The spectrum upon these processes is a vector of discrete spectral elements represented by:

$$L^*_\nu = \frac{\int_{\Delta t_m} \int_{\Delta \nu_m} \int_{\Delta s_m} \int_{\Delta \Omega_m} \int_{\delta \nu} [R_\nu (T_\nu L_\nu \otimes ILF)] dt d\nu ds \cos \theta d\Omega}{\int_{\Delta t_m} \int_{\Delta \nu_m} \int_{\Delta s_m} \int_{\Delta \Omega_m} \int_{\delta \nu} dt d\nu ds \cos \theta d\Omega} + N^s_\nu + N^r_\nu \quad (31)$$

The relation between the pixel position and the wavelength spectral element $\delta \nu$ is established via calibration, by fitting a (quasi-linear) third order polynomial. In laboratory tests, a Hg lamp spectrum was also used for this purpose, but in the field, the position of the Fraunhofer lines in the solar spectrum can be used instead. This relation may vary due to thermal stress or other causes, and therefore wavelength-pixel shift and squeeze operations are usually necessary to correct for these effects.

4) Once the spectrum has been recorded, the S/N can be improved by averaging a number of spectra, since this procedure will increase this ratio as the square-root of the number of averaged spectra. Dark/offset subtraction is then applied. The ultimate source of noise in the UV should be linked to the statistics of radiation detection (shot or photon noise which is a Poisson-like process), thus dark current and offset, as well as digitalization noise (due to truncation/round-off in the quantization), and inter-pixel variability should be properly subtracted. Dark current can be modeled by measuring a spectrum with the optics

unexposed to external radiation, offset is usually taken from permanently blocked pixels in the spectrometer, the digitalization noise and inter-pixel variability can be measured in the laboratory. These effects are usually dependent on temperature and even the intensity of measured radiation. In the measurements here reported, a first order noise cancellation was performed by a simple subtraction of a dark-offset spectrum taken under non-illuminated conditions. Inter-pixel variability and digitalization noise can be cancelled by taking the ratio of spectra taken under similar conditions and in close time proximity.

The next step consists in trying to reproduce the observed spectrum by a model and from the comparison of the model $\vec{f}(\vec{x}, \vec{b}, \vec{\varepsilon})$ with the measurement \vec{y} derive certain unknown variables \vec{x} and a-priori parameters \vec{b} and errors $\vec{\varepsilon}$, most importantly; in this case, the slant column densities SCD of atmospheric trace gases. The retrieved SCD are those that minimize an appropriate measure of the fitting, for instance the least squares norm:

$$\min \|\vec{y} - \vec{f}(\vec{x}, \vec{b}, \vec{\varepsilon})\| = \min \sum_{i=1}^n [y_i - \vec{f}(x_i, b_i, \varepsilon_i)]^2 \quad (32)$$

Where n represents the number of spectral elements or channels used in the fitting. The DOAS inversion usually takes as the measurement the optical depth and its model approximates the slowly varying part of the optical depth by a low order (usually ≤ 5) polynomial and the rapidly varying part by a weighted sum of absorption cross sections of the expected molecules present in the spectral range of analysis. The weights of the sum are the SCD . The implementation of this algorithm can incorporate absolute or differential (high-pass filtered) cross sections. In the latter case, the same filter should be applied to the measured optical depth. The solution is found iteratively until a value under a threshold (e.g., 10^{-4}) is reached for the chi-square of the fitting or until a maximum number of iterations (e.g., 5000) have been performed. Once a solution is found, the residual (difference between measured and model functions) is scaled to absorption optical depth of the gas of interest to estimate the uncertainty of the retrieval. The minimizing function takes then the form:

$$\min \sum_{i=1}^n (\tau_{i_x}^{meas} - \tau_{i_x}^{model})^2 = \min \sum_{i=1}^n \left\{ \ln \left[\frac{L_v^*(\tau'_i, \Omega') - N^{s'_{vi}}}{L_v^*(\tau_{i_x} + \tau_i, \Omega) - N^{s_{vi}}} \right] - \left[\sum_{j=0}^p c_j \lambda^j_i + \sum_{k=1}^q SCD_k \alpha_{ki} \right] \right\}^2 \quad (33)$$

It is important to emphasize that the ratio of two measured radiances cancels out most of the common instrumental effects and that usually $N^{s'_{vi}} \approx N^{s_{vi}}$. Moreover, the major asset of DOAS consists in separating high and low frequency components of the optical depth. If the measurement is done under non-ideal conditions, the ratio of radiances taken at different directions would include a complicated function of different variables: the optical depths, single scattering albedoes, phase functions, and directions of observation and of solar position for both measurements. This ratio would not give directly the differential optical depth of the target cloud, but if the terms related to scattering have low variation with wavelength, the DOAS algorithm can effectively separate the effects of absorption from scattering.

For an ideal retrieval, the minimized function should converge to the variance σ^2 of the measurement (related to the random error in measured radiance):

$$\min \sum_{i=1}^n (\tau_{ix}^{meas} - \tau_{ix}^{model})^2 = (n-1)\sigma_{\tau_x}^2 \quad (34)$$

The uncertainty in the retrieved VCD_j of a component j is calculated from:

$$\sigma_{VCD_j} = \frac{\sigma_{\tau_x}}{\varepsilon_j^* \times amf_j} \quad (35)$$

Where ε^* denotes the plume extinction coefficient for absorption spectroscopy or the plume (differential) absorption coefficient for differential absorption spectroscopy. An example of a DOAS evaluation for the measurement of BrO, O₃ and O₄ is shown in Figure 7.

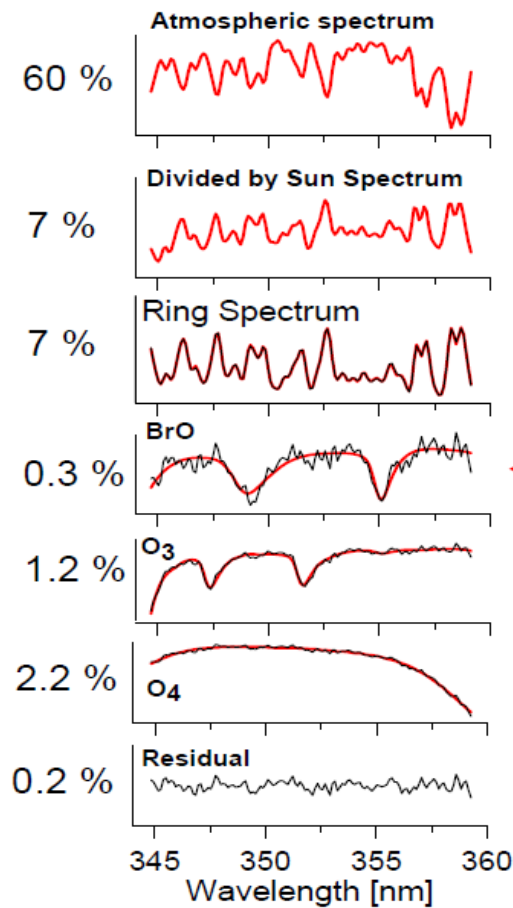


Figure 7. Example of a DOAS evaluation performed in the wavelength range of 345-360 nm, including a Fraunhofer spectrum and the absorption cross-sections of BrO, O₃, O₄, and a Ring spectrum. The measurement is shown in black and the fitted spectra in red. Also shown are the residual and the percentage of the signal for each component (courtesy of IUP-Uni-Bremen DOAS group)

2.2.1. DOAS measurements of volcanic gas emission rates

A DOAS measurement provides the *VCD* of the absorbers of interest in the plume. The estimate of the total emission rate of the measured gas requires integrating such measurements along the path in transversal direction to the plume and multiplying the product with the plume velocity. This problem can be analyzed from the perspective of mass conservation in a box enclosing the volcano and surrounded by a surface defined by the scanning path of the DOAS sensors, as sketched in Figure 8.

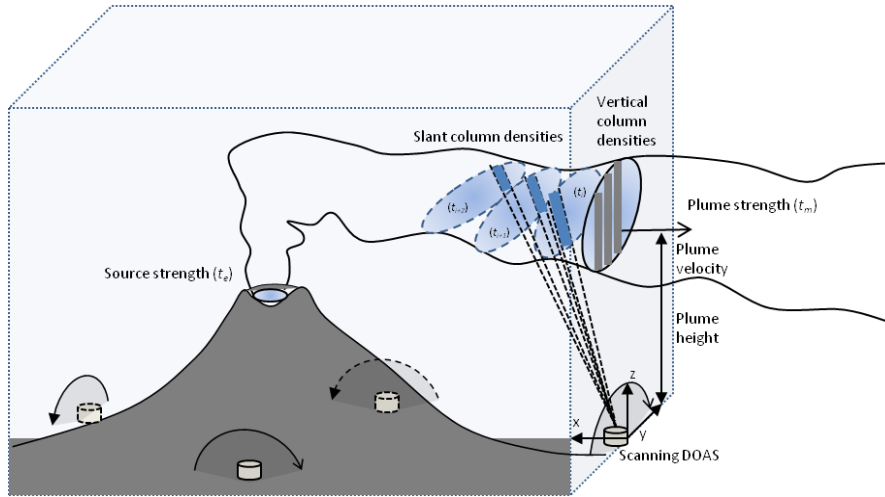


Figure 8. Schematics representing mass conservation in a box to derive the emission rate of a volcanic gas from scanning DOAS measurements. The surface integral of the gas number density multiplied by the normal wind speed plus any accumulation in the volume equals the volumetric source strength minus the total volumetric sink strength

According to the mass conservation equation, obtained as the zeroth velocity moment of the Boltzmann transport equation neglecting body forces (e.g., gravity), the total time derivative of the mass density of a species ρ_j , equals the net rate of production per volume of the species, i.e., the difference between volumetric rate sources q_j and sinks p_j :

$$\frac{d\rho_j}{dt} = \frac{\partial\rho_j}{\partial t} + \vec{\nabla} \cdot \vec{j}_j = q_j - p_j \quad (36)$$

Where the current density $\vec{j}_j = \vec{j}_j^{adv} + \vec{j}_j^{dif}$ is the sum of an advective term $\vec{j}_j^{adv} = \rho_j \vec{c}_j$ (\vec{c}_j is the advective transport velocity) and a diffusive term $\vec{j}_j^{dif} = -(K_j + D_j) \vec{\nabla} \rho_j$ (K_j is the turbulent mass diffusion coefficient and D_j is the molecular diffusion coefficient). Integrating this equation in a volume enclosing the source gives:

$$\begin{aligned}
\frac{dm_j}{dt} &= \iiint_V \frac{d\rho_j}{dt} dV = \iiint_V \frac{\partial\rho_j}{\partial t} dV + \iint_S \vec{j}_j \cdot d\vec{S} = \iiint_V (q_j - p_j) dV \\
&\Rightarrow \frac{\partial m_j}{\partial t} + \vec{c}_j \cdot \int_y \left(\int_z \rho_j dz \right) dy - (K_j + D_j) \iint_S \vec{\nabla} \rho_j \cdot d\vec{S} = Q_j - P_j \\
&\Rightarrow Q_j = \dot{m}_j + c_{j_x} \int_y VCD_j dy - (K_j + D_j) (\partial_x \rho_j) S + P_j
\end{aligned} \tag{37}$$

Where the Stokes theorem has been used to transform volume V to surface S integrals and a Cartesian system of coordinates has been used with x pointing in the longitudinal, y in the transversal and z in the vertical directions. Equation (37) states that the net rate of production or source strength of a gas species Q_j is equal to the sum of the rate of accumulation of the material inside the volume $\dot{m}_j = \partial m_j / \partial t$, the advective $c_{j_x} \int_y VCD_j dy$ and diffusive $-(K_j + D_j) (\partial_x \rho_j) S$ fluxes across the surfaces of the volume, and the net rate of destruction or sink strength of the species P_j . Ground-based remote sensing measures the advective term to estimate the source strength of volcanic emission, thus the approximation is better if diffusion, accumulation and sinks are either unimportant or properly accounted for.

The observation volume is naturally defined by the scanning planes of the instruments, which in some cases have complete azimuthal coverage of the volcanic plumes. From below the volume is bounded by the ground, and from above it may not be bounded (although conical scanning geometries may indeed enclose the sources also from above) but generally emissions at high, e.g., stratospheric altitudes, would not be accurately measured by typical instrumental DOAS networks. The advection is controlled by the local wind fields and determine one or more (in the case of crosswinds) prevalent directions. This term usually predominates over diffusion, and thus the main role of the diffusive flux is spreading the plume in the transverse directions. The source strength for a species like SO_2 is generally dominated by crater plume emissions, since fumarolic and flank emissions are usually negligible in comparison, although flank emissions may be important for species like CO_2 at some volcanoes (Allard et al., 1991). Another possible source of SO_2 is chemical reactions, especially the oxidation chain of H_2S . Accumulation inside the volume may be caused by processes like deposition or stagnant local wind fields. Different sink processes may be present, including chemical reactions, adsorption and solution in wet (e.g., sulfuric acid aerosols) or dry (e.g., tephra) surfaces, or dilution to a concentration below the limit of detection of the method. The presence and magnitude of each of these terms depends on various factors like the volcanic activity and composition of emissions, the local meteorological conditions, the surrounding topography, and the observation conditions (distance to crater, distance to plume, and scanning geometry).

The role of diffusive transport is important. In the longitudinal direction it tends to smooth out or spatially expand the heterogeneities in concentration and adds a component of transport that, under certain circumstances, can represent a considerable fraction of the total mass transport. In the transversal direction, on the other hand, diffusion expands the plume dimensions and in this way dilutes the concentration, which affects the limit of detection. The lateral spread is determined by the magnitude of the gradient of concentration and the diffusivity, which in turn depends on atmospheric conditions. Naturally, the plume width

increases by diffusion with distance from the source, and this effect can be used to estimate approximately the total transport speed if the diffusivity, which is dependent usually on altitude and atmospheric stability, is properly constrained. The basic idea is that by measuring the width of the plume Δy at its centre-of-mass altitude z and by estimating the transport time $t_p = d_p / c_p$ of the plume (d_p is the distance travelled from the source), the plume transport speed c_p can be calculated from values of the diffusivity at that altitude $K_y(z)$:

$$\begin{aligned}\Delta y(z) &\propto \sqrt{K_y(z)t_p} = \sqrt{K_y(z)\frac{d_p}{c_p}} \\ \Rightarrow c_p &\propto \frac{K_y(z)d_p}{[\Delta y(z)]^2}\end{aligned}\tag{38}$$

2.2.2. Scanning DOAS instrument

The introduction of the mini-DOAS instrument for volcanic gas studies arguably represented the most important innovation in remote sensing technology since the establishment of the COSPEC as a standard in this field (Galle et al., 2003). It also motivated the development of other techniques like the SO₂ cameras and the refinement of spectroscopic analytical procedures that allow the identification of other species in volcanic plumes (Bobrowski et al., 2003) and the reduction of certain source of uncertainty in the measurements like radiation transport or plume velocity (Johansson et al., 2009).

The scanning DOAS is a double channel multi-axis (MAX) DOAS instrument (Hönninger et al., 2004). It consists of a flat or conical scanning UV telescope connected to a double grating spectrometer via two slightly off-focused optical fibres. Alternatively, a single-beam configuration has one channel and an in-focus optical fibre. The spectrometer and the driving, recording and transmitting electronics is housed at a distance from the scanning head for protection and versatility of installation. Time and position is determined with a GPS antenna and the temperature inside the box is measured by a small IC sensor. The spectral, GPS and thermal data is integrated and recorded in an internal memory or transmitted via a radio-link. Remote instrumental control and data analysis is done with the "NovacProgram" software. Details of the instrumentation and software can be found in (Galle et al., 2010; Johansson, 2009).

The scanner is common to the two channels, which are used for zenith-looking observations at slightly different directions along the plume axis. The obtained gas time series are similar but shifted in proportion to the plume speed in the direction of observation¹⁸. The cross-correlation of the signals provides the best time shift, which combined with the spatial separation of the simultaneous sections of the plume seen by the two channels (dependent on the distance to the plume and the constant angular separation of the field of views),

¹⁸ Assuming that non-periodical heterogeneities in the gas column densities are present. Such variations may be caused by inhomogeneous emission rates, eddies, meandering or fluctuations in wind speed. Typical variations in the observed column densities can be as large as 50%.

provides the mean transport speed along the observed axis. Figure 9 shows a sketch of the principle of measurement and data obtained from its application to a real volcanic plume.

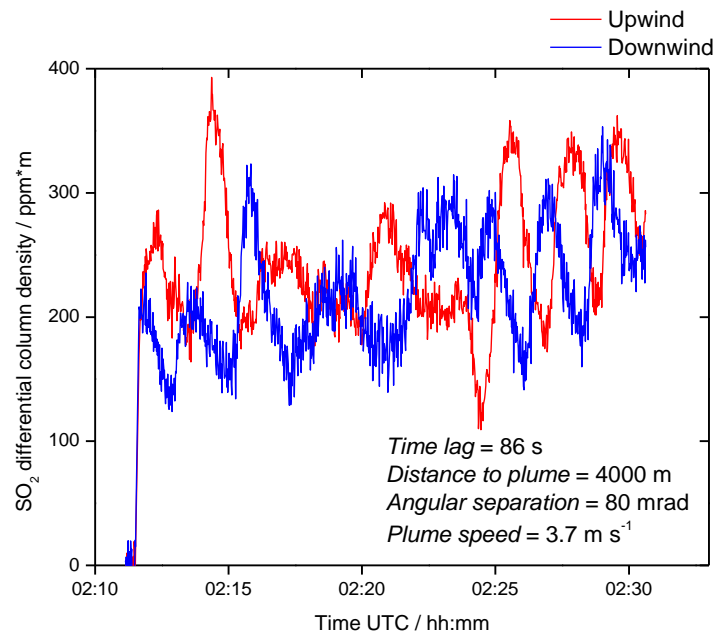


Figure 9. The plume speed is measured by placing the instrument under the centre of the plume with one spectrometer looking further upwind than the other (Johansson et al., 2009). The plot shows a measurement at Karymsky volcano (Kamchatka) on 19 July 2012. The plume was at a distance of about 4000 m, the angular separation of the two lines of sight was 80 mrad and the optimal time lag in the two series was 86 s. The retrieved plume speed was 3.7 m s^{-1}

The calculation of the flux across a surface by scanning DOAS involves a series of steps on each scan:

1. A "clear background" or "sky" spectrum is measured, typically at zenith scanning position. All spectra in the same scan are divided by this spectrum to derive the differential column densities. If the target species is present in the sky spectrum, an offset level is calculated from the measurements with lower (ideally null) gas column densities. Alternatively, a sky spectrum can be modeled or adapted from a measurement with the same or other instrument.
2. A "dark-offset" spectrum is measured, typically by pointing the scanner to the nadir position, which is shielded from incoming radiation. This spectrum is subtracted from each other spectrum in the same scan to give an approximate correction of dark current and electronic offset. Alternatively, the dark-offset spectrum can be modeled from independent measurements of dark current (no illumination at high exposure time, low number of co-additions) and electronic offset (no illumination at low exposure time, high number of co-additions), properly scaled to the exposure time and number of co-added spectra of each measurement.

3. A number of “scan” spectra are measured from horizon to horizon across a flat or conical surface intercepting the volcanic plume. The exposure time and number of co-averaged spectra are usually optimized for having high intensity at the spectral region of interest.
4. Dark current/offset correction is applied on each spectrum. Slant gas column densities are retrieved by the DOAS method, incorporating reference cross sections of possible absorbents convoluted to the resolution of the spectrometer. Shift-squeeze of the spectral elements is usually necessary, which can be implemented by correlating the Fraunhofer structures in the measured spectra with those of a solar spectrum or by free fitting with the sky spectrum.
5. A background correction is applied to the slant column densities. Vertical column densities are calculated from computation of respective air-mass-factors for each slant column density measurement.
6. Cross-section integration is performed based on the angular information and estimation or calculation of the plume height by triangulation of measurements from different locations.
7. The emission rate is estimated by multiplying the integral of column densities with the normal component of transport velocity. All in all, the mass flow rate of SO₂ φ_{SO_2} is calculated according to the formula:

$$\varphi_{SO_2} = c_{\perp} h \sum_{\alpha=-90}^{\alpha=90} [\langle VCD_{\alpha} \rangle \Delta \tan(\alpha)] \quad (39)$$

Where c_{\perp} is the normal component of plume velocity, h the altitude of the plume centre-of-mass relative to the station, $\langle VCD_{\alpha} \rangle$ the average vertical column density between two consecutive measurements, $\Delta \tan(\alpha)$ the angular segment between two consecutive measurements, and α is the scan angle. More details on the geometric calculation of the airmass factor, projection of the normal plume speed component, etc. can be found in Johansson (2009) or Paper II.

2.2.3. Uncertainty related to Scanning DOAS measurements

Estimating the source strength of SO₂ from volcanoes based on measurements of the plume strength involves a series of assumptions. The total uncertainty includes model, parameters and measurement uncertainty. In Paper II, two methods are presented to estimate this uncertainty: an analytical model based on the law of propagation of uncertainty of the Guide for the expression of Uncertainty in Measurements –GUM- (JCGM, 2008.); and a numerical Monte-Carlo estimation. In the former, the measurement equation (39) is propagated in quadrature (assuming independence of terms and neglecting high-order derivatives). In the latter, the uncertainties of the input variables are expressed as probability distribution functions from which random sampling is performed to arrive to an ensemble probability distribution function for the output mass flow rate. Figure 10 below shows an example of this approach for the calculation of uncertainty.

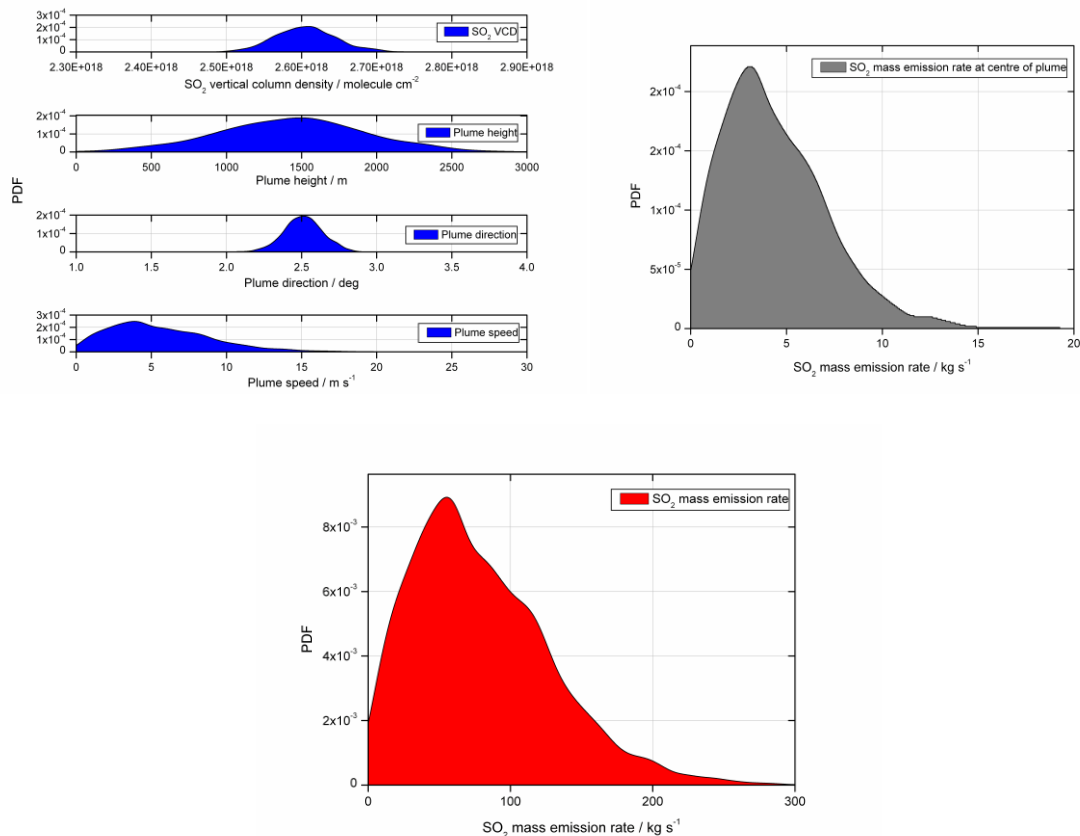


Figure 10. Example of the analysis of uncertainty for one measurement of the mass flow rate of SO₂ on Popocatepetl volcano. The upper left plot shows the probability distribution functions (pdf) of the input variables for one scanning position of the measurement, the upper right plot shows the resulting pdf for the segment of the plume corresponding to that scanning position. The lower plot shows the resulting pdf for the total scan. The method shows that even if the input variables have symmetric distributions, the output may have a skewed pdf. The measurement is represented by the most probable value and the confidence intervals of the resulting pdf (cf. Paper II)

2.3. NOVAC

NOVAC, the Network for Observation of Volcanic and Atmospheric Change, was initiated in 2005 as a 5-years-long project financed by the European Union (Galle et al., 2010). Its main purpose was to implement a global network for the study of volcanic atmospheric plumes and related geophysical phenomena by using the scanning-DOAS instrument. Up to 2014, about 70 instruments have been installed at 32 volcanoes in Central and South America, Italy, Democratic Republic of Congo, Reunion, Iceland, and Philippines, and efforts are being done to expand the network to other active volcanic zones. NOVAC has been a pioneer initiative in the community of volcanologists, involving research institutes and volcanological observatories in more than 20 countries. A map with location of the volcanoes in the network and participating institutions is shown in Figure 11.

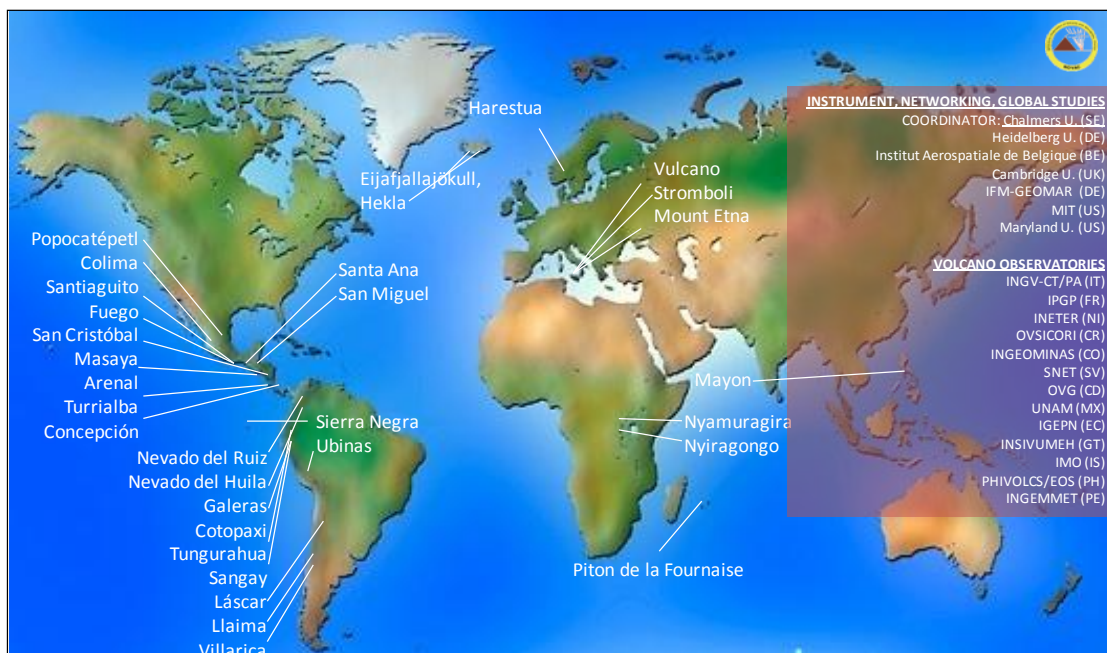


Figure 11. Map of the volcanoes and partner institutions in the NOVAC collaboration

Paper I describes the network and Paper III reports the compilation of results from measurements on 16 volcanoes of NOVAC during 2007-2016. Paper IV presents a methodology to derive BrO column densities from the measurements in NOVAC.

2.4. FTIR

Fourier Transform Infra-Red spectrometry is a well-known analytical method for characterization of chemical compounds. It has been developed for field operations and used on a variety of platforms (ground, ships, balloons, aircraft, and spacecraft). Its importance in Earth's remote sensing lies on the number of advantages that FTIR has with respect to dispersive techniques, such as a higher étendue ("Jacquinot advantage"), S/N , resolution, or wavelength stability.

FTIR is a multiplex technique, which means that several spectral elements are sensed simultaneously by the same detector. This property, referred to as the " Fellgett advantage", is achieved by interferometry: the measurement of an interference pattern of multiple radiation beams. The simplest and most common setup consists of the separation and posterior interference of two beams, as devised originally by A. Michelson for the accurate measurement of lengths in the end of the 1880s (famously used for the "Michelson-Morley" experiment of null absolute motion of Earth respect to the "ether"). Although the principle of interferometry can be applied to radiation of any wavelength, the technique has historically been developed mostly for infrared and longer wavelengths, where abundant information exists on molecular transitions and required materials and detectors are available. In the Michelson configuration, which is the simplest but not always the most technically stable configuration, an incident beam is divided in two approximately equal beams by a beam-

splitter/compensator and guided to travel two perpendicular, mirror-folded, counter-propagating paths to be then recombined (interfered) at the beamsplitter, deviating again half of the radiation to a detector and the other half to the entrance aperture. By controlling the difference in pathlength of the two beams, it is possible to relate the interference pattern to this difference, or equivalently, to time. This relation is called the interferogram (amplitude vs. path difference), from which the spectrum (amplitude vs. frequency ν or wavenumber $\tilde{\nu} = 1/\lambda$) is obtained via a mathematical operation known as the Fourier transformation, hence the name of this technique.

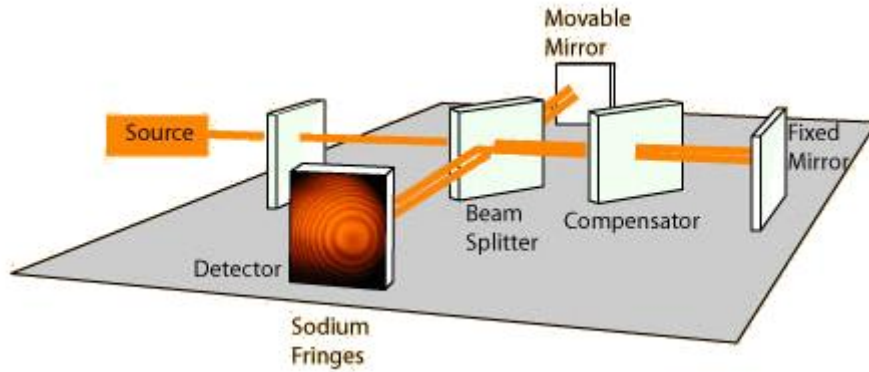


Figure 12. Schematics of a FTS in the Michelson configuration. Radiation from the source is filtered and divided in two beams at the beam-splitter. One of the beams is reflected in a fixed mirror (through a compensator to equate the paths through the substrate of the beamsplitter) and the other in a movable mirror. The beams are recombined at the beamsplitter, wherefrom half of the interfered radiation is detected and half is redirected to the source (Image courtesy of Rod Nave, HyperPhysics project: <http://hyperphysics.phy-astr.gsu.edu/hbase/hph.html>)

Expressed in mathematical form, the intensity as a function of path difference $I(x)$ formed from the interference of beams with monochromatic intensity as a function of wavenumber $F(\tilde{\nu})$ from a broad-band source is given by:

$$I(x) = \int_0^{\infty} F(\tilde{\nu}) [1 + \cos(2\pi\tilde{\nu}x)] d\tilde{\nu} = \int_0^{\infty} F(\tilde{\nu}) d\tilde{\nu} + \int_0^{\infty} F(\tilde{\nu}) \cos(2\pi\tilde{\nu}x) d\tilde{\nu} \quad (40)$$

Where the first term corresponds to the total energy incident on the system $\int_{-\infty}^{\infty} F(\tilde{\nu}) d\tilde{\nu} = C$ and the second term is the interferogram. The spectrum is obtained from the Fourier transformation:

$$F(\tilde{\nu}) = \int_{-\infty}^{\infty} [I(x) - C] B(x) \cos(2\pi\tilde{\nu}x) dx \quad (41)$$

In which the boxcar function $B(x)$ has been introduced to account for the limited pathlength L of the system, while preserving the infinite limits of integration of the transformation. The inclusion of the boxcar function is equivalent to a convolution of the spectrum with a "sinc" function: $F(\tilde{\nu}) \otimes \sin(2\pi\tilde{\nu}L)/2\pi\tilde{\nu}L$, which represents the nominal ILS of the FTIR with a resolution (FWHM) given by $\delta\tilde{\nu}/\tilde{\nu} = 0.6034/L$ in cm^{-1} . Since this function presents unwanted periodic wings, it is common to include an "apodization" function such as triangular, rectangular, Norton-Beer, Mertz, etc., at the cost of degrading the spectral

resolution. The ILS of a FTIR is wavelength invariant, a property known as the “Connes advantage”. Precision in wavelength marking is also an asset of FTIR, which uses a very stable laser beam following the same optical path of the measurement to control de sampling. For instance, the FTIR employed in our measurements has a precision of 0.04 cm^{-1} .

Limitations that degrade the resolution or produce spectral shifts include the effect of beam divergence, non-ideal modulation efficiency of the beamsplitter, pointing errors, and image motion (turbulence, jittering). The interested reader is referred to the extensive literature about the technique for more details (Beer, 1992; Davis et al., 2001; Griffiths and De Haseth, 2007).

2.4.1. FTIR measurements of volcanic gas molar ratios

The use of FTIR for volcanic gas studies in the field dates back to the 1990s. The first measurements were reported by Japanese researchers (Mori and Notsu, 1997; Notsu et al., 1993), who measured several species by employing the thermal emission from the hot volcanic rocks as the source for remote absorption measurements. Solar direct absorption and plume thermal emission measurements have also been reported (Francis et al., 1998; Love et al., 1998), as well as measurements with a lava fountain (Allard et al., 2005), lava lake (Sawyer et al., 2008), the moon (Burton et al., 2001), or explosively ejected material as sources of radiation (La Spina et al., 2013; Oppenheimer et al., 2006). Scanning image construction of the plume (Stremme et al., 2011) and active open-path FTIR measurements (Duffell et al., 2003; Conde et al., 2014) have also been carried out in volcanic environments. The range of trace gas species measured with FTIR is large, covering all the most abundant components (H_2O , CO_2 , SO_2 , HCl , HF , CO , COS , SiF_4), particularly when proximal (e.g., at the crater rim) observations and low temperature (e.g., terrestrial bodies, lamps) sources can be used. The following paragraphs describe the procedure of FTIR measurements of volcanic gases:

1. Radiation transport in the infrared spectral region is complicated due to the fact that not only absorption of radiation from the source (sun/moon/lamp/rocks/plume) by the gas plume occurs, but also thermal radiation is emitted. Refraction, scattering and reflection are, on the other hand, usually negligible in this region. The information content of the spectrum makes possible in some cases to retrieve temperature/pressure conditions in the observed system as well as absolute concentrations of the absorbing species; however, this requires proper radiometric calibration. The situation is simpler if only ratios of column amounts/concentrations are needed, as explained below.
2. Infrared radiation is collected by a pointing/gathering radiation system, analyzed by the interferometer and detected by either a photovoltaic or photoconductive element or array of detectors. In direct solar configurations, the sun position has to be tracked with precision, especially for high resolution ($<10^{-2} \text{ cm}^{-1}$) measurements, because background source variations and pointing cause undesired shift or resolution distortions. The most common detectors in the 1 to 12 μm wavelength interval are photovoltaic InSb and HgCdTe (or MCT) detectors, which operate at low temperatures, requiring contact with liquid N_2 ($\sim 77 \text{ K}$) or another cooling mechanism. The signal is then amplified, digitalized and recorded for further analysis.

3. Analysis consists first on the transformation from interferogram to spectrum (via a discrete Fourier transformation, apodization, frequency-shift corrections). The spectral inversion then consists on reconstructing the spectrum from a forward model, as for example implemented by D. Griffith for the Multi-Layer-Atmospheric-Transmission (MALT) model (Griffith, 1996) used in this thesis. This retrieval procedure consists on simulating the measured transmission by including spectral information (temperature/pressure dependence parameters for the line strengths of the molecules absorbing in the spectral interval of interest), pressure-temperature-composition of different atmospheric layers depending on the measurement configuration, and instrumental parameters (ILS). A non-linear Levenberg-Marquardt or another iterative fitting algorithm is performed to retrieve the variables of interest, particularly the gas column amounts of the absorbing molecules included in the model. Since the optical path is assumed to be the same for the plume molecules, the ratio of concentrations between different species can be obtained from a single spectrum.

2.4.2. Solar FTIR

Solar FTIR consists in measuring the direct solar radiation to analyze the composition of the intervening atmosphere. With the aim of developing a Solar FTIR system for automatic volcanic plume measurements it was necessary to design and build a solar-tracking apparatus, which transfers the (moving) direct solar beam into the (stationary) interferometer. It was decided to build a simple stationary tracker based on two motorized rotating mirrors with the possibility of equatorial or horizontal setups¹⁹. Previous work in this line has been done by the Chalmers Optical Remote Sensing group for stationary high-resolution FTIR measurements of atmospheric composition (Galle et al., 1999) and for mobile low-resolution FTIR measurements of industrial emissions by the Solar Occultation Flux (SOF) method (Kihlman, 2005), as well as for direct-sun DOAS measurements within the NOVAC collaboration (Sommer, 2008).

The solar tracker is mounted on a horizontal platform oriented towards North. The solar tracking algorithm consists on first reading the time and position from a GPS sensor, then calculating the corresponding coordinates of the sun and moving the mirrors accordingly (Merlaud et al., 2012). Although the theoretical precision of the solar position calculation and of the stepper motors is high (0.001 deg, 0.004 deg respectively), misalignments are unavoidable, requiring an active fine-tuning of the signal based on the actual intensity at zero-path-difference (ZPD) of the interfering beams (centre of the interferogram). Spectral shifts caused by non-normal incidence of the beam can also be corrected for by adjusting the position of known features in the spectrum. The fine-tuning is done on a reduced interval of the spectrum and at low resolution (8 cm⁻¹) for speed. If the fine-tuning procedure fails at recognizing a high enough intensity due to, for instance, the presence of clouds, it proceeds to acquire interferograms based only on the calculated pointing direction. The acquisition of measurement interferograms is made at a highest possible resolution of the FTIR (0.5 cm⁻¹). Photography of the solar tracker developed for volcanic plume measurements is presented in Figure 13.

¹⁹ An equatorial setup is particularly beneficial to preserve the orthogonality of the coordinates of solar motion at high solar zenith angles (close to noontime at low latitudes). Horizontal setups are prompt to such singularities.

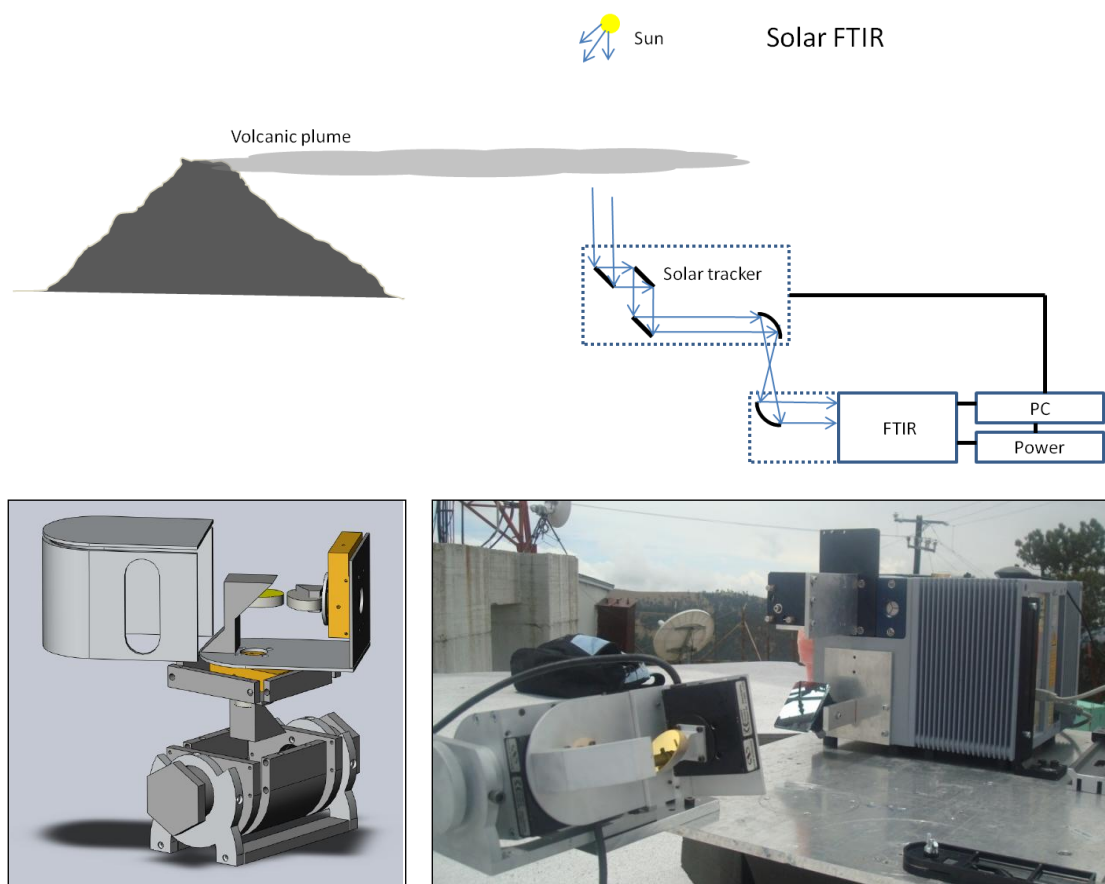


Figure 13. Above: Schematics of the principle of Solar-FTIR measurements. Below: Model of the solar tracker and photography of the system for measurements of volcanic plumes

Solar –FTIR measurements were done in field campaigns at the volcanoes Popocatépetl (Mexico), Tungurahua (Ecuador) and Nyiragongo (D.R. Congo). Some results are presented in the next chapter.

2.4.3. Open-Path FTIR

In the open-path (OP) FTIR configuration, an atmospheric path of known distance is observed between an artificial or natural source and the optics-FTIR system. OP-FTIR measurements of volcanic gases can be made in passive mode, using a hot body in the background of the plume, or in active mode, when an IR lamp is used as source. Measurements in emission mode are also possible, but were not made during the work reported in this thesis.

The telescope used for this measurements was a simple Newtonian with a primary mirror of 30 cm diameter and focal length de 80 cm (f/2.7), and a flat secondary mirror, matching the entrance aperture of the interferometer. Schematic of the setup is shown in Figure 14.

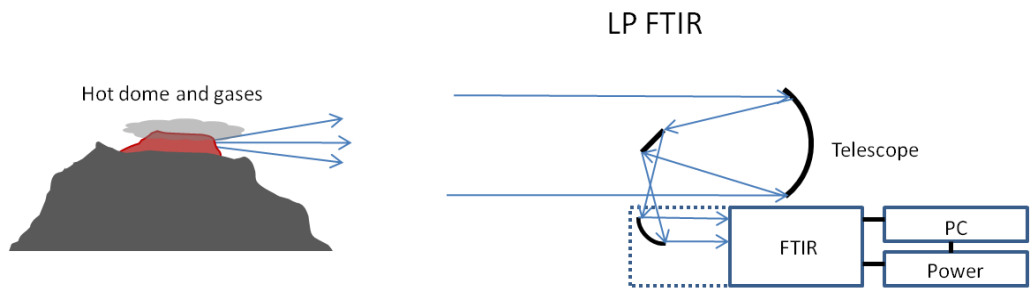


Figure 2. Schematics of the passive open-path FTIR system developed for volcanic gas measurements

OP-FTIR measurements were done in a field-campaign at Fuego de Colima volcano (Mexico). The results are presented in the next chapter. More details about the Scanning-DOAS and FTIR techniques are given in Table 3.

Table 3. Technical details of the Scanning-DOAS and FTIR techniques

Characteristic	Scanning-DOAS	Solar/OP FTIR
Spectral region (for SO ₂ , HCl)	278– 425 (310–325) nm	1850–4000 (2470–2535, 2810–2870) cm ⁻¹
Spectral resolution	0.6 nm	0.5 cm ⁻¹ (Maximum path difference of 1.8 cm)
Temporal resolution	Approx. 5 min (per flux)	Approx. 10 s (per spectrum)
Field of view	15 mrad	30 mrad (adjusted in fitting)
Source of radiation	Diffuse solar radiation	Direct solar radiation or hot lava dome
Transfer optics	Flat/conical scanning refractor, VIS-filter, quartz bundle optical fiber	Stationary solar tracker, flat, Au-coated mirrors, Ge/Si filter
Spectral analyzer	Crossed Czerny-Turner grating spectrometer	“SolidRock” (pendulum) interferometer with ZnSe covered KBr beamsplitter
Detector	2049-element linear Si CCD array, with UV-fluorescent film	InSb, cooled by thermo-electrical system or liquid N ₂
Typical acquisition parameters	15 co-added spectra, optimal integration time (typically 100-1000 ms)	16 co-added scans
Species included in fitting	SO ₂ , O ₃ , modeled Ring spectrum, 5 th order polynomial	SO ₂ , HCl, CH ₄ , N ₂ O, H ₂ O, 2 nd order polynomial
DOAS and FTIR implementation	Dark/offset subtraction, ratio by sky spectrum, HP-filter, NL-LS-fit	Multi-layer model (HITRAN), NL-LS-fit (MALT)
Wavelength shift correction	Fit to Fraunhofer solar spectrum	Fit to modeled spectrum
Size	Approx. 20 cm ³	Approx. 30 cm ³
Geometrical variables	Plume height and velocity by correlation or models	NA
Power consumption	5 W	40 W
Typical uncertainty	Approx. 30% (per flux)	Approx. 5% (per spectrum)

3. Results

"Nature uses only the longest threads to weave her patterns, so each small piece of her fabric reveals the organization of the entire tapestry."

— Richard Feynman ²⁰

3.1. Observations with DOAS on several volcanoes

3.1.1. Karymsky

Karymsky (54.05° N, 159.45° E, 1536 m) is a basaltic/andesite stratovolcano in the eastern volcanic zone of Kamchatka. About 11000 people live within 100 km from the volcano (Smithsonian Institution, <http://www.volcano.si.edu/>). We conducted ground-based remote measurements of volcanic plumes at Kamchatka during 5, 6 and 10-14 September 2011 by using scanning and mobile DOAS systems. The Rapid-Deployment System (RDS) is a scanning DOAS instrument similar to the Mark I system of the NOVAC project, but forming a single unit easy to transport and install in the field (Conde, 2011). It includes a back-pack/box containing the basic components: electronic box, spectrometer, timer, power regulator, and 12V battery; and the corresponding connectors for: tube-protected optical fiber, tripod-supported scanner, GPS antenna, foldable solar panel, and communication cables. Figure 15 shows photographs of the two instruments deployed at Karymsky volcano.



Figure 15. Left: Photograph of the Rapid-Deployment-System. Right: Photograph of the Mobile-DOAS instrument. Both were used for the measurements at Kamchatka (Photos by B. Galle)

To correct for potential shifts in the pixel-wavelength relation of the spectrometers which occur mainly due to thermal stresses, the analysis of data included a calibration scheme that uses the known positions (wavelengths) of Fraunhofer structures in the solar spectrum to

²⁰ "The Character of Physical Law", 1964, p. 34

determine the optimal shift and applies it to all the spectra of each scan. Because the RDS incorporate a temperature sensor inside the box, it was possible to characterize the thermal dependence of this shift for the spectrometers. An example of such analysis is presented in Figure 16.

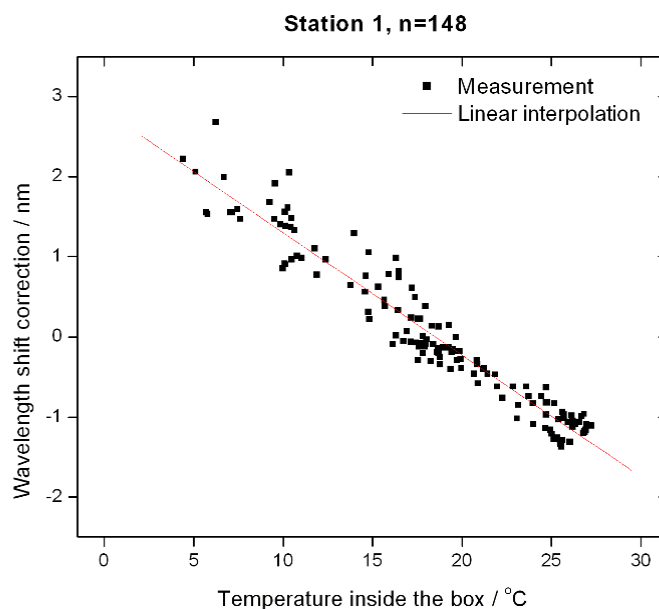


Figure 16. Linear dependence on temperature inside the box of the optimal shift for the pixel-wavelength mapping of the spectrometer D2J2356 (Shift = $2.82 - 0.152T$)

In cooperation with the Institute of Volcanology and Seismology of the Far Eastern Division of the Russian Academy of Sciences (IVS FED RAS), our group conducted a campaign of remote sensing measurements of the SO₂ gas emissions of Karymsky volcano during 10-14 September 2011. Karymsky is probably the most active volcano of Kamchatka and known for being the locus of persistent low-to-moderate explosive activity since its reactivation in 1996. Geophysical studies in the past have identified the main video-seismo-acoustic (Johnson and Lees, 1998; Johnson and Lees, 2000; Ozerov et al., 2001) and geochemical (Fischer et al., 2002) features of the explosions at Karymsky. The mechanisms responsible for these explosions seem to be related to the formation of temporal plugs in the vent which create a pressure buildup until a threshold is reached triggering an explosion. The emissions are occasionally rich in ash and lithics and continuous degassing usually followed after the explosive opening of the vent.

To better keep tracking of the gas emissions of Karymsky, we made a temporal installation of 2 scanning DOAS systems in flat and conical configurations oriented in order to intercept the plume as much perpendicularly as possible. The stations were visited every day to download the saved data, clean the ash deposition, and revise the scanning directions and performance. No instrumental problems were detected during the measurement period. Additionally, mobile-DOAS measurements with 2 different systems were conducted from the Observatory of the RAS (located close to St. B) in different measurement modes. The positions and orientations of the RDSs are illustrated in Figure 17.

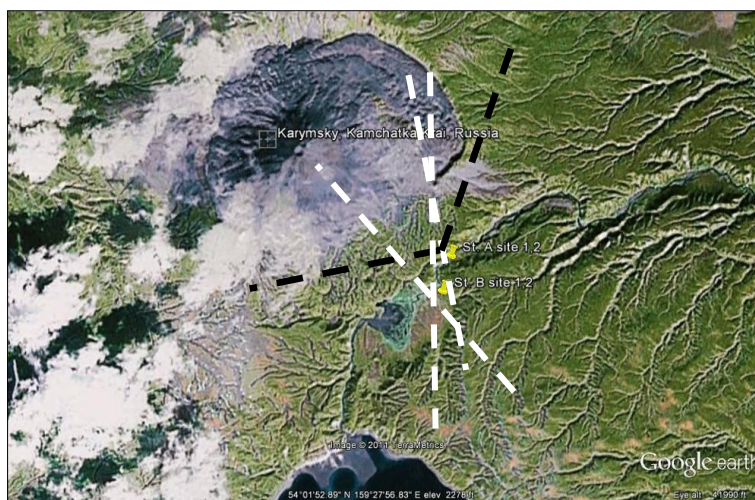


Figure 17. Image of Karymsky volcano showing the location (yellow marker) of the measurement stations and scanning directions (white dashed lines for flat and black dashed lines for conical scanners) (Base image from Google Earth)

The RDS collected a total of 432 scans during almost 4 days of operation. The close proximity to the plume (typically < 2 km) made possible to enclose the plume cross section most of the time. As an example of a tandem observation of the plume by the 2 RDSs, Figure 18 shows scans taken on the 12th September 2011.

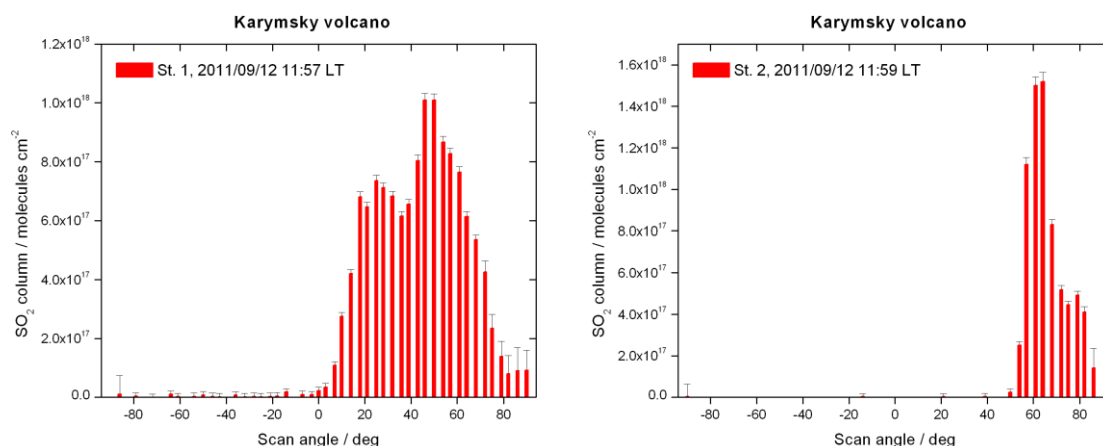


Figure 18. Examples of scans obtained from stationary measurements at Karymsky volcano. Station A (left) was closer to the plume than Station B (right) and therefore had a less skewed coverage of it. The combination of the 2 observations allows estimation of the plume height and direction

The results of individual scan measurements are presented in graphical form in Figure 19, and in numerical form in Table 3. The data points do not show uncertainty estimates, which are expected to be >30% and controlled by the plume speed uncertainty. A method to estimate the wind speed based on a special configuration of mobile-DOAS measurements is presented below.

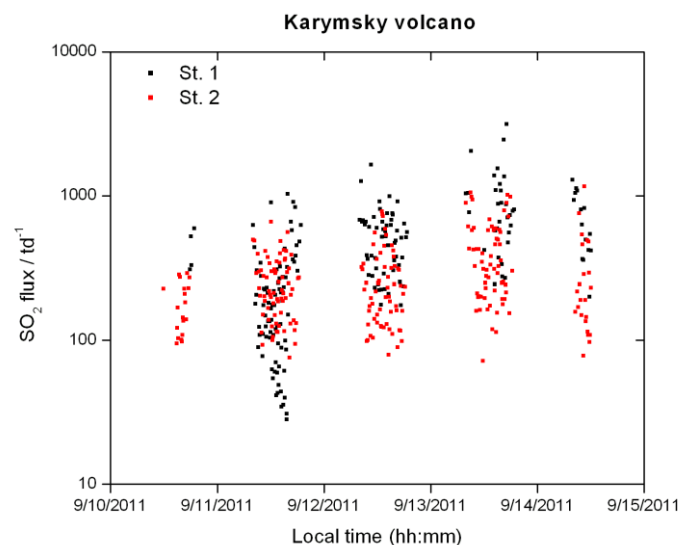


Figure 19. Time series of SO₂ mass flow rates for Karymsky volcano (2011/09/10-14) obtained from measurements with 2 Rapid-Deployment-Scanning DOAS systems. A standard value of wind speed of 6 ms⁻¹ was used in the calculations

Table 3. Statistics of the measurements of SO₂ gas emissions of Karymsky volcano

	Number of measurements	Plume direction / deg	Plume speed / ms ⁻¹	Plume height / m a.s.l.	SO ₂ flux / td ⁻¹		
					Range	Average	Std. Dev.
Station A	189	328 ± 35	6	1375 ± 340 (33)	28 – 3145	480	429
Station B	243	333 ± 21	6	1375 ± 340 (33)	72 -1159	295	202
Combined	432	331 ± 28	6	1375 ± 340 (33)	28 – 3145	376	334

The measurement configuration of the scanning systems made possible to estimate the wind direction and height of the plume in 33 occasions. The results, presented in Table 4 and Figure 20, indicate that the plume transport was very stable and that the plume height (at the centre of mass) was slightly higher than the summit altitude. In terms of daily variability, the emission rate also was remarkably stable, with a short-term variability associated with shallow processes (sealing-explosion rates) but no important deviations from the mean daily emission rate.

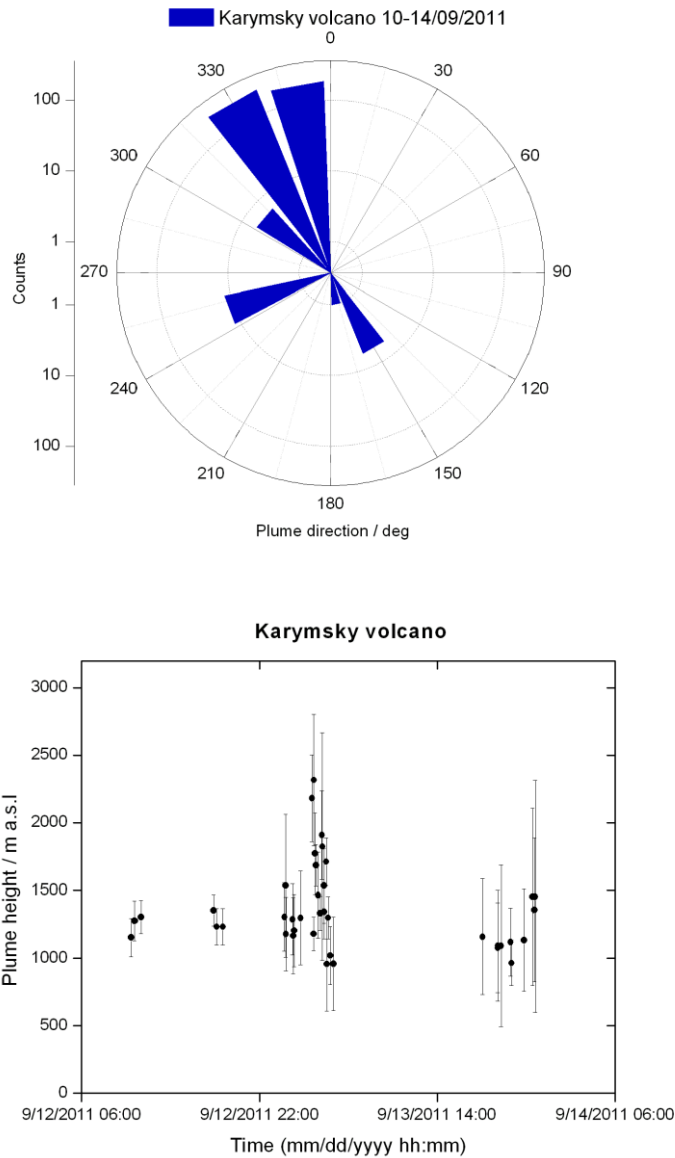


Figure 20. Above: Wind-rose showing the distribution of plume directions (upwind) as measured from triangulation of the scanning systems. Below: Plume heights derived from the same measurements

The main source of uncertainty in our measurements is the estimate of plume speed. For the measurements reported here, we have used values reported from external sources (visual or UV-camera observations, weather forecasts) and it is desirable to have concurrent measurements of this parameter. The dual-beam method was not performed due to logistical constraints to find a location below the centerline of the plume to do the measurements. For the case of Karymsky, visual estimates suggested that the plume transport speed was not very high at the section of the plume intercepted by the scanners. A report from NOAA (<http://ready.arl.noaa.gov/READYamet.php>); however, indicates wind-speed values at the summit of Karymsky that were unexpectedly high. We decided not to interpolate these values to report our flux measurements and instead used a constant value

of 6 ms^{-1} , which was a typical value obtained from Large-Field of View Mobile-DOAS measurements.

The particular activity of frequent explosive emissions observed at Karymsky, led us to experiment a configuration of stationary measurements with the mobile-DOAS instrument in which we dispensed with the use of the telescope and point instead to the plume with the large field of view ($\sim 150 \text{ mrad}$) of the optical fiber. In this way, a considerable portion of the plume is observed at once in the field of view of the instrument and acquisition can be done at a much higher frequency ($\sim 1 \text{ Hz}$) than with a scanning method. The implementation of this methodology to volcanic studies is not new (Boichu et al., 2010; McGonigle et al., 2009), and Karymsky volcano was an ideal scenario to implement it.

We performed Large-Field of View mini-DOAS (LFOV-miniDOAS) measurements at Karymsky during several hour-long periods on the 12, 13 and 14 September 2011 from the observatory. An extract of one of these periods is shown in Figure 21, in which the blue line represents the intensity of UV light in the region of SO_2 absorption and the red line is the real-time column measurement. It is evident a negative correlation of the 2 time-series, which shows the promise of the method to do positive detection of volcanic plumes.

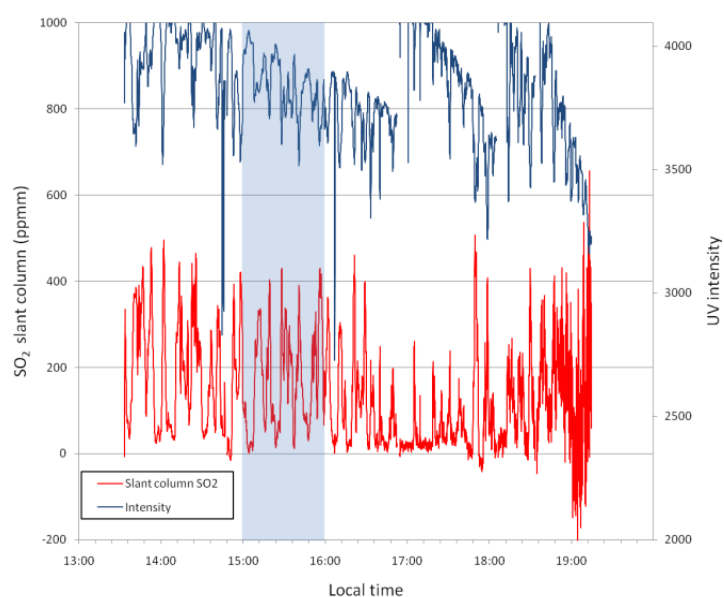


Figure 21. Time series of LFOV mini-DOAS measurements at Karymsky on 2011-09-12. The upper blue line represents UV intensity and the lower red line SO_2 column amounts. The shaded area corresponds to an interval used for estimation of the wind speed

A potential drawback of this method is the difficulty to determine how representative of the instantaneous emission is the snapshot of the plume observed by the instrument. Another limitation is the fact that heterogeneities in gas concentration observed in the field of view might cause an underestimation that can be significant for optically thick regions of the plume. On the other hand, the LFOV mini-DOAS method provides a reliable way to determine the plume transport speed for the type of activity of Karymsky. By tracking the time of occurrence of explosive events (by visual observation or acoustic signals), and

controlling the geometry of the observation (distance to the plume and azimuth of observation respect to the vent direction), it is possible to quantify the time it takes for a given parcel of gas emitted in the explosion to be detected by the instrument. We mark the times of occurrence of explosions for a given period of observation in Figure 22 and observe the increase in the corresponding gas measurement after a certain period. In practice, we assume that the instrument detects the explosion before or at the moment of a relative maximum in column amount, which is probably the time when the bulk of the emission of each event is covering the field of view of the instrument.

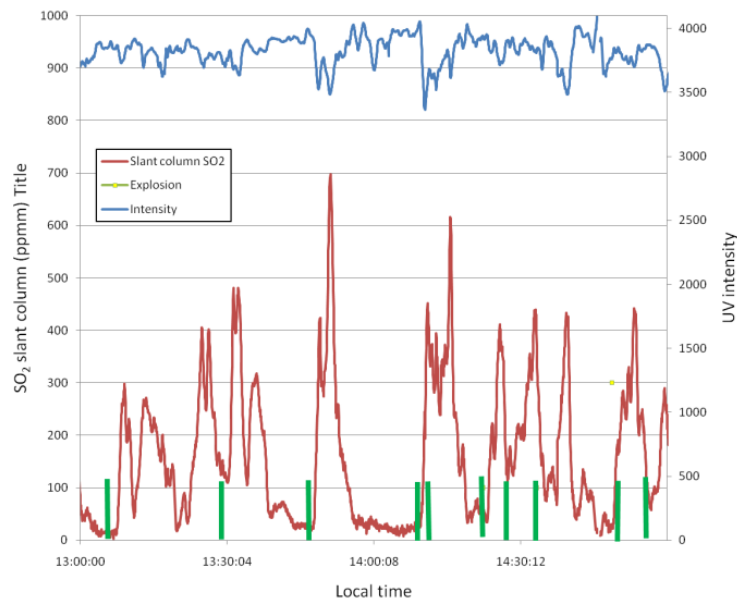


Figure 22. LFOV measurement on 2011-09-13, showing the times (green marks) when explosions occurred at Karymsky volcano

A concrete example of this method to estimate the plume speed is presented in Figure 23. The upper figure gives details for an individual measurement (in this case the time shift between the explosion and the beginning of the increase in the column series). The center figure shows the application of this method (with shifts until the position of the peak columns) to a longer data series, and the lower figure presents the results.

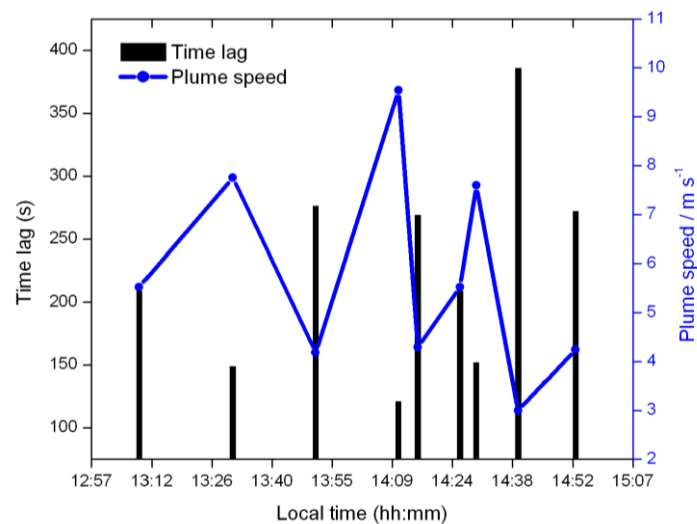
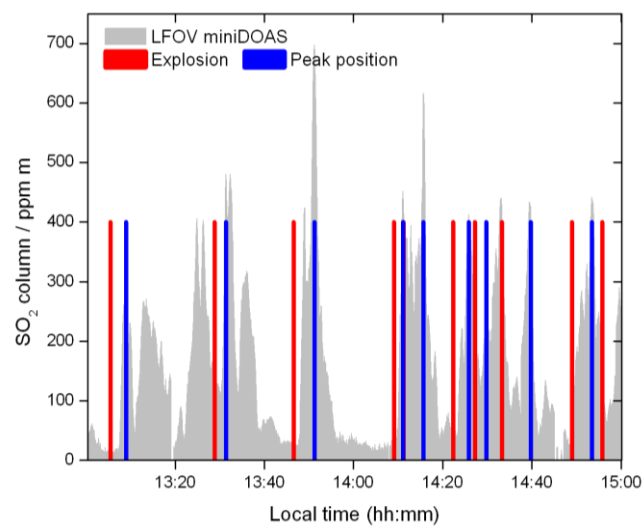
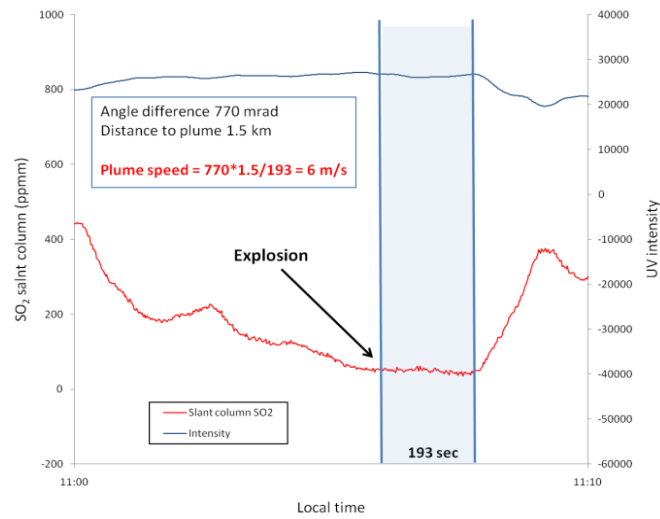


Figure 23. Application of the plume speed estimation method based on LFOV mini-DOAS measurements. Above: Example of a single calculation showing positions of the time lag and additional information used for the wind speed measurement. Middle: Extension of the method to a larger dataset. Below: Results of the calculations for the data set presented in the center, a mean value of $5.74 \pm 2.13 \text{ ms}^{-1}$ ($\pm 1\sigma$) was obtained

The time series of SO₂ emission rate measurements at Karymsky reveal two main degassing patterns:

- During 10-13 September, the volcano produced small Strombolian eruptions at a typical rate of 3-20 explosions per hour. These were characterized by small-to-moderate ash contents, variable audible intensity of explosions and accompanying rumbling. At night, it was possible to distinguish incandescence associated with some of the explosions with the naked eye. The gas emission dropped to an undetectable level after the degassing events.
- On 14 September, the volcano produced bigger Vulcanian-type eruptions at a typical rate of 1 per hour. These were characterized by variable amounts of ash, strong audible signals and were followed by open degassing with variable amounts of ash during each event. The gas emission did not cease between events.

Such activity is typical of Karymsky since its reactivation in 1996 and the details of the shallow geophysical signals have been reported before (Fischer et al., 2002; Johnson and Lees, 1998). Our measurements constitute the first of its type during the last decade and confirm the permanency of Karymsky's activity without major changes.

3.1.2. Nyiragongo

Nyiragongo (1.52° S, 29.25° E, 3470 m) is a very active volcano located in eastern Congo, close to the border with Rwanda. The city of Goma, with about 1 million inhabitants, is located less than 20 km from the volcano, and nearly 9 million people live within 100 km from the volcano (Smithsonian Institution, <http://www.volcano.si.edu/>). The area is politically unstable in recent times; with hundreds of thousands of refugees from a civil war in the area and in nearby Rwanda. In 2002 a flank eruption caused rapid lava flows that destroyed about 20% of the city. Besides the high direct threat of the volcano to the population, the volcano is one of the strongest sources of volcanic gases in the world with an SO₂ emission of 5000-50000 t d⁻¹. In addition, high amounts of HCl and HF are abundant in the plume. The population and vegetation downwind the volcano is strongly affected both directly by the toxic gases, and indirectly by acid rain and contaminated drinking water.

To help monitoring Nyiragongo, our group has installed 4 scanning-DOAS instruments since 2004 at distances between 9 and 14 km from the crater in the sites called Rusayo, Sake, Kunene and Buzi (Kunene station was later replaced by an instrument at Kingi). Due to difficulties to maintaining the stations, some gaps in the time series exist. About 70% of the valid measurements were done by the Rusayo station and most of the rest by the Sake instrument.

The evaluation of data was done according to the procedure describe above and the most important results are depicted in Figure 24 and listed in Table 4 below (cf. Paper V).

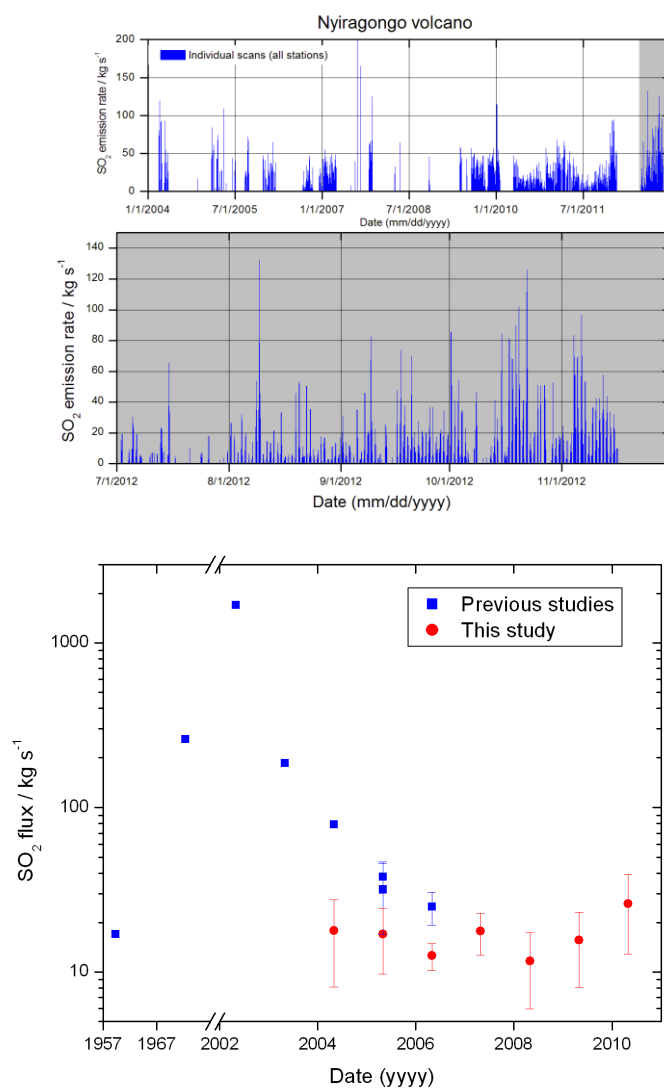


Figure 3. Above: Time series of SO₂ emission rate from Nyiragongo volcano measured with scanning-DOAS during 2004-2012. Below: Annual averages obtained from measurements within NOVAC extending the historical record of degassing monitoring at this volcano (cf. Paper V)

Table 4. Results of NOVAC measurements (2004-2012) at Nyiragongo volcano

	Mean	Std. Dev.	Min.	Max.
SO ₂ emission rate / kg s ⁻¹ (t d ⁻¹)	17.58 (1519)	15.05 (1300)	0.24 (21)	185.12 (15995)
Wind speed / m s ⁻¹	5.43	2.17	0.30	11.30
Wind direction / deg	72.10	21.37	1.00	250.00
Plume height / m a.s.l.	3502.80	209.43	2255.84	5148.43

3.2. Observations with FTIR on several volcanoes

3.2.1. Nyiragongo

Two field campaigns for observations with solar-FTIR were conducted at Nyiragongo volcano on November 2013 and March 2014. The instrument was placed close to Kingi, a small village located about 12 km WNW of the volcano, and solar spectra were obtained with the plume in occultation. Data was evaluated with the MALT model (Griffith, 1996). Excerpt plots from the evaluation results are indicated in Figure 25 below.



Figure 25. Spectral fitting of solar-FTIR measurements at Nyiragongo. The upper plot shows the case for HCl, along with the interfering species CH₄, H₂O and N₂O. The lower plot shows the fitting for SO₂, in the region where also CH₄, H₂O and N₂O absorb. The SO₂/HCl molar ratio out of 37 measurements was in the range 24.3 ± 1.8 (Nov. 2013) and from 826 spectra the molar ratio was 18 ± 1.5 (Mar. 2014)

3.2.2. Popocatépetl

Popocatépetl (19.02° N, 98.62° W, 5426 m) is an active stratovolcano of basaltic to dacitic composition, located in Mexico, where nearly 26 million people live (within 100 km of the volcano) (Smithsonian Institution, <http://www.volcano.si.edu/>). Solar-FTIR measurements were performed during a field campaign in April 2010 from 4 different sites at distances between 10 and 17 km from the crater. These observations were conducted close to noon time, where it is easier to obtain the right geometry with the sun behind the plume. Examples of the spectral fitting based on the MALT model are shown in Figure 26.

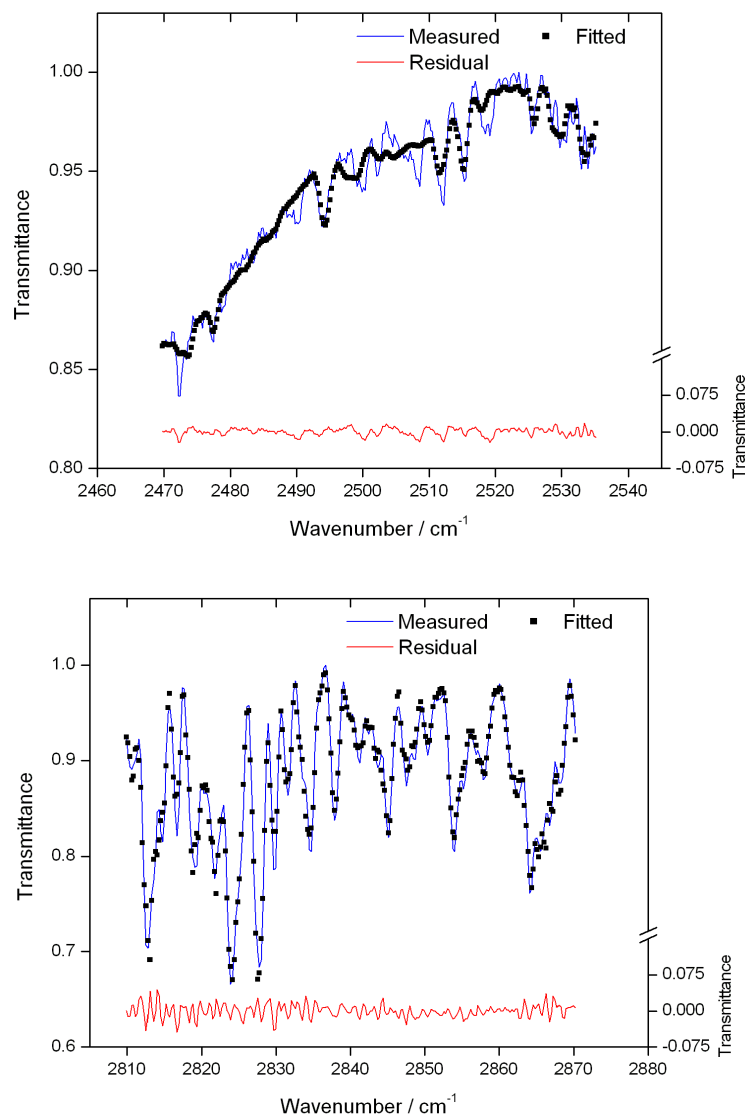


Figure 26. Above: Spectral fit for SO₂ based on the MALT model of a volcanic plume from Popocatépetl (Mexico) measured 17 km downwind the crater on 21 April 2010. Below: Spectral fit for HCl. Other species included in the fit are H₂O, CH₄ and N₂O and a second order polynomial. The SO₂/HCl molar ratio out of 21 measurements was 0.31 ± 0.29

3.2.3. Fuego de Colima

Fuego de Colima (19.51° N, 103.62° W, 3850 m) is a basaltic-to-dacitic stratovolcano located in Mexico. It affects to about 1.5 million people living within 100 km (Smithsonian Institution, <http://www.volcano.si.edu/>). OP-FTIR measurements were conducted in a field campaign at Fuego de Colima volcano in Mexico in February 2011 by B. Galle, V. Conde and Mexican colleagues. The system was deployed at a distance of 5.2 km from the crater dome, at the facilities of the volcanological observatory in Nevado de Colima. The telescope was pointed to the dome, where thermal radiation was intense enough to produce an IR signal above background. Unfortunately, the direction of the plume was most of the time in the opposite side; however, in certain occasions it moved within the field of view of the instrument and volcanic species could be detected (cf. Figure 27).

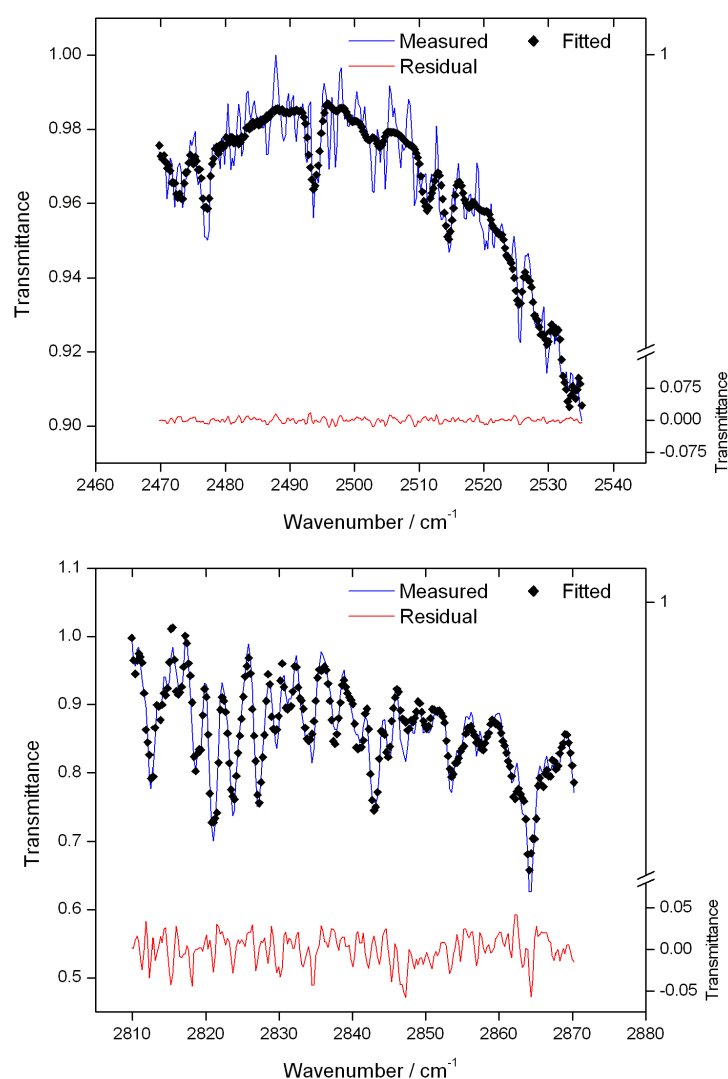


Figure 27. Spectral fit for SO₂ (upper plot) and HCl (lower plot) based on the MALT model of a volcanic plume from Fuego de Colima measured 5.2 km from the crater on 17 February 2011. Other species included in the fit are H₂O, CH₄ and N₂O and a second order polynomial. The SO₂/HCl molar ratio out of 71 measurements was of 16.27 ± 85.65

3.2.4. Tungurahua

Tungurahua (1.47° S, 78.44° W, 5023 m) is a basaltic-andesitic stratovolcano in Ecuador. About 1.6 million people live within <100 km from the volcano (Smithsonian Institution, <http://www.volcano.si.edu/>). Solar-FTIR measurements were done at Tungurahua volcano during July 2012. In this campaign a zenith-looking mobile DOAS with stationary Solar FTIR were combined. The mobile measurements allowed us to identify the position of the plume and to derive the total mass flow rate of SO₂. Based on the location of the plume after the first traverse, the optimal location for solar measurements was selected and the FTIR deployed. At the end, a second return traverse was made to improve the mass flow rate statistics. The combination of the 2 methods allowed us to determine the fluxes of SO₂ and HCl. Results and depiction of the campaign are shown in Figure 28.

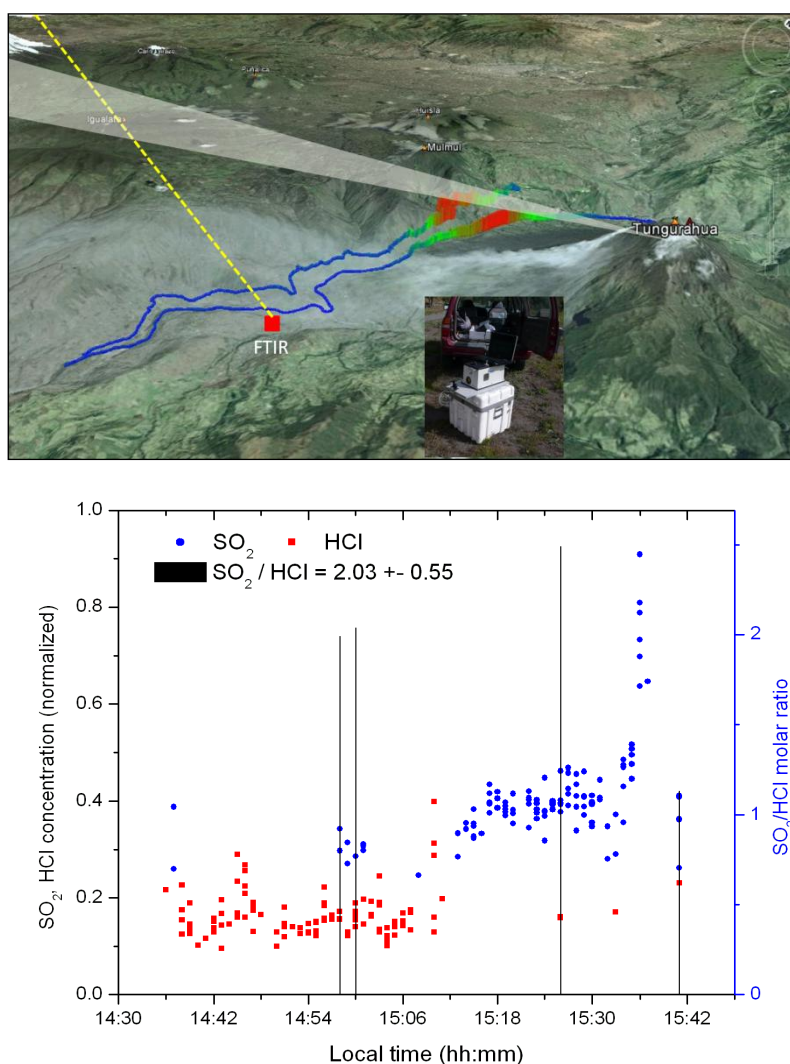


Figure 28. DOAS and FTIR measurements at Tungurahua volcano in July 2012. Above: Map showing the trajectories of the mobile DOAS traverses and bars representing the column amounts of SO₂ when crossing the plume. After the first traverse, the right location for solar FTIR measurements was determined and the observations carried out (base image fr. Google Earth). Below: Time series of the SO₂ and HCl relative molar concentrations and their ratio

3.3. Observations from the network perspective: NOVAC

Paper III is a compilation of measurements on 16 NOVAC volcanoes during 2007-2013. The evaluation was performed with the NOVAC Post-Processing Program (NovacP³) developed by M. Johansson, following the same protocols than for the observatory software. Wind data was mostly provided by analyzed modeled data from the European Center for Medium-Range Weather Forecasts (ECMWF), with a time resolution of 6 h, horizontal resolution of about 16 km and vertical resolution of less than 1 km and interpolated to the time and location of the measurements. The most important statistics, showing the distributions of the measurements for each volcano, are shown in Figure 29.

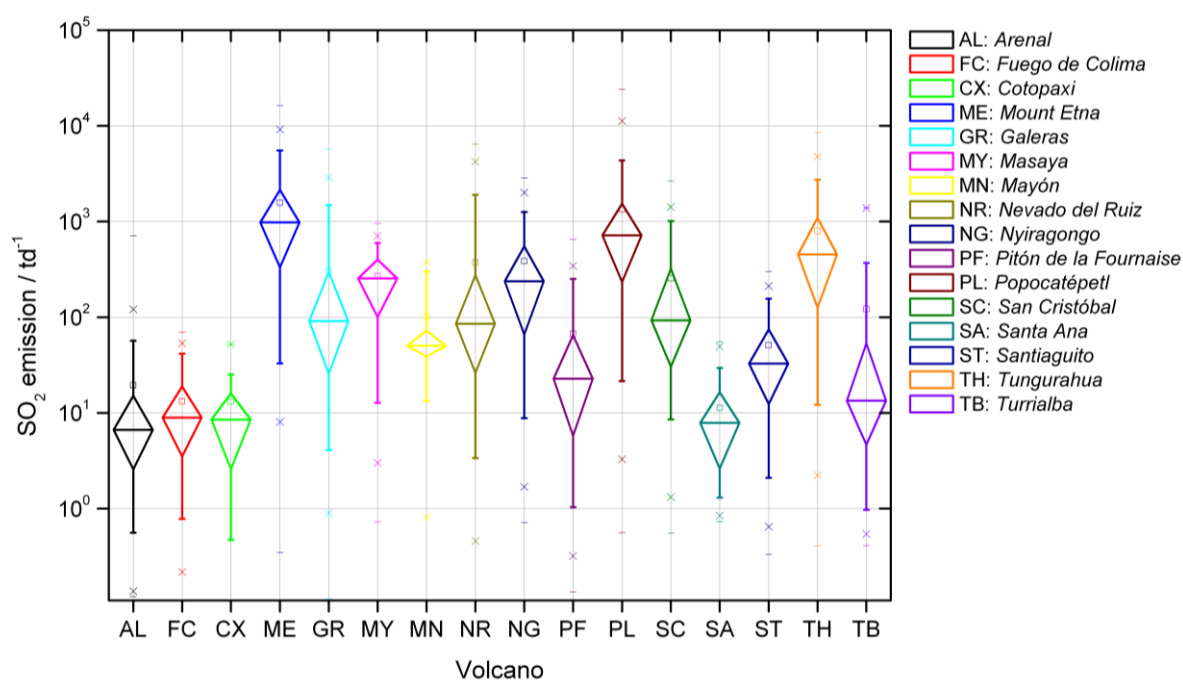


Figure 29. Box-chart plots of measurements of SO₂ emissions on 16 volcanoes of NOVAC during 2007-2013. The marks indicate the limits of the range and the 5, 25, 50, 75, and 95% quantiles, as well as the arithmetic mean. Notice the skewed distribution of emissions and the large ranges of variability for individual volcanoes as well as between different volcanoes (cf. Paper III)

It is important to emphasize the relevance of the network data: it is the largest (since 2004 for some volcanoes) and densest (40 measurements per day on average) compilation of measurements from some of the most important emitters (the network includes about 20% of the total number of volcanoes erupting in the last 40 years, Andres and Kasgnoc, 1998) and data have been obtained and evaluated in a standardized manner. This is important for effects of comparison and to determine the natural variability of the emissions of individual sources.

Figure 30 shows a map with the locations of the studied volcanoes and circles with areas representing their mean emissions. In Paper III, the statistics of NOVAC measurements are compared with previous reports in the literature. The major contribution of long-term monitoring is the possibility to characterize the distribution of degassing strength of volcanoes, allowing a better interpretation of anomalies in the rate of emission, i.e. if an

observed change can be considered within the normal range for a certain state of volcanic activity.

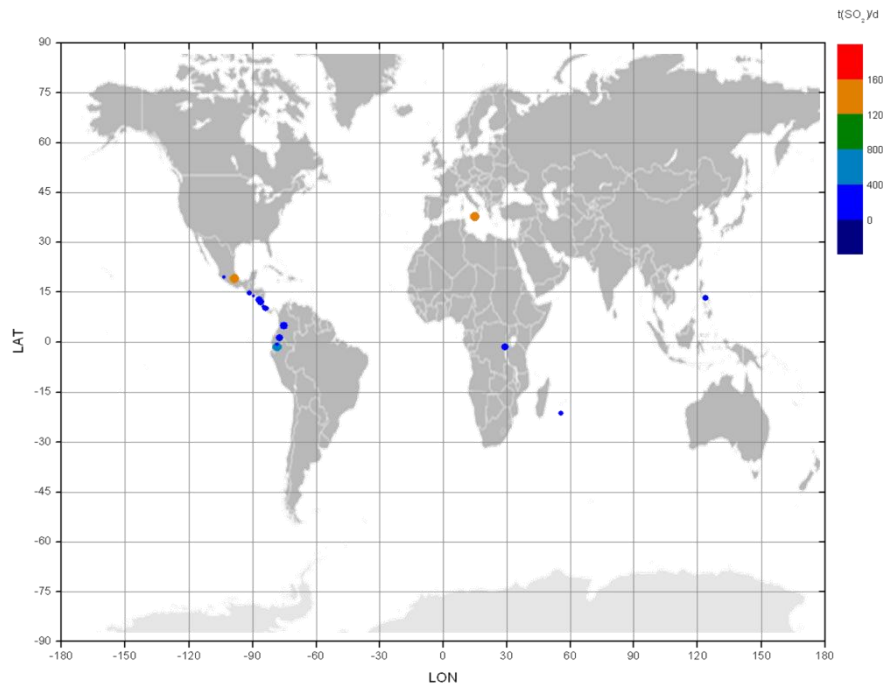


Figure 30. Map representing the mean values of SO₂ emissions from 16 volcanoes of NOVAC during 2007-2013

3.4. Geophysical models of volcanic degassing

In this section, brief descriptions of two modeling studies are presented: one focused on a particular volcano and another concerning general characteristics of passive degassing for the volcanoes in NOVAC. More studies are presented in the summary of appended and non-appended papers in the next chapter.

3.4.1. Gas emissions as a proxy of magma discharge

Paper I shows a case of a monitoring network of NOVAC instruments at Tungurahua volcano. The study gives a descriptive view of the comparison between long-term time-series of gas emission measurements on one hand, and seismicity and deformation on the other. Geophysical modeling of degassing from Tungurahua until 2006 is presented in Paper V. In this study, efficient degassing of the volcano is modeled principally as resulting from magma overturning in the conduit, as first proposed by Kazahaya et al. (1994). Further studies on the degassing mechanisms and its relation with eruptive activity after 2007 are presented in Paper IX. It has been observed that Tungurahua had a shift in eruptive activity after the VEI 2-3 events of July and August 2006, respectively. In essence, there has been a transition between almost continuous passive degassing punctuated by sporadic episodes of

explosive activity, to a sequence of short-term phases of mostly explosive activity interspersed with periods of almost complete inactivity of varying duration. Observation of the total amount of SO₂ and the duration of each of these phases after 2007 indicates the pattern shown in Figure 31.

We interpreted this observation as an indication of elastic response of the magma reservoir to discharge. The SO₂ emission rate can be seen as a proxy to the magma emission rate, mediated by the sulfur content of the magma, the speciation of sulfur as SO₂, and the partition of SO₂ between the melt and gas phases. These relations are controlled by dynamic processes and may not remain constant between different phases of activity, but their time-averaged values should not vary drastically.

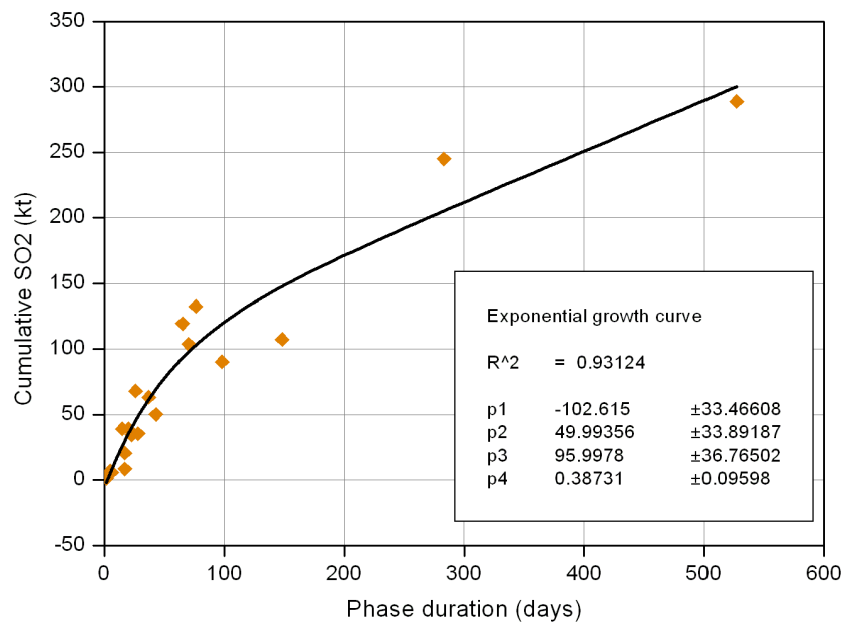


Figure 31. Cumulative emission of SO₂ vs. duration of each phase of activity of Tungurahua volcano during 2007-2013. A model of exponential growth is fitted to the data providing constraints on the magma intrusion rate, characteristic time of magma discharge and other physical conditions of the system (cf. Text and Paper IX)

The elastic reservoir model was adapted from Wadge (1981), Huppert and Woods (2002) and Mastin et al., (2008). Two basic assumptions regarding the overpressure in the reservoir as linearly proportional to the difference between intruded and erupted mass (with a proportionality coefficient depending on the compressibilities of magma and reservoir, the density of magma and the volume of the reservoir); and, the mass emission rate linearly proportional to the reservoir pressure, predict a growth curve of cumulative erupted mass M_e that follows the following relation with time t :

$$M_e = p_1 e^{-\frac{t}{p_2}} + p_3 + p_4 t \quad (42)$$

Where $p_1 = \frac{(Ap_0 - B) - \dot{M}_i}{AC}$, $p_2 = \frac{1}{AC}$, $p_3 = -p_1$, $p_4 = \dot{M}_i$, with p_0 representing the pressure at the reservoir and \dot{M}_i the rate of intrusion of magma to the reservoir. A, B, C are constants related to the physical conditions of the reservoir (initial overpressure, volume, compressibility), conduit (cross section, length) and magma (compressibility, density, viscosity). In particular, the characteristic time for discharge is given by $\tau = p_2$.

Figure 31 shows also the result of non-linear (Levenberg-Marquardt) regression of the data with the model given by equation (42). The characteristic time is found to be about 50 ± 34 d (the mean duration of the phases of activity is 79 ± 29 d). The intrusion rate is found to be 0.38 ± 0.1 kt d⁻¹, indicating a process of relatively slow recharge of the reservoir consistent with the episodic activity observed at Tungurahua.

3.4.2. The frequency distribution of passive volcanic degassing

Recalling the finding shown in Figure 29: when looking at frequent and long-term records of gas mass flow rate from volcanoes, one finds an evident and systematic skewness in the distribution of the individual measurements. Volcanoes tend to emit low amounts of gas very frequently and large outburst rarely during periods of passive degassing, which are dominant in the long term.

To explore this interesting finding Figure 32 shows the distributions of the 16 volcanoes studied in NOVAC in logarithmic scale. The probability distribution functions were estimated with a kernel density estimator (Botev et al., 2010).

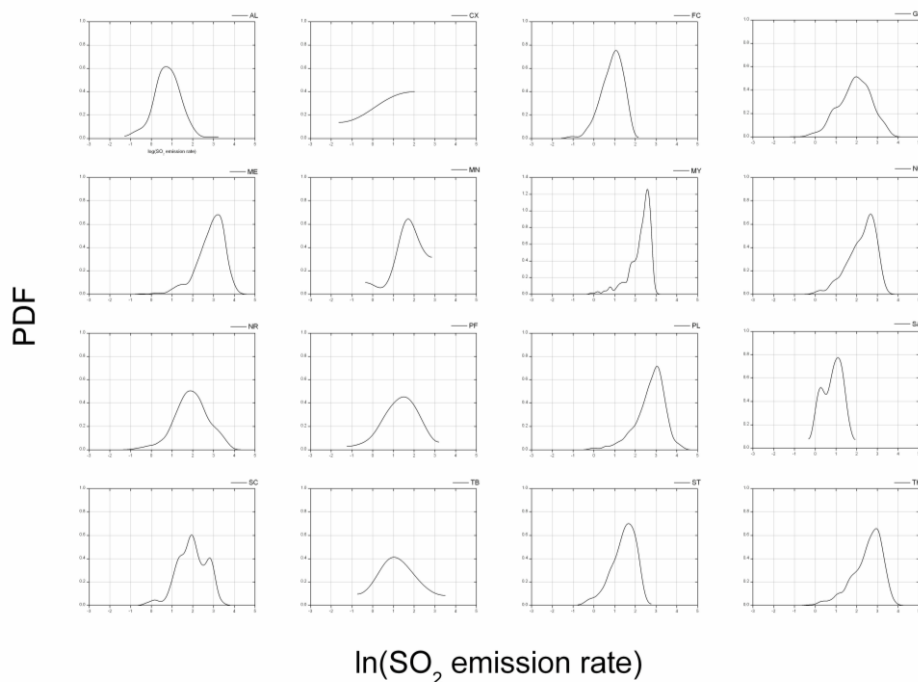


Figure 32. Frequency distribution of volcanic emission on 16 volcanoes of NOVAC

By taking the logarithmic gas emission rate, the distributions of volcanoes with large amounts of data tend to conform to a single peaked, almost symmetric distribution. It is thus interesting to work on logarithmic space. But it should be noted that the measurements of SO₂ emission may entail a considerable level of uncertainty, mostly due to radiative transfer effects and imprecisely known plume velocity (cf. Paper II). Furthermore, time series tend not to be regular, due to instrumental or environmental causes. In order to overcome these problems, I propose to use a metric of the change in the order of magnitude of two consecutive measurements of gas emission rate, defined in this way:

$$\delta(t_i) = \ln \left[\frac{\varphi(t_i)}{\varphi(t_{i-1})} \right] \quad (43)$$

This quantity, dubbed the 'flux index' that relates measurements taken close in time, has the advantage that reduces the effect of uncertainties because the common uncertain factors would to a large extent be cancelled out. To ensure this, the index is calculated for pairs of measurements which do not differ for more than 30 min. Moreover, this definition reduces possible trends in the time series, facilitating the statistical analysis of the time-series. From the series of flux indexes the flux can be reconstructed at any time:

$$\varphi(t_i) = \varphi(t_0) e^{\int_{t_0}^{t_i} \delta(t') dt'} \quad (44)$$

I applied a density kernel estimator (Botev et al., 2010) to the time series of flux indexes of the volcanoes with longer datasets in NOVAC and fit the empirical probability distribution function to different canonical distributions, namely: Gauss, Cauchy, Weibull, and Lévy distribution. All of these distributions are parametric. As a measure of the quality of the fit, least-squares, least-distance, and Kolmogorov-Smirnov tests of fitting were applied to determine which is the best model for the observed distributions. The Lévy distribution is an alpha-stable distribution characterized for resulting from a generalization of the central limit theorem and it can accommodate concentration, skewness, scale, and location by four parameters α , β , c , and μ , respectively. It emerges from the problem of finding a distribution of the sum of two distributions of the same family, which also belongs to the same family (Mantegna and Stanley, 1994). The results of the fits are shown in Figure 33.

It is interesting that for all the cases, the empirical distribution is better represented by a symmetric Lévy distribution. The fact that it is symmetric reduces the number of free parameters. Moreover, the location can be centralized by defining the initial flux index equal to zero or taking the standard flux index (shifted by the mean value and scaled by the standard deviation). The concentration parameter α varies between 0 and 2. For the case of symmetric alpha-stable distributions this parameter is 1 for the Cauchy distribution and 2 for the Gaussian distribution, which therefore can be seen as especial cases of the Lévy-type distribution.

Another important feature of this analysis is that α is quite stable for each volcano but different among volcanoes. For the cases studied here, the parameters seem to be larger for volcanoes with lower magma viscosities. Furthermore, the asymptotic behavior of the distribution tends to a power-law distribution.

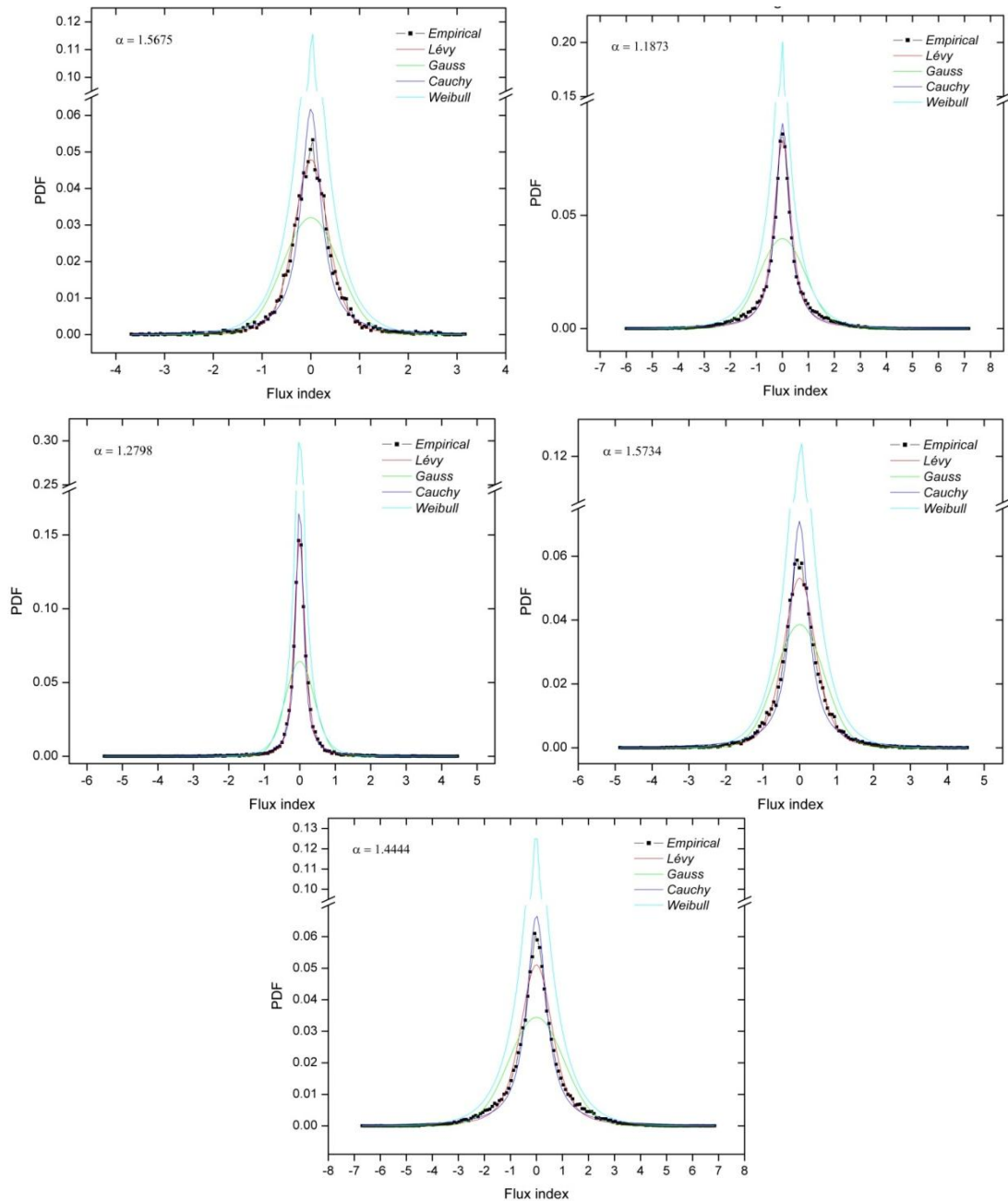


Figure 33. Frequency distribution of the flux index of 5 volcanoes in NOVAC. From above left-right to below: Nyiragongo, Tungurahua, Mount Etna, Galeras and Nevado del Ruiz. For all the cases, the best distribution is symmetric alpha-stable (Lévy-type)

Lévy processes are forms of anomalous diffusion characterized for having infinite variance. In natural systems, certain constraints such as the limited size of the systems make processes to be truncated after certain values of the Lévy-jumps (steps). The distribution of flux indexes is thus conceived as a truncated Lévy process.

The asymptotic power-law behavior is interpreted as resulting from a power-law distribution of gas parcels in the magma. The exponent of the power-law should be related to the degree of connectivity of those parcels of gas. The measure of such connectivity is the porosity of the magma, since there is a power-law relation between this parameter and the permeability, which ultimately controls the emission in passively degassing volcanoes.

The interpretation of having an alpha-stable degassing process that looks power-law after certain value of the porosity indicates that passive magma degassing is analogous to a phase transition where the running parameter is the porosity (in phase transitions, the distribution of certain magnitude tends to be power-law close to a critical value of the running parameter). It is proposed that there is a critical porosity at which volcanoes begin to emit, and the distribution of those emissions, close to the critical porosity follows a power-law.

Since different volcanoes have all shown this character we can conclude that the idea of connectivity applies to all of them. However, it is known that for instance passive degassing in basaltic volcanoes can be controlled by convection, whereas it occurs due to percolation in silicic systems. The unifying idea is that percolation occurs at different scales: for viscous systems is the percolation of cracks in the magma column that creates pathways that tend to be power-law distributed. For intermediate systems, it is the percolation of bubbles which follows such distribution. Finally, for less viscous basaltic systems, the percolation of gas-rich magma parcels is power law distributed close to a certain threshold of connectivity. The parameter α is related to these percolation mechanisms. Figure 34 shows the fits of Lévy distributions for the volcanoes analyzed.

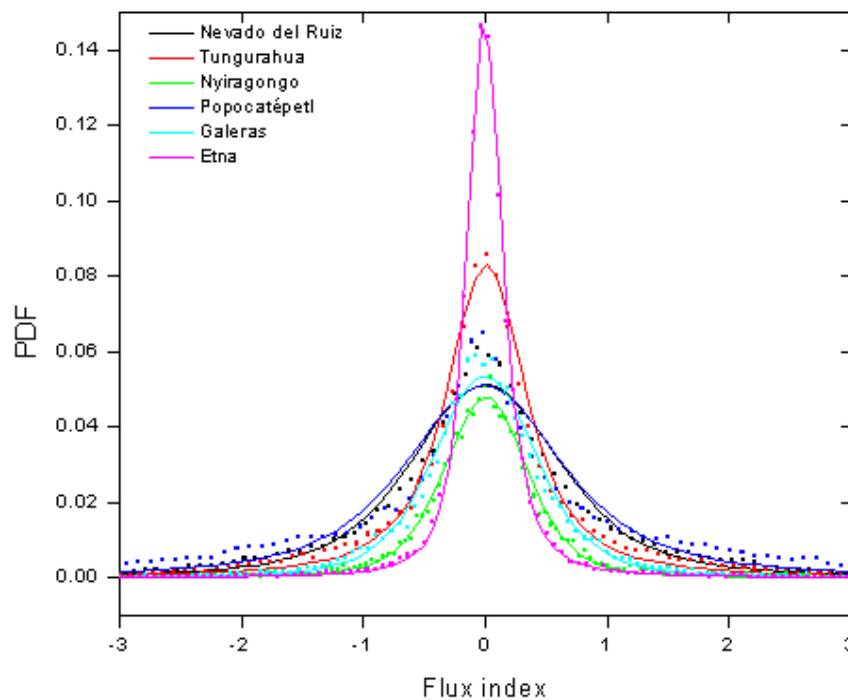


Figure 34. Fitting of the empirical probability distribution functions of the flux indexes of 6 volcanoes to a symmetric Lévy-type distribution

4. Summary of publications

- I. **“Network for Observation of Volcanic and Atmospheric Change (NOVAC)-A global network for volcanic gas monitoring: Network layout and instrument description”**
J. Geophys. Res., 115, D05304, 2010
B. Galle, M. Johansson, C. Rivera, Y. Zhang, M. Kihlman, C. Kern, T. Lehmann, U. Platt, S. Arellano, S. Hidalgo

This paper describes in detail NOVAC, the objectives of the network, its measurement strategies, instrumentation, software, error analysis, initial list of volcanoes monitored, and an example of installation and 21 months of operation at Tungurahua volcano (Ecuador). My contribution to this paper was *section 8: Installation Example* and collaborate with the edition. This work came out of my work (2003-2008) at Instituto Geofísico – EPN, and consisted in the installation of three stations around the volcano (now increased up to five), the daily operation and data evaluation, and the comparison of the retrieved time series of emission of SO₂ with deformation and seismicity measurements during a period of fluctuating levels of explosiveness in the activity of the volcano.

- II. **“Analysis of uncertainty of the time-averaged estimation of volcanic gas emission rate from scanning-DOAS measurements of tropospheric plumes”, *manuscript***
S. Arellano, B. Galle, M. Johansson, C. Kern, M. Van Roozendaal, U. Platt

In this study we analyze the total uncertainty in the estimation of daily emission rate of SO₂ from volcanoes by scanning-DOAS. The categories of model errors, parameter errors and measurement errors are clearly defined. A distinction is done between the measured plume strength and the estimated source strength, as well as between the individual samples and the time-averaged statistics. We contrasted the traditional analytical propagation of errors used in previous studies with a full numerical computation based on a Monte-Carlo sampling method. The conditions on which the analytical method is based (e.g. independence, negligible contribution of higher orders in the expansion) are rarely met in this type of measurements, from which we reach the conclusion that the full calculation is necessary and applied the method to measurements at Popocatepetl (Mexico). I designed the study, implemented the methods and wrote the paper.

- III. **“Inventory of SO₂ gas emission rate measurements from the global Network for Observation of Volcanic and Atmospheric Change (NOVAC)”, *manuscript***
S. Arellano, B. Galle, M. Johansson, P. Norman, the NOVAC collaboration

This is a compilation of results of 6 years (2007-2013) of measurements of the SO₂ mass flow rate on 16 volcanoes of NOVAC. The network, instrumentation, data evaluation and uncertainty analyses are briefly described. Time-series of daily emission rate are presented, showing the most probable value, uncertainty range and variability. Based on these series, statistical information is derived and the skewed distribution of volcanic emission, observed in nearly all cases, documented. A comparison between

the NOVAC estimates and previous published inventories is presented and a description to access the dataset provided. I analyzed the data, implemented the uncertainty and statistical methods, and wrote the paper.

- IV. “BrO/SO₂ molar ratios from scanning DOAS measurements in the NOVAC network”**
***Solid Earth*, 5, 409-424, 2014**
P. Lübcke, N. Bobrowski, S. Arellano, B. Galle, G. Garzón, L. Vogel, U. Platt

This paper presents a method to derive BrO column densities from NOVAC measurements. The significance of this result is that BrO having a typical concentration that is 5 orders of magnitude lower than SO₂ requires precision measurements, for this reason it has been measured sporadically on a few volcanoes. The possibility to exploit the rich NOVAC database will make a big contribution to understand the role of this species in volcanic and atmospheric processes. Interestingly, the BrO/SO₂ molar ratio is found to anticipate an eruptive crisis in Nevado del Ruiz volcano (Colombia) by several weeks. My contribution to this paper was the evaluation of the time-series of SO₂ emission, and help with the volcanological interpretation and writing of the manuscript.

- V. “Degassing patterns of Tungurahua volcano (Ecuador) during the 1999-2006 eruptive period, inferred from remote spectroscopic measurements of SO₂ emissions”**
***J. Volcanol. Geotherm. Res.*, 176, 151-162, 2008**
S. Arellano, M. Hall, P. Samaniego, J.L. LePennec, A. Ruiz, I. Molina, H. Yepes

We presented 7 years of measurements of volcanic degassing from Tungurahua volcano with scanning DOAS, including a discussion of errors and novel methods of data quality assurance. The results are categorized between passive and explosive periods by using a seismic index of explosiveness. Passive degassing is found to be largely dominating and the ratio between emitted SO₂ gas and (DRE) magma is found to vary between passive and explosive periods, being much larger during the former. The gas/magma ratio clearly shows a case of “excessive” degassing for which we presented two models. Based on fluid-dynamical calculations, we conclude that magma overturning in the conduit is a feasible mechanism to explain excessive passive degassing. I performed the measurements, analyzed the data, devised the models, and wrote the paper.

- VI. “Magnitude, intensity and impact of SO₂ gas emissions from Nyiragongo volcano during 2004-2012”, *manuscript***
S. Arellano, M. Yalire, B. Galle, M. Johansson, P. Norman, N. Bobrowski)

We presented 8 years of measurements with scanning-DOAS at Nyiragongo volcano (D. R. Congo), characterize the magnitude of the emissions and presented an statistical approach to infer the distribution of the order of magnitude of changes in emission, which is found to be well described as alpha-stable. This result is interpreted on the basis of percolation theory and proposed as a generic model for a wide category of volcanic systems (as supported by observations at other volcanoes in

NOVAC). I performed the data analysis, implemented the statistical and physical models and wrote the paper.

(Not included)

- VII. “Early in-flight detection of SO₂ via Differential Optical Absorption Spectroscopy: a feasible aviation safety measure to prevent potential encounters with volcanic plumes”**
***Atmos. Meas. Tech.*, 4, 1785-1804, 2011**
L. Vogel, B. Galle, C. Kern, H. Delgado, V. Conde, P. Norman, S. Arellano, O. Landgren, P. Lübcke, J.M. Álvarez, L. Cárdenas, U. Platt

This paper describes a strategy to detect volcanic SO₂ plumes by DOAS from a flying aircraft. A experiment was executed at Popocatepetl volcano during the volcanic crisis of Eyjafjallajökull in 2010, carrying a set of forward-looking DOAS instruments and supported by ground observations with scanning-DOAS. Radiative transfer modeling was used to interpret the observations, which showed the feasibility to detect a plume at typical flying altitudes from a distance of about 80 km. I participated in the field campaign conducting ground-based observations and collaborated with writing of the manuscript.

- VIII. “Detailed multidisciplinary monitoring reveals pre- and co-eruptive signals at Nyamulagira volcano (North Kivu, Democratic Republic of Congo)”**
***Bull. Volcanol.*, 76, 787, 2013**
B. Smets, N. d’Oreye, F. Kervyn, F. Albino, S. Arellano, M. Bagalwa, C. Balagizi, S. Carn, T. Darrah, J. Fernández, B. Galle, P. González, E. Head, K. Karume, D. Kavotha, F. Lukaya, N. Mashagiro, G. Mavonga, P. Norman, E. Osondu, J. Pallero, J. Pioto, S. Samsonov, M. Syauswa, D. Tedesco, K. Tiampo, C. Wauthier, M. Yalire

We combine measurements of seismicity, ground deformation, thermal flux and gas emission from ground- and satellite-based sensors to characterize the flank eruption of Nyamulagira volcano (D. R. Congo) in January 2010. This volcano has frequent, short-lasting eruptions, but this is the first multidisciplinary account of one eruptive episode. Four phases are identified, in agreement with past descriptions of the activity, but for the first time evidence of precursory signals were observed. I provided the time series of SO₂ and plume directions to separate the signal from the nearby Nyiragongo volcano. I also assisted with the writing of the paper.

- IX. “SO₂ degassing at Tungurahua volcano (Ecuador) between 2007 and 2013: transition from continuous to episodic activity”**
Submitted to J. Volcanol. Geotherm. Res.
S. Hidalgo, J. Battaglia, S. Arellano, A. Steele, B. Bernard, J. Bourquin, B. Galle, S. Arrais, F. Váscquez

This paper describes the volcanic activity of Tungurahua after 2007 and presents the results of gas emission measurements with NOVAC stations. A new method to derive

daily emitted mass is proposed which improves the correlation with seismicity. Several periods of activity are distinguished and characterized, showing that the volcano is experimenting alternation of silent and explosive phases, in contrast to the preceding years of passive but constant emission punctuated by explosive activity. A model of magma discharge is proposed to explain the relation between emitted mass of SO₂ and duration of each period of activity. I contributed with the analysis of SO₂ data, the implementation of the physical model and writing of the article.

X. "Gas emission strength and evolution of the molar ratio of BrO/SO₂ in the plume of Nyiragongo in comparison to Etna"

Accepted for publication in J. Geophys Res.

N. Bobrowski N., R. von-Glasow, G. Giuffrida, D. Tedesco, A. Aiuppa, M. Yalire, S. Arellano, M. Johansson, B. Galle

This article presents a series of measurement and modeling results to study the evolution of the BrO/SO₂ molar ratio in the plume of Nyiragongo volcano. Measurements were taken by remote sensing and direct sampling techniques at the crater rim and the plume of the volcano during field campaigns in 2004-2007. The measurements were used to initialize a geochemical model and the results of this used to explain the different molar ratios observed in the plumes of Nyiragongo and Etna (Italy) volcanoes. I provided measurements of SO₂ emission for Nyiragongo volcano.

XI. "Daily monitoring of Ecuadorian volcanic degassing from space"

J. Volcanol. Geotherm. Res., 176, 1, 141-150, 2008

S.A. Carn, A.J. Krueger, S. Arellano, N.A. Krotkov, K. Yang

We present a survey of measurements of volcanic SO₂ degassing with the Ozone Monitoring Instrument (OMI) onboard NASA's EOS/Aura satellite during 2004-2006 in Ecuador and southern Colombia. The spatial and temporal resolution of OMI allows unprecedented detection of passive degassing on a daily basis. During the study period, the bulk of emissions is attributed almost entirely to Tungurahua (40%), El Reventador (30%) and Galeras (30%) volcanoes. Comparisons with seismicity and ground-based observations are provided. My contribution consisted in the analysis of ground-based data and description of activity of the Ecuadorian volcanoes.

5. Conclusions and outlook

"The real difficulty about vulcanism is not to see how it can start, but how it can stop."

— Harold Jeffreys²¹

This doctoral thesis summarizes the most important work done by the author during 2009-2014 on the field of remote spectroscopic sensing of volcanic gases in the atmosphere. Several aspects of this work include:

Instrumental development- A stationary solar tracker which uses a passive sun tracking algorithm and occasional active fine tuning was designed, built and calibrated. The system is fully operational and it has been used for field-campaigns on the volcanoes: Popocatépetl, Tungurahua and Nyiragongo. An internal report (Arellano, 2014) describes the components and mode of operation of this instrument. Additionally, dozens of scanning-DOAS, mobile-DOAS and rapid-deployment NOVAC systems have been assembled, calibrated and sent to volcanological observatories, which staffs have been trained for the use or maintenance of the instruments.

Measurements- Field campaigns with DOAS and FTIR systems were conducted on the volcanoes Popocatépetl, Fuego de Colima, Santiaguito, Telica, Tungurahua, Cotopaxi, Karymsky, Gorely, Mutnovsky, and Nyiragongo. We tested solar-FTIR, open-path FTIR, scanning and mobile DOAS and wind measurements with a wide-field-of-view DOAS system. Assistance for field campaigns in Fuego de Colima and Ubinas was also provided.

Data analysis- Spectroscopic analysis of FTIR (solar, open-path) and DOAS (scanning, mobile) was done for data collected in field campaigns or short periods of observation, as well as for the whole database of NOVAC since 2004. This includes attention to special requests of colleagues from collaborating volcanological observatories during periods of heightened activity at several volcanoes, not reported in this thesis. The post-processing for NOVAC was based on the code developed by M. Johansson with improvements in certain subroutines. An in-depth analysis of measurement uncertainty and methods to select and combine measurements from different instruments resulted in different codes used for the computationally demanding task to analyze such important volume of data.

Statistical analysis- New methods for the analysis of uncertainty, combination of measurements and derivation of probability distribution functions were developed and applied to the NOVAC database. This resulted in particular, in the finding of a general form of the distribution of an index measuring the variation in the order of magnitude change of consecutive emissions. The large amount of data generated and validated has permitted to conduct studies of high statistical significance.

Physical modeling- After developing instruments, performing observations, analyzing the data and finding patterns, the challenge is to explain those patterns, i.e. finding their underlying causes. The modalities of degassing for Tungurahua were modeled to explain both the mechanism of passive emissions and the recharge/discharge rate of the magma reservoir. Measurements of the SO₂/BrO molar ratio resulted in a signal that anticipated with

²¹ "Earthquakes and Mountains", 1950, p.187

several weeks the occurrence of a major explosive event. Passive degassing of the convective lava lake system at Nyiragongo was modeled as a Lévy process. The generated time series of SO₂ emission were used to study the plume processing of BrO at Nyiragongo. The converging distributions of the flux index of several volcanoes were interpreted as the result of percolation mechanisms at the level of magma batches, bubbles and cracks in the conduit.

Future work is required to maintain the processing flow of the NOVAC dataset and its distribution to interested users. It is interesting to explore in more detail the models of magmatic degassing and their relation with other monitored variables of volcanic activity. Regarding the sources of uncertainty in remote sensing of SO₂ by the scanning-DOAS method, more work is needed to quantify or correct for the effects of radiative transfer and to implement the findings in an operational analyzing code. It would also be interesting to explore further the information contained in the spectra collected in the network, to expand the retrieval of other species such as BrO to several volcanoes, or to find strategies to identify ash or meteorological interfering clouds. The combination of FTIR and DOAS requires further automation and use, because both make a powerful tool to investigate the composition and dynamics of volcanic emissions and their source mechanisms.

6. References

- Afe, O.T., Richter, A., Sierk, B., Wittrock, F. and Burrows, J.P., 2004. BrO emission from volcanoes: A survey using GOME and SCIAMACHY measurements. *Geophysical Research Letters*, 31(24): L24113.
- Allard, P., Burton, M. and Mure, F., 2005. Spectroscopic evidence for a lava fountain driven by previously accumulated magmatic gas. *Nature*, 433(7024): 407-410.
- Allard, P., Carbonnelle J., Dajlevic, D., Le Bronec, J., Morel, P., Robe, M., Maurenas, J., Faivre-Pierret, R., Martin, D., Sabroux, J. and Zettwoog P., 1991. Eruptive and Diffuse Emissions of Co₂ from Mount Etna. *Nature*, 351(6325): 387-391.
- Allègre, J.C., Staudacher, T. and Sarda, P., 1987. Rare gas systematics: formation of the atmosphere, evolution and structure of the Earth's mantle. *Earth and Planetary Science Letters*, 81: 127-150.
- Andres, R.J. and Kasgnoc, A.D., 1998. A time-averaged inventory of subaerial volcanic sulfur emissions. *Journal of Geophysical Research D: Atmospheres*, 103(D19): 25251-25261.
- Arellano, S., 2014. Chalmers Stationary Solar Tracker-User Manual. Report, Optical Remote Sensing Group, Chalmers University of Technology, Gothenburg, pp 5.
- Beer, R., 1992. Remote Sensing by Fourier Transform Spectrometry. Chemical Analysis. John Wiley & Sons, Inc., Toronto, 153 pp.
- Bluth, G.J.S., Shannon, J.M., Watson, I.M., Prata, A.J. and Realmuto, V.J., 2007. Development of an ultra-violet digital camera for volcanic SO₂ imaging. *Journal of Volcanology and Geothermal Research*, 161(1-2): 47-56.
- Bobrowski, N., 2005. Volcanic Gas Studies by Multi Axis Differential Optical Absorption Spectroscopy. PhD Thesis, University of Heidelberg, Heidelberg, 215 pp.
- Bobrowski, N., Hönninger, G., Lohberger, F. and Platt, U., 2006. IDOAS: A new monitoring technique to study the 2D distribution of volcanic gas emissions. *Journal of Volcanology and Geothermal Research*, 150(4): 329-338.
- Bobrowski, N., Hönninger, G., Platt, U. and Galle, B., 2003. Detection of bromine monoxide in a volcanic plume. *Nature*, 423(6937): 273-276.
- Bohren, C.F. and Clothiaux, E., 2006. Fundamentals of atmospheric radiation: an introduction with 400 problems. Wiley-VCH, 472 pp.
- Bohren, C.F. and Huffman, D.R., 1998. Absorption and Scattering of Light by Small Particles. Wiley, 544 pp.
- Boichu, M., Oppenheimer, C., Tsanev, V. and Kyle, P.R., 2010. High temporal resolution SO₂ flux measurements at Erebus volcano, Antarctica. *Journal of Volcanology and Geothermal Research*, 190(3-4): 325-336.
- Botev, Z.I., Grotowski, J.F. and Kroese, D. P., 2010. Kernel density estimation via diffusion. *Annals of Statistics*, 38, 5, 2916-2957.
- Bourassa, A.E., Robock A., William, R., Deshler, T., Rieger, L., Lloyd, N., Llewellyn, T. and Dagenstein, D., 2012. Large Volcanic Aerosol Load in the Stratosphere Linked to Asian Monsoon Transport. *Science*, 337(6090): 78-81.
- Bransden, B.H. and Joachain, C.J., 2003. Physics of Atoms and Molecules (2nd Edition). Pearson education, Malaysia, 1114 pp.
- Burton, M.R., Oppenheimer, C., Horrocks, L.A. and Francis, P.W., 2001. Diurnal changes in volcanic plume chemistry observed by lunar and solar occultation spectroscopy. *Geophysical Research Letters*, 28(5): 843-846.
- Butler, J., Johnson, B.C. and Barnes, R.A., 2005. The Calibration and Characterization of Earth Remote Sensing and Environmental Monitoring Instruments, Optical Radiometry. *Experimental Methods in the Physical Sciences*. Elsevier Academic Press, pp. 453-534.
- Carn, S.A., Krotkov, N. A., Yang, K., Hoff, R. M., Prata, A. J., Krueger, A. J., Loughlin, S. C., and Levelt, P. F., 2007. Extended observations of volcanic SO₂ and sulfate aerosol in the stratosphere. *Atmospheric Chemistry and Physics Discussion*, 7(1): 2857-2871.
- Chance, K.V. and Spurr, R.J.D., 1997. Ring effect studies: Rayleigh scattering, including molecular parameters for rotational Raman scattering, and the Fraunhofer spectrum. *Applied Optics*, 36(21): 5224-5230.
- Clarisse, L., Coheur, P., Prata, A., Hurtmans, D., Razavi, A., Phulpin, T., Hadji-Lazaro, J., Clerbaux, C., 2008. Tracking and quantifying volcanic SO₂ with IASI, the September 2007 eruption at Jebel at Tair. *Atmospheric Chemistry and Physics*, 8(24): 7723-7734.
- Conde, V., 2011. Development and implementation of a rapid deployment system for volcanic gas emissions monitoring. Chalmers University of Technology.
- Conde, V., Robidou, P., Avard, G., Galle, B., Aiuppa, A., Muñoz, A., Giudice, G., 2014. Measurements of volcanic SO₂ and CO₂ fluxes by combined DOAS, Multi-GAS and FTIR observations: a case study from Turrialba and Telica volcanoes.

- Connor, C.B., Stoiber, R.E. and Malinconico, L.L., Jr., 1988. Variation in Sulfur Dioxide Emissions Related to Earth Tides, Halemaumau Crater, Kilauea Volcano, Hawaii. *J. Geophys. Res.*, 93(B12): 14867-14871.
- Datla, R.U. and Parr, A., 2005. Introduction to Optical Radiometry, *Optical Radiometry. Experimental Methods in the Physical Sciences.* Elsevier Academic Press, pp. 1-34.
- Davis, S.P., Abrams, M.C. and Brault, J.W., 2001. *Fourier Transform Spectrometry.* Elsevier Science, 262 pp.
- Diaz, J.A., Giese, C.F. and Gentry, W.R., 2002. Mass spectrometry for in-situ volcanic gas monitoring. *TrAC Trends in Analytical Chemistry*, 21(8): 498-514.
- Dingwell, D.B., 1996. Volcanic Dilemma--Flow or Blow? *Science*, 273(5278): 1054-1055.
- Duffell, H.J., Oppenheimer, C., Pyle, D., Galle, B., McGonigle, A., Burton, M., 2003. Changes in gas composition prior to a minor explosive eruption at Masaya volcano, Nicaragua. *Journal of Volcanology and Geothermal Research*, 126(3-4): 327-339.
- Eisinger, M. and Burrows, J.P., 1998. Tropospheric sulfur dioxide observed by the ERS-2 GOME instrument. *Geophysical Research Letters*, 25(22): 4177-4180.
- Elachi, C. and Van Zyl, J., 2006. *Introduction to the Physics and Techniques of Remote Sensing (2nd Edition).* John Wiley & Sons.
- Fischer, T.P., Roggensack, K. and Kyle, P.R., 2002. Open and almost shut case for explosive eruptions: Vent processes determined by SO₂ emission rates at Karymsky volcano, Kamchatka *Geology*, 30(12): 1059-1062.
- Francis, P., Burton, M.R. and Oppenheimer, C., 1998. Remote measurements of volcanic gas compositions by solar occultation spectroscopy. *Nature*, 396(6711): 567-570.
- Galle, B., Johansson M, Rivera C, Zhang Y, Kihlman M, Kern C, Lehmann T, Platt U, Arellano S, and Hidalgo S, 2010. Network for Observation of Volcanic and Atmospheric Change (NOVAC): A global network for volcanic gas monitoring -Network layout and instrument description. *Journal of Geophysical Research*, 115(D5): D05304.
- Galle, B., Mellqvist, J., Arlander, D., Floisand, I, Chipperfield, M., and Lee, A., 1999. Ground based FTIR measurements of stratospheric species from Harestua, Norway during SESAME and comparison with models. *Journal of Atmospheric Chemistry*, 32(1): 147-164.
- Galle, B., Oppenheimer, C., Geyer, A., McGonigle, A., Edmonds, M., and Horrocks, L., 2003. A miniaturised ultraviolet spectrometer for remote sensing of SO₂ fluxes: a new tool for volcano surveillance. *Journal of Volcanology and Geothermal Research*, 119(1-4): 241-254.
- Gao, C., Robock, A. and Ammann, C., 2008. Volcanic forcing of climate over the past 1500 years: An improved ice core-based index for climate models. *J. Geophys. Res.*, 113(D23): D23111.
- Gerlach, T.M., 2011. Volcanic versus anthropogenic carbon dioxide. *Eos Trans. AGU*, 92(24): 201-202.
- Gianfrani, L. and De Natale, P., 2000. Remote Measurements of Volcanic Gases With a Diode-Laser-Based Spectrometer. *Opt. Photon. News*, 11(12): 44-44.
- Gleckler, P.J., AchutaRao, K., Gregory, J., Santer, D., Taylor, K. and Wigley, T. M. L., 2006. Krakatoa lives: The effect of volcanic eruptions on ocean heat content and thermal expansion. *Geophys. Res. Lett.*, 33(17): L17702.
- Gonnermann, H.M. and Manga, M., 2006. The Fluid Mechanics Inside a Volcano. *Annual Review of Fluid Mechanics*, 39(1): 321-356.
- Grainger, R.G. and Highwood, E.J., 2003. Changes in stratospheric composition, chemistry, radiation and climate caused by volcanic eruptions. Geological Society, London, Special Publications, 213(1): 329-347.
- Grattan, J., Durand, M. and Taylor, S., 2003. Illness and elevated human mortality in Europe coincident with the Laki Fissure eruption. Geological Society, London, Special Publications, 213(1): 401-414.
- Griffith, D., 1996. Synthetic calibration and quantitative analysis of gas-phase FT-IR spectra. *Applied Spectroscopy*, 50(1): 59-70.
- Griffiths, P. and De Haseth, J.A., 2007. *Fourier Transform Infrared Spectrometry. Chemical Analysis: A Series of Monographs on Analytical Chemistry and Its Applications.* John Wiley & Sons, 704 pp.
- Halmer, M., Schmincke, H.-U. and Graf, H.-F., 2002. The annual volcanic gas input into the atmosphere, in particular into the stratosphere: a global data set for the past 100 years. *Journal of Volcanology and Geothermal Research*, 115, 3-4, 511-528, doi:10.1016/S0377-0273(01)00318-3.
- Hamilton, P.M., Varey, R.H. and Millan, M.M., 1978. Remote sensing of sulphur dioxide. *Atmospheric Environment*, 12(1-3): 127-133.
- Hansen, J.E. and Travis, L.D., 1974. Light-Scattering in Planetary Atmospheres. *Space Science Reviews*, 16(4): 527-610.
- Herman, J., Cede, A., Spinei, E. Mount, J., Tzortziou, M., and Abuhassan, N., 2009. NO₂ column amounts from ground-based Pandora and MFDOAS spectrometers using the direct-sun DOAS technique: Intercomparisons and application to OMI validation. *Journal of Geophysical Research-Atmospheres*, 114.
- Herzberg, G., 1950. *Molecular spectra and molecular structure*, 1-3. Van Nostrand, New York.

- Hönninger, G., von Friedeburg, C. and Platt, U., 2004. Multi axis differential optical absorption spectroscopy (MAX-DOAS). *Atmospheric Chemistry and Physics*, 4(1): 231-254.
- Huppert, H., Woods, A., 2002. The role of volatiles in magma chamber dynamics. *Nature* 420, 493-495, doi:10.1038/nature01211.
- Jackson, M.G., Carlson, R., Kurz, M., Kempton, P., Francis, D., and Blusztajn, J., 2010. Evidence for the survival of the oldest terrestrial mantle reservoir. *Nature*, 466(7308): 853-856.
- Jaupart, C. and Allègre, C.J., 1991. Gas content, eruption rate and instabilities of eruption regime in silicic volcanoes. *Earth and Planetary Science Letters*, 102(3-4): 413-429.
- JCGM, 2008. Evaluation of measurement data - Guide to the expression of uncertainty in measurement. In: BIPM (Editor), JCGM 100:2008, pp. 120
- Jennings, S.G., 1988. The Mean Free-Path in Air. *Journal of Aerosol Science*, 19(2): 159-166.
- Johansson, M., 2009. Application of Passive DOAS for Studies of Megacity Air Pollution and Volcanic Gas Emissions, Chalmers University of Technology, Gothenburg, 64 pp.
- Johansson, M., Galle, B., Zhang, Y. and Rivera, C., 2009. The dual-beam mini-DOAS technique—measurements of volcanic gas emission, plume height and plume speed with a single instrument. *Bulletin of Volcanology*, 71(7): 747-751.
- Johnson, J.B. and Lees, J.M., 1998. Degassing explosions at Karymsky volcano, Kamchatka. *Geophysical Research Letters*, 25(21): 3999-4002.
- Johnson, J.B. and Lees, J.M., 2000. Plugs and chugs: seismic and acoustic observations of degassing explosions at Karymsky, Russia and Sangay, Ecuador. *Journal of Volcanology and Geothermal Research*, 101(1): 67-82.
- Kazahaya, K., Shinohara, H., and Saito, G., 1994. Excessive degassing of Izu-Oshima volcano: magma convection in a conduit. *Bulletin of Volcanology* 56, 3, 207-216, doi.:10.1007/BF00279605.
- Kern, C., 2009. Spectroscopic Measurements of Volcanic Gas Emissions in the Ultra-Violet Wavelength Region, University of Heidelberg, Heidelberg, 318 pp.
- Kern, C., Deutschmann, T., Vogel, L., Wöhrbach, M., Wagner, T., and Platt, U., 2010. Radiative transfer corrections for accurate spectroscopic measurements of volcanic gas emissions. *Bulletin of Volcanology*, 72(2): 233-247.
- Kern, C., Trick, S., Rippel, B. and Platt, U., 2006. Applicability of light-emitting diodes as light sources for active differential optical absorption spectroscopy measurements. *Appl. Opt.*, 45(9): 2077-2088.
- Kihlman, M., 2005. Application of Solar FTIR Spectroscopy for Quantifying Gas Emissions, Chalmers University of Technology, Gothenburg, 67 pp.
- Kingston, R.H., 1995. Optical Sources, Detectors, and Systems: Fundamentals and Applications. *Optics and Photonics*. Academic Press, London, 198 pp.
- Krueger, A.J., Walter, L., Bhartia, P., Schnetzler, C., Krotkov, N., Sprod, I., and Bluth, G., 1995. Volcanic sulfur dioxide measurements from the total ozone mapping spectrometer instrument. *Journal of Geophysical Research*, 100(D7): 14057-14076.
- Kurucz, R.L. and Bell, B., 1995. Atomic Line Data. Smithsonian Astrophysical Laboratory.
- Kurucz, R.L., Furenlid, I., Brault, J. and Testerman, L., 1984. Solar flux atlas from 296 nm to 1300 nm.
- La Spina, A., Burton, M., Harig, R., Mure, F., Rusch, P., Jordan, M., and Caltabiano, T., 2013. New insights into volcanic processes at Stromboli from Cerberus, a remote-controlled open-path FTIR scanner system. *Journal of Volcanology and Geothermal Research*, 249(0): 66-76.
- Levenberg, K., 1944. A method for the solution of certain non-linear problems in least squares. *Quarterly of Applied Mathematics*, 2: 164-168.
- Love, S.P., Goff, F., Counce, D., Siebe, C. and Delgado, H., 1998. Passive infrared spectroscopy of the eruption plume at Popocatepetl volcano, Mexico. *Nature*, 396(6711): 563-567.
- Major, J. and Newhall, C., 1989. Snow and ice perturbation during historical volcanic eruptions and the formation of lahars and floods. *Bulletin of Volcanology*, 52(1): 1-27.
- Mantegna, R., and Stanley, E., 1994. Stochastic processes with slow convergence to the Gaussian: the truncated Lévy flight. *Physical Review Letters*, 73, 22, 2946-2949.
- Marquardt, D.W., 1963. An algorithm for least-squares estimation of nonlinear parameters. *Journal of the Society for Industrial and Applied Mathematics*, 11(2): 431-441.
- Massol, H. and Koyaguchi, T., 2005. The effect of magma flow on nucleation of gas bubbles in a volcanic conduit. *Journal of Volcanology and Geothermal Research*, 143(1-3): 69-88.
- Mastin, L., Roeloffs, E., Beeler, N., and Quick, J., 2008. Constraints on the size, overpressure, and volatile content of the Mount St. Helens magma system from geodetic and dome-growth measurements during the 2004-2006+ eruption: Chapter 22 in *A volcano rekindled: the renewed eruption of Mount St. Helens, 2004-2006*, USGS Professional Paper: 1750-22.
- Matthews, A.J., Barclay, J., Carn, S., Thompson G., Alexander, J., Herd, R., and Williams, C., 2002. Rainfall-induced volcanic activity on Montserrat. *Geophys. Res. Lett.*, 29(13): 1644.
- McGonigle, A.J.S., Aiuppa, A. and Ripepe, M., 2009. Spectroscopic capture of 1 Hz volcanic SO₂ fluxes and integration with volcano geophysical data. *Geophysical Research Letters*, 36(21): doi:10.1029/2009GL040494.

- Melnik, O., Barmin, A.A. and Sparks, R.S.J., 2005. Dynamics of magma flow inside volcanic conduits with bubble overpressure buildup and gas loss through permeable magma. *Journal of Volcanology and Geothermal Research*, 143(1/3): 53-68.
- Merlaud, A., De Maziere, M., Hermans, C. and Cornet, A., 2012. Equations for Solar Tracking. *Sensors*, 12(4): 4074-4090.
- Miller, G.H., Geirsdóttir, Á., Zhong, Y., Larsen, D., Otto-Bliesner, B., Holland, M., Bailey, D., Refsnider, K., Lehman, S., Southon, J., Anderson, C., Björnsson, H., and Thordarson, T., 2011. Abrupt onset of the Little Ice Age triggered by volcanism and sustained by sea-ice/ocean feedbacks. *Geophysical Research Letters*, 39(2): L02708.
- Moffat, A.J. and Millan, M.M., 1971. The applications of optical correlation techniques to the remote sensing of SO₂ plumes using sky light. *Atmospheric Environment*, 5(8): 677-690.
- Mori, T. and Notsu, K., 1997. Remote CO, COS, CO₂, SO₂, HCl detection and temperature estimation of volcanic gas. *Geophysical Research Letters*, 24(16): 2047-2050.
- Neely, R.R., Toon, O., Solomon, S., Vernier, J.P., Alvarez, C., English, J., Rosenlof, K., Mills, M., Bardeen, C., Daniel, J., and Thayer, J., 2013. Recent anthropogenic increases in SO₂ from Asia have minimal impact on stratospheric aerosol. *Geophysical Research Letters*, 40(5): 999-1004.
- Notsu, K., Mori, T., Igarashi, G. and Tohjima, Y., 1993. Infrared spectral radiometer: A new tool for remote measurement of SO₂ of volcanic gas. *Geochemical Journal*, 27: 361-366.
- Oppenheimer, C., 2011. *Eruptions that shook the world*. Cambridge University Press, 408 pp.
- Oppenheimer, C., Bani, P., Calkins, J.A., Burton, M.R. and Sawyer, G.M., 2006. Rapid FTIR sensing of volcanic gases released by Strombolian explosions at Yasur volcano, Vanuatu. *Applied Physics B-Lasers and Optics*, 85(2-3): 453-460.
- Ozerov, A., Ispolatov, I. and Lees, J., 2001. Modeling eruptions of Karymsky volcano. Arxiv preprint physics/0106069.
- Parfitt, E. and Wilson, L., 2008. *Fundamentals of Physical Volcanology*. John Wiley & Sons, 256 pp.
- Pinardi, G., van Roozendaal, M. and Fayt, C., 2007. The influence of spectrometer temperature variability on the data retrieval of SO₂. 44-48.
- Platt, U. and Stutz, J., 2008. *Differential Optical Absorption Spectroscopy Principles and Applications*. Physics of Earth and Space Environments. Springer, 597 pp.
- Prata, A.J. and Bernardo, C., 2007. Retrieval of volcanic SO₂ column abundance from Atmospheric Infrared Sounder data. *Journal of Geophysical Research*, 112(D20): D20204.
- Prata, A.J. and Bernardo, C., 2009. Retrieval of volcanic ash particle size, mass and optical depth from a ground-based thermal infrared camera. *Journal of Volcanology and Geothermal Research*, 186(1-2): 91-107.
- Prata, A.J. and Kerkmann, J., 2007. Simultaneous retrieval of volcanic ash and SO₂ using MSG-SEVIRI measurements. *Geophys. Res. Lett.*, 34(5): L05813.
- Robock, A., 2000. Volcanic eruptions and climate. *Reviews of Geophysics*, 38(2): 191-219.
- Robock, A., 2005. Cooling following large volcanic eruptions corrected for the effect of diffuse radiation on tree rings. *Geophys. Res. Lett.*, 32(6): L06702.
- Robock, A. and Matson, M., 1983. Circumglobal transport of the El Chichon volcanic dust cloud. *Science*, 221: 195-197.
- Robock, A. and Oppenheimer, C., 2003. *Volcanism and the Earth's Atmosphere*. Geophys. Monogr. Ser. AGU, Washington, DC, 360 pp.
- Rodgers, C., 2000. *Inverse Methods for Atmospheric Sounding : Theory and Practice*. Atmospheric Oceanic and Planetary Physics. World Scientific Pub Co Inc.
- Rosenkranz, P.W., 1993. Absorption of microwaves by atmospheric gases. Chapter 2 in *Atmospheric Remote Sensing By Microwave Radiometry*, (edited by M.A. Janssen). John Wiley & Sons, Inc. (New York).
- Sakurai, J.J., 1967. *Advanced quantum mechanics*. Addison-Wesley series in advanced physics. Addison-Wesley Pub. Co., Reading, Mass., 336 pp.
- Sawyer, G.M., Carn, S.A., Tsanev, V.I., Oppenheimer, C. and Burton, M., 2008. Investigation into magma degassing at Nyiragongo volcano, Democratic Republic of the Congo. *Geochemistry Geophysics Geosystems*, 9(2).
- Scarpa, R. and Tilling, R.I., 1996. *Monitoring and Mitigation of Volcano Hazards*. Springer, 841 pp.
- Seinfeld, J.H. and Pandis, S.N., 2006. *Atmospheric Chemistry and Physics - From Air Pollution to Climate Change (2nd Edition)*. John Wiley & Sons, 1225 pp.
- Shinohara, H., 2005. A new technique to estimate volcanic gas composition: plume measurements with a portable multi-sensor system. *Journal of Volcanology and Geothermal Research*, 143(4): 319-333.
- Shinohara, H. and Tanaka, H., 2012. Conduit magma convection of a rhyolitic magma: Constraints from cosmic-ray muon radiography of Iwodake, Satsuma-Iwojima volcano, Japan. *Earth and Planetary Science Letters*, 349-350(0): 87-97.

- Sigmundsson, F., Hreinsdóttir, S., Hooper, A., Árnadóttir, T., Pedersen, R., Roberts, M., Óskarsson, N., Auriac, A., Decriem, J., Einarsson, P., Geirsson, H., Hensch, M., Ófeigsson, B., Sturkell, E., Sveinbjörnsson, H., and Feigl, K., 2012. Intrusion triggering of the 2010 Eyjafjallajökull explosive eruption. *Nature*, 468(7322): 426-430.
- Simkin, T., 1993. Terrestrial Volcanism in Space and Time. *Annual Review of Earth and Planetary Sciences*, 21: 427-452.
- Simkin, T. and Siebert, L., 1984. Explosive Eruptions in Space and Time. *Explosive Volcanism Inception, Evolution and Hazards*. National Academy Press, Washington DC, 110-124 pp.
- Simkin, T. and Siebert, L., 1999. Earth's Volcanoes and Eruptions: an Overview, *Encyclopedia of Volcanoes*. Academic Press, pp. 249-261.
- Slezin, Y.B., 2003. The mechanism of volcanic eruptions (a steady state approach). *Journal of Volcanology and Geothermal Research*, 122(1): 7-50.
- Sommer, T., 2008. Direct sun light measurements of trace gases in volcanic plumes using differential optical absorption spectroscopy, Heidelberg University, Heidelberg, 126 pp.
- Sparks, R.S.J., 2003. Dynamics of magma degassing. *Geological Society, London, Special Publications*, 213(1): 5-22.
- Sparks, R.S.J., Biggs, J. and Neuberg, J.W., 2012. Monitoring Volcanoes. *Science*, 335(6074): 1310-1311.
- Stix, J., Morrow, W.H., Nicholls, R. and Charland, A., 1996. Infrared remote sensing of CO and COS gas emitted by the Galeras volcano, Colombia, January 8-10, 1993. *Canadian Journal of Remote Sensing*, 22(3): 297-304.
- Stoiber, R.E. and Jepsen, A., 1973. Sulfur dioxide contributions to the atmosphere by volcanoes. *Science*, 182(4112): 577-578.
- Stoiber, R.E., Williams, S.N. and Huebert, B., 1987. Annual contribution of sulfur dioxide to the atmosphere by volcanoes. *Journal of Volcanology and Geothermal Research*, pp. 1-8.
- Sturkell, E., Sigmundsson, F., Geirsson, H., Ólafsson, H. and Theodórsson, T., 2008. Multiple volcano deformation sources in a post-rifting period: 1989–2005 behaviour of Krafla, Iceland constrained by levelling, tilt and GPS observations, *Journal of Volcanology and Geothermal Research*, 177, 2, 405-417, doi:10.1016/j.jvolgeores.2008.06.013.
- Stremme, W., Ortega, I., Siebe, C. and Grutter, M., 2011. Gas composition of Popocatepetl Volcano between 2007 and 2008: FTIR spectroscopic measurements of an explosive event and during quiescent degassing. *Earth and Planetary Science Letters*, 301(3-4): 502-510.
- Svanberg, S., 2003. *Atomic and Molecular Spectroscopy: Basic Aspects and Practical Applications* (Fourth edition). Springer Series on Atomic, Optical and Plasma Physics. Springer, Germany, 588 pp.
- Taran, Y.A., 2009. Geochemistry of volcanic and hydrothermal fluids and volatile budget of the Kamchatka-Kuril subduction zone. *Geochimica Et Cosmochimica Acta*, 73(4): 1067-1094.
- Textor, C., Graf, H.F., Timmreck, C. and Robock, A., 2003. Emissions from volcanoes. In: C. Granier, C. Reeves and P. Artaxo (Editors), *Emissions of Chemical Compounds and Aerosols in the Atmosphere*. Kluwer, Dordrecht.
- Thomas, G. and Stammes, K., 1999. *Radiative Transfer in the Atmosphere and Ocean*. Atmospheric and Space Science Series. Cambridge University Press, 517 pp.
- Urai, M., 2004. Sulfur dioxide flux estimation from volcanoes using Advanced Spaceborne Thermal Emission and Reflection Radiometer: a case study of Miyakejima volcano, Japan. *Journal of Volcanology and Geothermal Research*, 134(1-2): 1-13.
- van Geffen, J.H.G.M. and van Oss, R.F., 2003. Wavelength calibration of spectra measured by the Global Ozone Monitoring Experiment by use of a high-resolution reference spectrum. *Applied Optics*, 42(15): 2739-2753.
- van Roozendaal, M., Pinardi, G., Hermans, C., Fayt, C. and Merlaud, A., 2006. MiniDOAS calibration issues. Second NOVAC retrieval workshop.
- Vandaele, A.C., Simon, P.C., Guilmot, J.M., Carleer, M. and Colin, R., 1994. SO₂ Absorption Cross-Section Measurement in the UV Using a Fourier-Transform Spectrometer. *Journal of Geophysical Research-Atmospheres*, 99(D12): 25599-25605.
- Voigt, S., Orphal, J., Bogumil, K. and Burrows, J.P., 2001. The temperature dependence (203-293 K) of the absorption cross sections of O₃ in the 230-850 nm region measured by Fourier-transform spectroscopy. *Journal of Photochemistry and Photobiology A: Chemistry*, 143(1).
- von Glasow, R., Bobrowski, N. and Kern, C., 2009. The effects of volcanic eruptions on atmospheric chemistry. *Chemical Geology*, 263(1-4): 131-142.
- Vountas, M., Rozanov, V.V. and Burrows, J.P., 1998. Ring effect: Impact of rotational Raman scattering on radiative transfer in earth's atmosphere. *Journal of Quantitative Spectroscopy & Radiative Transfer*, 60(6): 943-961.
- Wadge, C., 1981. The variation of magma discharge during basaltic eruptions. *Journal of Volcanology and Geothermal Research* 11 (2-4), 139-168, doi:10.1016/0377-0273(81)90020-2.

- Waters, J.W., 1993. Microwave limb sounding - Theoretical expressions. Chapter 8 in: Atmospheric Remote Sensing by Microwave Radiometry (edited by M.A. Janssen). John Wiley & Sons, Inc. (New York).
- Watson, I.M., Realmuto, V., Rose, W., Prata, A., Bluth, G., Gu, Y, Bader, C., and Yu, T., 2004. Thermal infrared remote sensing of volcanic emissions using the moderate resolution imaging spectroradiometer. *Journal of Volcanology and Geothermal Research*, 135(1-2): 75-89.
- Weibring, P., Swartling, J., Edner, H., Svanberg, S., Caltabiano, T., Condarelli, D., Cecchi, G., and Pantani, L., 2002. Optical monitoring of volcanic sulphur dioxide emissions - comparison between four different remote-sensing spectroscopic techniques. *Optics and Lasers in Engineering*, 37: 267-284.
- Weber, K., Vogel, A., Fischer, C., van Haren, G., Pohl, T., 2010. Airborne measurements of the Eyjafjallajökull volcanic ash plume over northwestern Germany with a light aircraft and an optical particle counter: first results. *Proc. SPIE 7832, Lidar Technologies, Techniques, and Measurements for Atmospheric Remote Sensing VI*, 78320P, doi:10.1117/12.869629.
- Wenig, M., Jähne, B. and Platt, U., 2005. Operator representation as a new differential optical absorption spectroscopy formalism. *Appl. Opt.*, 44(16): 3246-3253.
- Williams-Jones, G., Stix, J. and Hickson, C., 2008. The COSPEC Cookbook: making SO₂ measurements at active volcanoes. IAVCEI, *Methods in Volcanology*.
- Wilson, L., 2009. Volcanism in the Solar System. *Nature Geoscience*, 2(6): 389-397.
- Wilson, L., Sparks, R.S.J. and Walker, G.P.L., 1980. Explosive volcanic eruptions — IV. The control of magma properties and conduit geometry on eruption column behaviour. *Geophysical Journal of the Royal Astronomical Society*, 63(1): 117-148.
- Wright, R. and Pilger, E., 2008. Radiant flux from Earth's subaerially erupting volcanoes. *International Journal of Remote Sensing*, 29(22): 6443-6466.
- Young, A.T., 1982. Rayleigh scattering. *Physics Today*, 35(1): 42-48.

Acknowledgements

I remember my advisor saying: "once you get to the end of this PhD journey you will still be confused... but at a higher level". Wise dictum that only makes sense after this multi-year experience! As I finally complete this step there are good reasons to take a short pause in the journey. I gaze at the horizon, see the route that lies behind, and found myself with some ironies: that long route has actually had an end, but long as it had seemed, it was only a training track for the mountains that are left to climb. The road has been challenging oftentimes, yet it has been charming with its ups and downs. This thesis shows my personal stance about the work of these years, still I have had all along the journey my good travel buddies. To all of them, who are too many to name in these lines, I want to express my deepest gratitude. Too brief but very special thanks to:

Bo Galle, my thesis supervisor, for giving me the opportunity to work with him. I appreciate the freedom and support to some of my ideas and the criticism to others (of my ideas, I mean). I admire your perseverance to keep this (projects) ship afloat in spite of difficult (funding) waters, and your genuine connection with volcanoes and nature that makes everyday's job an enjoyable experience.

Johan Mellqvist, my co-supervisor, for injecting so much energy and enthusiasm in the group, it's still a mystery to me how do you manage to run "Vasaloppets" after touring half of the world with so many new and exciting projects.

My former and present colleagues of the Optical Remote Sensing group for the interesting discussions and supportive and friendly atmosphere. I extend these thanks throughout the corridor and the observatory to reach many of my fellows of the "Institutionen för rymd- och geovetenskap". Gunnar, Donal and all the members of the extremely helpful administrative team deserves a special mention here. I'm also indebted with the institutional support from Chalmers, from the university's Library to the students' funding programs and clubs. There is always something interesting, academically and socially, going on around!

Jerker, Brian and all the good chaps of FluxSense, the teammates and rivals of the weekly innebandy ritual (our fondly remembered Jo was one of the most enthusiasts), and "Master" Andy and the Tang Soo Do club for that "indomitable spirit".

My scientific collaborators, in particular the growing NOVAC family. It has been an honor to cooperate with my colleagues in Quito, Heidelberg, Kiel, Goma, Mexico DF, Pasto, Manizales, Petropavlosk-Kamchatsky, Arequipa, and other places. Also to my colleagues within the FIEL-VOLCAN, FUTUREVOLC, and Congo projects, the ERCA school, CCVG, and IGP for such rewarding collaborations or stimulating recognitions.

The friends I have made in Sweden and those I have in Ecuador and elsewhere, who have made the difficult tasks bearable and the bright days even more shining.

My beloved family, especially my dear mom María Dolores, my sisters, nephews and their families, my mother-in-law Marlene and the rest of you, for keeping me connected with my origins and with all those important things in life.

My wife Vivi, and my children Isaac and Carolina. You are my present and my connection with the future, and who make my life meaningful. More than thanks, you deserve the credit for each of our steps together. Because of you, at the end of this journey I am happy... but at a higher level.

